POLITECNICO DI TORINO

Department of Electronics and Telecommunications

Master's Degree in Electronic Engineering

Politecnico di Torino

Master's Degree Thesis

Design of smart electromagnetic surfaces for next generation of communication systems

Supervisors

Prof. Paola Pirinoli

Dott. Michele Beccaria

Candidate

Alessandro Tuninetti

October, 2023

Ho sceso, dandoti il braccio, almeno un milione di scale
e ora che non ci sei è il vuoto ad ogni gradino.
Anche così è stato breve il nostro lungo viaggio.
Il mio dura tuttora, né più mi occorrono
le coincidenze, le prenotazioni,
le trappole, gli scorni di chi crede
che la realtà sia quella che si vede.

Ho sceso milioni di scale dandoti il braccio
non già perché con quattr'occhi forse si vede di più.
Con te le ho scese perché sapevo che di noi due
le sole vere pupille, sebbene tanto offuscate,
erano le tue.

(Eugenio Montale, *Satura*, 1966)

Dedicated to Giorgia, my family and my friends

Acknowledgements

Durante questo percorso di Tesi diverse emozioni si sono susseguite: gioia, ansia, entusiasmo e felicità. Da solo non sarei mai riuscito a concludere tale cammino e perciò tengo particolarmente a ringraziare di cuore tutte le persone che mi hanno seguito ed aiutato durante questi mesi.

Innanzitutto ci tengo a ringraziare la Prof.ssa Paola Pirinoli che sin dal primo incontro per la presentazione dei possibili argomenti di Tesi è sempre stata molto disponibile e gentile, mantenendo tali capacità durante tutti i mesi successivi, con grande esperienza e professionalità.

Nei mesi di svolgimento della Tesi, anche il Dott. Michele Beccaria, a cui va un enorme ringraziamento, mi ha affiancato e sostenuto durante tutte le attività di simulazione svolte e durante la stesura di tale lavoro, con grande umanità e cordialità.

Un grande ringraziamento va soprattutto alla mia fidanzata Giorgia, alla quale questa Tesi è dedicata. Dopo quasi 6 anni di fidanzamento non ha mai smesso di credere in me. Mi è sempre stata accanto seguendo tutto il mio percorso al Politecnico e giorno per giorno, anche quello di Tesi. Anche la nostra cagnolina, Leila, mi è stata vicina, mettendosi spesso a dormire a fianco a me mentre io lavoravo al computer per ore, "standomi vicino" a modo suo.

Vorrei inoltre ringraziare la mia famiglia: mamma e papà che mi hanno sempre spronato a migliorare e andare avanti, mio fratello Gabriele che, a 13 anni, vedendo l'impegno richiesto per laurearsi, ha già deciso di non frequentare l'università.

Grazie anche a tutti i miei parenti: zii, cugini e soprattutto nonni, che hanno sempre guardato con ammirazione il mio percorso universitario.

Un caloroso ringraziamento ad Andrea, il compagno di laboratori per eccellenza, con cui ho condiviso letteralmente ogni giorno di questo percorso universitario e

affrontato, con successo, importanti sfide.

Ultimi, ma non per importanza, anche a tutti i miei amici va un enorme grazie, per avermi sostenuto ed essersi interessati a me ed avermi fatto svagare anche nei momenti difficili.

Grazie infinite a tutti voi.

Alessandro

Abstract

Smart electromagnetic surfaces (SESs) are novel technologies that have gained significant attention in the field of wireless communication. They are expected to play an important role in the development of 5G, 6G and future wireless communication systems, that will be asked to fast data transfer rates, wide bandwidth, better coverage and almost zero latency. These goals can be achieved using mm-waves or sub-THz frequency bands, that present several advantages. On the other hand, they also suffer from some limitations as higher free space loss, higher building penetration loss, and strong interaction with obstacles along the propagation path. To overcome these drawbacks without increasing the complexity and the cost of the systems, recently the possibility of exploiting the environment in which the signal propagates as a further degree of freedom has been investigated. The idea is to design a smart electromagnetic environment, that can actively contribute to improving the system performance. Its definition is possible thanks to the introduction of several active and passive devices that allow reaching blind spots or covering desired areas without increasing the number of base stations. Among them, there are SESs i.e. thin surfaces designed to provide not specular reflection. Two possible solutions have been considered for their realization: in the first case, they are completely passive surfaces able to re-direct the incident field in a fixed direction, while an alternative consists in using reconfigurable surfaces that can change the direction of re-radiation by adjusting their behavior. Both the two solutions are realized subdividing the surface in unit cells that can have either a resonant or a sub-wavelength size. In both the cases, in its widely-used version, the unit cell consists in a metal patch, with a proper shape, printed on a thin dielectric layer located over a ground plane: varying one or more of the geometrical parameters of the patches it is possible to control its response, and in particular

the reflection coefficient (or the surface impedance) it provides.

In this context, the activity carried on during the thesis has been focused on the design of an innovative (passive) smart electromagnetic skins. The two main aspects on which the work concentrates are the following.

Design of an innovative resonant unit cell with enhanced features. The result of this activity has been a new geometry able to provide a smooth variation of the phase of the reflection coefficient over a range of 360°, necessary to improve the SES bandwidth. Moreover, it possesses several free parameters, and therefore the possibility to varying simultaneously two of them has also been investigated.

Design of a curved SES, to be integrated on a street light or a stop light pole. Such an innovative solution presents several advantages in comparison with the conventional one, in which the smart skin is mounted on the wall of a building. It has a lower visual impact and can be used also in areas as the historical centers of towns, it can be rotated on the pole to maximize the system's performance, that is not affected by the not negligible contribution of the wall.

The performance of both the unit cell and a curved SES designed with its use have been numerically tested and compared with solutions where the re-radiating element is a square patch or/and with planar SESs: the obtained results prove the effectiveness of the proposed configuration.

Table of Contents

List of Tables

List of Figures

Acronyms

AI

Artificial Intelligence

AMC

Artificial Magnetic Conductor

AR

Augmented Reality

BTS

Base Transceiver Station

CRA

Convex conformal ReflectArray

E2E

End To End

EBG

Electromagnetic Band Gap

FSS

Frequency Selective Surface

HIS

High Impedance Surface

IoE

Internet of Everything

IRS

Intelligent Reflecting Surface

LoS

Line of Sight

MIMO

Multiple-Input Multiple-Output

ML

Machine Learning

PCB

Printed Circuit Board

PE

Patch Element

PSS

Phase Shifting Surface

RA

ReflectArray

RCS

Radar Cross-Section

RIS

Reconfigurable Intelligent Surface

SEE

Smart Electromagnetic Environment

SES

Smart Electromagnetic Surface

SLL

Side Lobe Level

UC

Unit Cell

Chapter 1

Smart Electromagnetic Surfaces

1.1 Introduction

The main goal of this work is to design a passive non-reconfigurable *Smart Electromagnetic Surface* (SES) with innovative resonant elements, that can be mounted not only on building facades (for which flat surfaces can be used) but also on objects such as lampposts, traffic light poles and other curved surfaces of the urban furniture. Due to the curved shape of the latter, the smart surface must be curved too (i.e. conformal), in order to be accommodated on these structures.

The thesis is organized into 4 chapters. Chapter 1 presents a general discussion on SESs, including their operating principles and implementations. Along with advantages and disadvantages, the State of the art is analyzed. Since the technique adopted for the design of the SES derives from the one generally adopted for *Reflectarrays* (RAs), Chapter 2 provides a detailed discussion of the RA technology, from the theoretical analysis approach to the practical skills for their design, for both the planar and conformal configurations. In Chapter 3 the design of an innovative resonant unit cell with enhanced features is proposed, showing all the followed steps. Chapter 4 provides an exhaustive analysis of different configurations of SESs, in order to assess the performance of the curved solution and the use of the proposed unit cell, with comparisons between similar structures.

1.2 The next generation of communication systems

Future wireless communication systems will be asked to fast data transfer rates, wide bandwidth, better coverage, almost zero latency and low energy consumption. These goals can be achieved by using new modulation and coding methods, novel multiple-access techniques, antenna arrays, wave propagation, radio frequency transceiver design, real-time signal processing and mmWaves or THz frequency bands[1]. Significant efforts are underway to characterize and understand wireless systems beyond 5G, which we refer to as the sixth generation (6G) of systems[2]. Some important driving characteristics linked to the next decade of lifestyle and societal changes are related to the new technologies as *Augmented Reality* (AR), *Artificial Intelligence* (AI), *Machine Learning* (ML), wearable devices requirements, *Internet of Everything* (IoE), vehicle communications, with expected data rates of approximately 1 Tb/s[3], to support AI for driving autonomous systems. Holograms and telepresence, along with multisense communications, in combination with tactile networks, are key driver technologies for the sixth generation of communication systems. They require extremely rapid data rates and submillisecond latency, that are beyond the capabilities of the current 5G and previous technologies. Security is also an important requirement. Some efforts have been done toward the development of an uninterrupted global broadband access exploiting the integration between terrestrial and satellite networks[4], [5]. The 6G requirements also imply the use of particular types of multiple antenna techniques, as *Ultramassive Multiple-Input Multiple-Output* (MIMO) *Systems*, *beamforming*, *spatial modulation* and others, already present in the actual 5G system. However, there is room for improvement for the new 6G technology to reach the optimality in performance and real-time implementations. Antennas must be able to work at such high frequencies, and scaled to larger physical areas. Attenuation and penetration losses in outdoor-to-indoor propagation increase dramatically at mmWave frequencies, as well as strong interaction with obstacles along the propagation path. The small wavelength of the THz signals allows a much greater number of antenna elements to be incorporated into the devices and *Base Transceiver Stations* (BTSs) operating in this band. This allows the use of advanced adaptive array technologies that can overcome the

range limitations[6], and the employment of SES- and *Reconfigurable Intelligent Surface* (RIS)-empowered *Smart Electromagnetic Environments* (SEEs) to improve coverage and other performance metrics[7], [8].

1.3 Introduction to EM surfaces

EM Surfaces or *Intelligent Surfaces* are relatively new enabling technologies for wireless communications. They are reflective surfaces, usually planar or conformal, that can be employed in 5G and 6G communication systems.

There are many types of EM surfaces: some refer to the same technology, others have different electromagnetic features. A classification is presented in Table 1.1.

Types of EM surfaces	
Structure	Metamaterial based
	Patch-array based
Power source	Reflecting surface
	Waveguide surface
Tuning mechanisms	Passive
	Active

Table 1.1: Classification of different types of EM surfaces. Adapted from [9]

Now, a brief description of them is given.

- **Waveguide surface**: consists of an array of metamaterial elements distributed over an electrically large structure, each subwavelength in dimension and with subwavelength separation between elements. In the antenna configuration we consider, the metasurface is excited by the fields from an attached waveguide. Each metamaterial element can be modeled as a polarizable dipole that couples the waveguide modes to radiation modes. Distinct from the phased

array and electronically-scanned-antenna architectures, a dynamic metasurface antenna does not require active phase shifters and amplifiers but rather achieves reconfigurability by shifting the resonance frequency of each individual metamaterial element[10].

- **Reflecting surface**: this type of antenna reflects incident signals towards the users on the same side of the BTS: each element only reflects the incident signals due to the copper backplane. If active, the electromagnetic (EM) responses can be tuned via onboard positive-intrinsic-negative (PIN) diodes[11], making them reconfigurable. Also, they can be made passive, without any possible reconfiguration. Reconfigurable surfaces can be also transmissive, where signals can penetrate them to serve the users on the opposite side of the BTS, and hybrid, where they have a dual function of reflection and transmission[12].

- **Patch-array based**: they are based on patch arrays with cell size approximately $\lambda/2$. The most common example are reflectarrays. RAs are used as planar or conformal equivalents of parabolic reflectors. The main disadvantage of this kind of configuration is that they function well only if the reflected rays do not have to be tilted much. For common applications of RAs this is not a problem, since the tilt angles of the reflected beam are usually not so large. In most recent communication scenarios the reflected waves should ideally be sent into any direction of the space, therefore this type of antennas must be carefully designed.

- **Metamaterial based**: antennas based on metamaterials have cell sizes much smaller than λ. They offer many benefits, including wide bandwidths, miniaturization, and well-controlled radiation characteristics. RISs based on metamaterials are usually designed to reflect *plane waves* as plane waves propagating into desired directions. Moreover, metasurfaces are equivalent to "lenses", i.e. focusing reflectors with an infinite focal distance. Some recent works have shown that metasurface-based antennas, such as RISs, can control reflection theoretically perfectly, without any spurious scattering[13], apart from manufacturing tolerances and defects, and dissipation losses.

- **Passive**: a *passive* surface is made up by a large number of passive elements

with controllable phase shift, for example, by varying the element dimensions. Currents on elements of reflectarrays and metasurfaces are excited by incident waves (and by fields scattered by all other array elements) and no active radio-frequency (RF) components are needed: they consumes zero direct-current power and the introduced thermal noise is usually negligible. The equivalent path loss of the transmitter-surface-receiver path is much higher with respect to the one of a direct transmitter-receiver loss of an unobstructed direct link. Therefore, thousands of elements are required to compensate for this large path loss.

- **Active**: in *active* surfaces each antenna element is fed by an external, controllable source to reflect the incident signals with reconfigurable phase shifts. To overcome the high loss of the passive, active ones can also amplify the reflected signals, exploiting some reflection-type amplifier with proper techniques. The active configuration hardware architectures and transmission models are quite more complicated with respect to the passive case. Moreover, additional power consumption is unavoidable for the amplification of the reflected signals and additional thermal noise is introduced.

A comparison between active and passive surfaces is depicted in Figure 1.1.

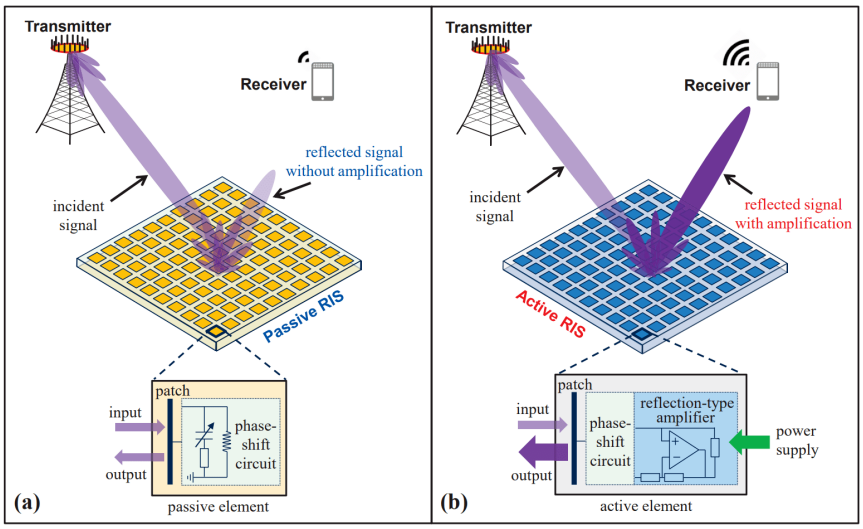

Figure 1.1: Comparison between (a) passive and (b) active surfaces. [14]

1.3.1 Features of EM surfaces

Based on their particular characteristics, EM surfaces can be divided into several categories. In the following some of them will be analyzed. A first scheme is presented in Figure 1.2.

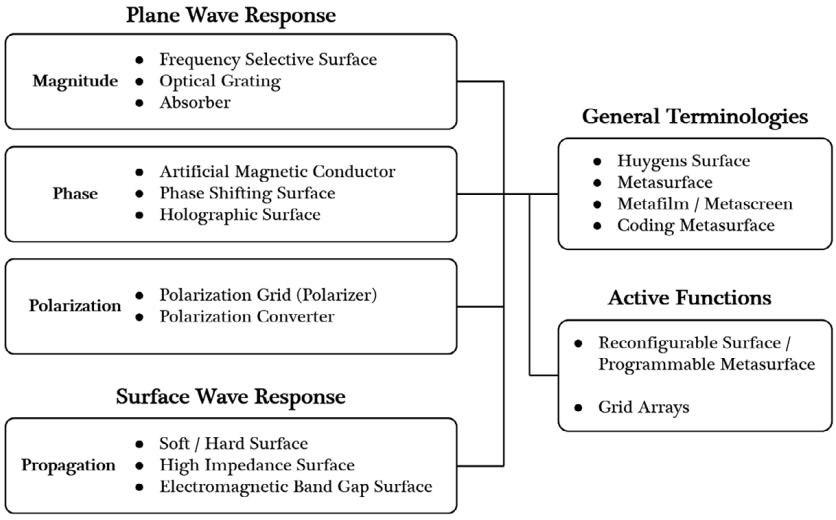

Figure 1.2: Scheme of the EM surfaces categories. [15]

1.3.1.1 Based on magnitude response of a plane wave

Based on the magnitude response of a plane wave it is possible to divide them into:

- *Frequency Selective Surface* (FSS): it is a very active research topic; the FSS acts as a spatial filter which lets some frequencies to pass and blocks the ones out from a certain frequency band. In optics, they are called *Optical Gratings*;
- *Absorber*: refers to a particular type of surfaces where the energy of the incident plane wave is neither reflected nor transmitted, but it is absorbed by the lossy surface.

1.3.1.2 Based on phase response of a plane wave

Based on the phase response of a plane wave it is possible to divide them into:

- *Artificial Magnetic Conductor* (AMC): similarly to a perfect magnetic conductor, reflects the plane wave with 0° reflection phase;

- *Phase Shifting Surface* (PSS): its main goal is to provide a full 360° reflection phase range when the plane waves reflect or transmit through this surface;
- *Holographic Surface*: this surface can provide specific reflection patterns in space including pencil beams, shaped beams and contour beams.

1.3.1.3 Based on polarization response of a plane wave

Based on the polarization response of a plane wave it is possible to divide them into:

- *Polarization grid* or *polarizer*: similar to optical filters, this surface can be designed to let one polarization to pass while blocking the others, by reflecting or absorbing them;
- *Polarization converter*: it can convert the polarization of the incident plane wave into another, for example vertical to horizontal polarization. It acts as an optical *waveplate*.

1.3.1.4 Based on surface wave features

Based on surface wave features it is possible to divide them into:

- *Soft/hard surface*: this particular surface allows the surface wave propagation in one direction, while blocking the orthogonal one (hard and soft operation, respectively);
- *High Impedance Surface* (HIS): it can stop the surface wave's propagation, providing high surface impedance for the fundamental TM mode;
- *Electromagnetic Band Gap* (EBG) *surface*: they highly impede electromagnetic propagation along the device's surface within the frequency band of operation, known as *band gap*.

1.3.1.5 Based on active functions

Based on active functions it is possible to divide them into:

- *Reconfigurable surface* and *programmable metasurface*: PIN diodes, MEMS switches or varactors are integrated into the surface to provide real-time control of the surface properties;

- *Grid arrays*: composed by arrays of amplifiers, oscillators and mixers, spatially distributed in a planar grid to build a quasi-optic system with greater power and performance in microwave, millimeter wave and THz frequency ranges.

In addition, other general terminologies are used for EM surfaces, e.g. *Huygen's surface*, *metafilm* and others, but are here omitted. Moreover, other classifications of these surfaces can be made by using other parameters and some surfaces may show two or more listed features. Special surfaces at research level are also emerging nowadays, exploiting materials with particular characteristics and providing full control on the wave parameters[16].

1.4 Smart Electromagnetic Environment

The mmWave spectrum allows to use channels with wider bandwidths and to accommodate large antenna arrays in very compact systems, reducing also interference. These aspects are fundamental to provide high data rates and very low latency. However, this frequencies are more susceptible to attenuation in presence of blockage effects from obstacles due to the small wavelength. To improve the performance of mmWave applications in case of NLoS (Non-Line of Sight) in urban areas, a simple solution is to increase the number of BTSs to implement network densification, and, as a consequence, to guarantee the minimum signal strength required by the users, by transmitting more power or using new frequency bands. However, this solution also comes with disadvantages. It may not be always a feasible solution due to the lack of backhaul, higher costs and power requirements. A promising approach is to employ the so called Smart Electromagnetic Environment, to take advantage of the environment itself for the propagation of the electromagnetic fields[8]. The SEE is an environment leveraging the electromagnetic properties of new network nodes, whose deployment and operation are optimized to maximize network performance in terms of coverage, by eliminating blind areas (namely, the zones where the signal from the base station is too weak to support a desired

throughput for users' applications), and capacity, while reducing costs and *End To End* (E2E) power consumption[17]. IAB nodes, Smart Repeaters, RISs and SESs are optimized to work together in the same network. The key idea behind RISs and SESs is to use an inexpensive adaptive (smart) thin composite material sheet, which, similar to a wallpaper, covers parts of walls, buildings, ceilings, etc., and is capable of modifying the radio waves impinging upon it in ways that, in some cases, can be also programmed and controlled by using external stimuli (RIS or *Intelligent Reflecting Surfaces* IRS)[18]. Configuring a wireless network in an environment such that an optimal number of them are placed in the most optimal positions currently remains an arduous task[19]. RISs require control circuits for the reconfigurability, for example using PIN diodes[20] or RF switches. Due to the few Watt power consumption, they must be powered with batteries or photovoltaic panels. A more innovative solution suggests to configure them such they can partially absorb the incident signals, thus providing the required power. This approach is also called *Simultaneous Wireless Information and Power Transfer* (SWIPT)[21], [9]. Passive and conformal solutions, such as SESs, allow instead higher flexibility and integration at low cost, especially in the urban environments, where particular architectural[22] and *Line of Sight* (LoS) constraints are present. Neither control devices nor power supply are required for their operation. AI-based design outcomes confirm the effectiveness of the optimization process that allows the designer to analytically synthesize large SESs with a careful control of the resulting reflection/focusing properties[19]. For a detailed analysis of RISs and SESs, see Section 1.5.

An example of SEE is illustrated in Figure 1.3.

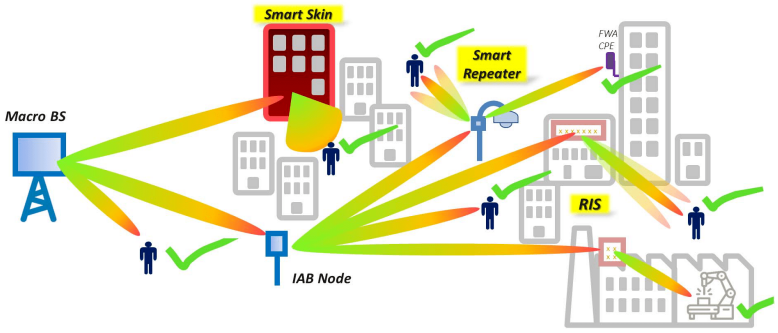

Figure 1.3: A Smart Electromagnetic Environment application scenario. [17]

All the Smart EM actors are potential candidates for enabling the use cases of the industrial environment too, e.g. flexible production lines, connected workers and automated guided vehicles for Industry 4.0. Moreover, the different network nodes can be deployed within the industrial sites with reduced operating costs due to absence of rental fees[17].

1.5 Introduction to SES

SESs are types of *Intelligent Surfaces*. Essentially two of them are here considered, according to their active or passive behavior. RISs are typically planar surfaces comprising a large number of reflecting elements, each of which is able to induce a controllable amplitude and/or phase change to the incident signal independently[23]. The design of each cell (material, size, inter-distance between the cells) determines the properties of the whole surface. They may be programmed and controlled based on the available environmental information[24] and therefore made *reconfigurable*, which means that the angle of reflection can be reconfigured (via software) regardless of the angle of incidence[25]. To estimate the environmental state information, the RISs may contain sensing elements. The general operation of RIS is split into two phases: (1) control and programming phase, when the environmental information is estimated and the RIS is configured; and (2) the normal operation phase, when the RIS is already configured and works as part of the network[8].

Passive SESs are modular, *passive* and static surfaces that allow to achieve a low-cost *electromagnetic skin*. In general, an electromagnetic skin is a structure conformal to the external surface of the object to which it is attached and offers functions related to the sensing and manipulation of the electromagnetic waves. They can be attached to a building external wall[26] to redirect the incident electromagnetic field modeled as a *plane wave*, coming from a BTS, towards areas where the signal would otherwise be weak[8], as illustrated in Figure 1.4.

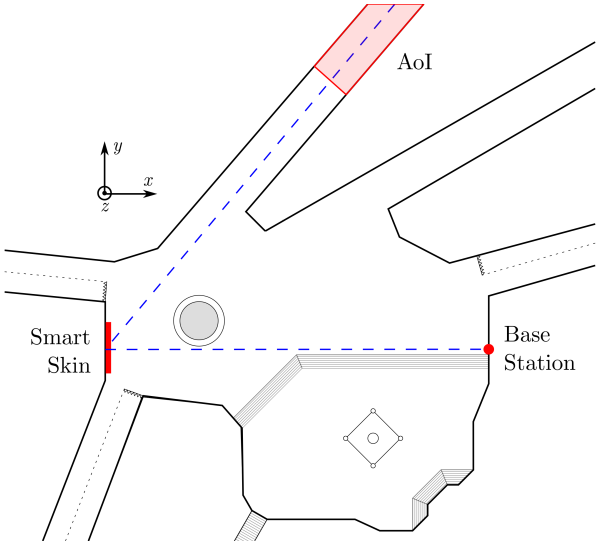

Figure 1.4: Typical urban scenario using a SES. [8]

A SES can be designed based on the non-specular reflection: two possible solutions are *metasurfaces* with unit cell much smaller than λ and *resonant unit cells*, used in reflectarrays. As depicted in Figure 1.5, for a standard metal plate, Snell Law applies. This means that the input angle θ_i is equal to the reflected (scattered) angle θ_s since the metal plate is a coherent surface, i.e. it has a constant surface impedance.

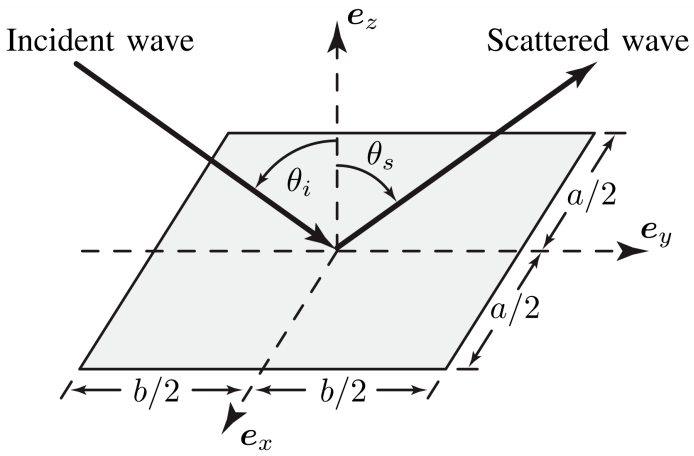

Figure 1.5: Generalized Snell Law scheme. [27]

For example, a metasurface has, instead, an altered surface impedance in order

to control the bounce-off direction of the reflected beam, providing non-specular reflection. A comparison between a metal plate and a metasurface is provided in Figure 1.6.

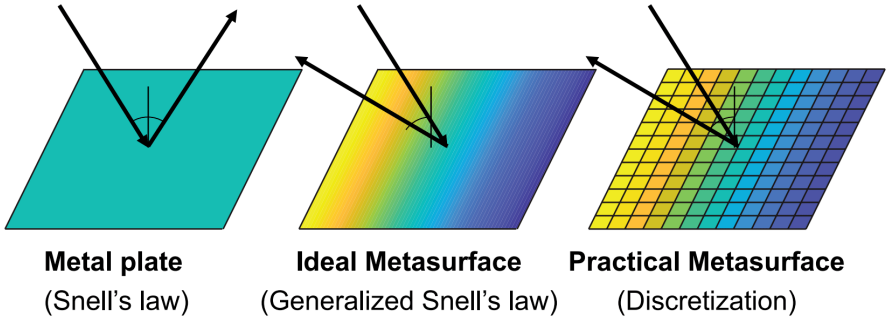

Figure 1.6: Comparison between a typical metal plate and a metasurface. [28]

Also, a metasurface has not a constant distribution: it is made up of small elements of sub-wavelength dimensions (for example $\lambda/5$, $\lambda/10$). Each reflecting cell can be independently designed in order to get the desired phase and/or amplitude characteristic of the reflected beam, to mimic the mirror behavior, but, with a reconfigurable capability.

Beside metasurfaces, the resonant unit cells technique, generally adopted for RAs, can be also exploited to design such intelligent surfaces with non-specular beam reflection. As detailed in Chapter 2, it is possible to develop the phase distribution of the surface elements in order to get the desired direction of the reflected beam. The elements, called *Unit Cells* (UCs), usually have dimensions $\lambda/2$, $\lambda/3$.

In this work the focus will be pointed toward this second type of surface design, developing an innovative passive SES with enhanced features.

A general scheme for SESs is provided in Figure 1.7.

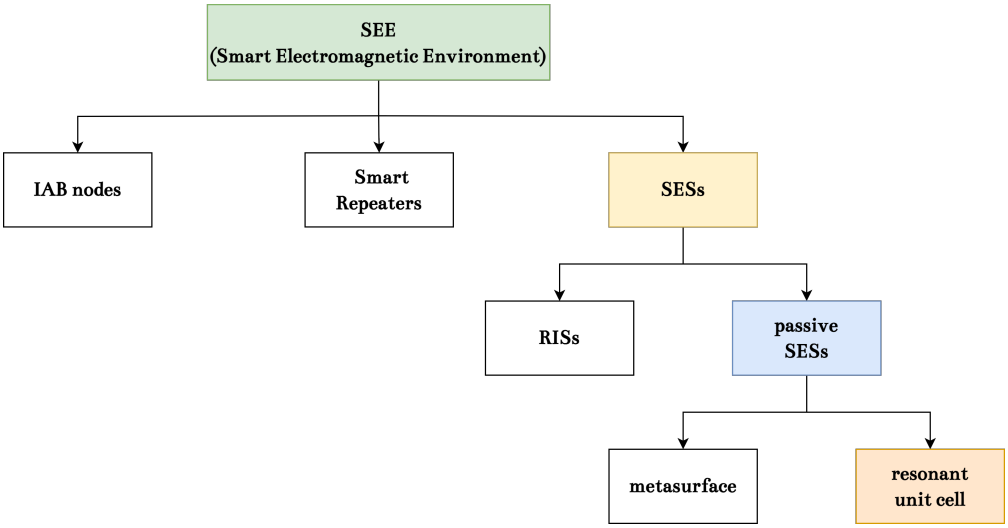

Figure 1.7: General scheme for SES categories.

1.6 Applications of SES

With the advance of the communication technology, obstacles and scatterers in the environment cannot be neglected due to increase of the frequencies: higher path loss and larger sensitivity to blockage must be taken into account. The LoS condition cannot be guaranteed anymore and the NLoS condition must be included in the design process. Usually, it is considered as a problem for the network design. By employing intelligent surfaces this can be bypassed, considering obstacles as enablers of the electromagnetic propagation and not impairments, mounting them on the building facades and controlling the electromagnetic field propagation, to ensure the desired QoS (Quality of Service) to the users.

An example of this last consideration is shown in Figure 1.8.

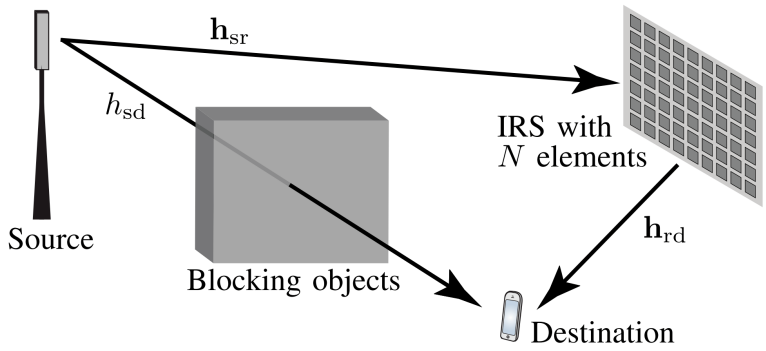

Figure 1.8: Obstacle avoidance by using RIS. [29]

There are several potential scenarios where smart surfaces can be employed. As already mentioned, a SEE can be built where the obstacles' scattering capabilities are modified by adding non-invasive coating materials, exploited to obtain the desired electromagnetic field distribution in the target region of interest without adding additional BTSs and thus reducing the outdoor electromagnetic exposure.

Other potential scenarios can be in homes, to enhance the indoor connectivity, in buildings, to increase the selectivity of the indoor-outdoor communications, in factories, hospitals, universities, train stations and so on.

Actually, moving vehicles can be equipped with such surfaces, for example cars, to enhance the vehicle-to-vehicle communications for the next generation of cars, trains and airplanes to provide high speed Internet connections to the passengers.

Recent works, have exploited the use of these surfaces inside clothes, to monitor the health of people by using special sensors, creating a sort of *body network*.

1.7 Advantages of SES

As already mentioned, the use of SESs provides many advantages. Starting from their manufacturing process, static and passive ones have very low cost, since they are in most of the cases made of a *Printed Circuit Board* (PCB). Instead, active surfaces, which require active amplifiers, will be more expensive.

Another advantage is the easy integration in the environment. For example, it is possible to embed them into building facades, indoor walls, aerial platforms, roadside billboards, highway polls and vehicle windows. It is not only possible to

integrate them, for example, on a wall surface, but even to hide them inside: in this way the antenna becomes invisible. The so-called *intelligent walls* are common walls but equipped with an active frequency selective surface and sensors. The intelligent wall can be designed as a self-configuring and self-optimizing autonomous part of a collaborative infrastructure[30].

As already highlighted, when the LoS is not guaranteed between the BTS and the user, for example due to obstacles, the received field strength will be very weak, causing a very low data stream throughput at the user. With SESs one can significantly improve the received SINR (signal-to-interference-plus-noise ratio) by using the virtual LoS formed via the reflection of the field thanks to the smart surfaces application.

The final advantage of the SESs is related to their back-compatibility. In fact, they are compatible with the standards and hardware of the existing wireless networks, since they reflect electromagnetic waves without applying any sophisticated signal processing. This makes them sustainable and an environmentally friendly technology solution.

1.8 Disadvantages of SES

There are also some disadvantages to the use of these systems, such as the impossibility of on-board channel estimation, signal regeneration and amplification. If the received signal is too weak, a passive SES is not capable of regenerating it and low performance is obtained. However, even when considering an *active* surface, it needs hundreds of reconfigurable elements to be competitive with classic decode-and-forward (DF) relaying technique[29]. The reason is that the source's transmit power must travel over two channels to reach the destination, leading to a very small channel gain per element in the RIS. Hence, the antenna needs many elements to compensate for the low channel gain, but, since each element has very small dimensions, the antenna size is still rather small.

In the design procedure, a tradeoff between the coverage range of the surface, its size and the number of elements that need to be deployed on it must be considered and can be very challenging. The larger the desired coverage range is, the larger the size of the surface or the larger the number of elements on the same surface

area are needed. This means that the elements will have smaller dimensions and much smaller inter-distance, compared to the wavelength. This is an ambitious problem that needs careful study and analysis in the design procedure.

1.9 SES State of the art

In the design of new SESs, many challenges have to be faced. In order to improve the coverage in urban areas using millimeter-wave it is necessary to use an optimization strategy to exploit minimum complexity, suitable coverage and reduced power consumption. Additionally, the eye impact must be also taken into account: in the following some attempts in this direction will be presented.

In [31], the available surface on building facades is divided into *tiles*, the minimum size elements composing the entire surface. Optimal size and position of them must be evaluated in order to efficiently design such antennas. The reference geometry is depicted in Figure 1.9. The signal coming from the BTS, in the far field, modeled as a plane wave, is incident on a surface $\mathcal{S}$ which is divided in N tiles of equal size $\Delta\mathcal{S} = L \times L$, centered at the position $r_{\mathcal{S}}$.

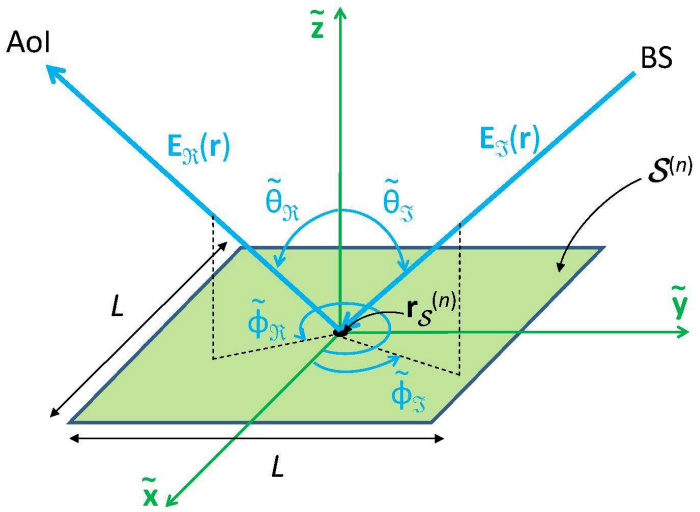

Figure 1.9: Geometrical configuration of the SES. [31]

$\mathbf{E}_{\Im}(\mathbf{r})$ is the incident field at working frequency f on the surface and $\mathbf{E}_{\Re}(\mathbf{r})$ is the reflected one. The reflected beam has a different angle with respect to the

incident one, along the so-called *Area of Interest* (AoI). The main synthesis goal is to get

$$\mathcal{P}_{\Re}(\mathbf{r}_u) \geq \mathcal{P}_{th} \tag{1.1}$$

which means that the power collected at the user position of the AoI must be greater than a user-defined coverage threshold.

In order to solve this design problem, one can exploit a binary implementation of the NSGA-II. Using this algorithm, the presence/absence of a tile on the final EMS layout ($\mathcal{S}_{opt}$) is mathematically modeled by means of a binary variable, t_n (with $t_n \in \{0, 1\}$, $n = 1, ..., N$). If $t_n = 1$, then the n-th tile $\mathcal{S}(n)$ is present on the facade of the building and it contributes to the reflection of the EM wave towards the AoI. Otherwise (i.e., $t_n = 0$), the n-th tile $\mathcal{S}(n)$ is not installed on the external wall of the building, which maintains its original scattering properties without contributing to the enhancement of the signal in the coverage area Ω[31].

The tile layout with simulated and numerically evaluated power angular distribution is shown in Figure 1.10.

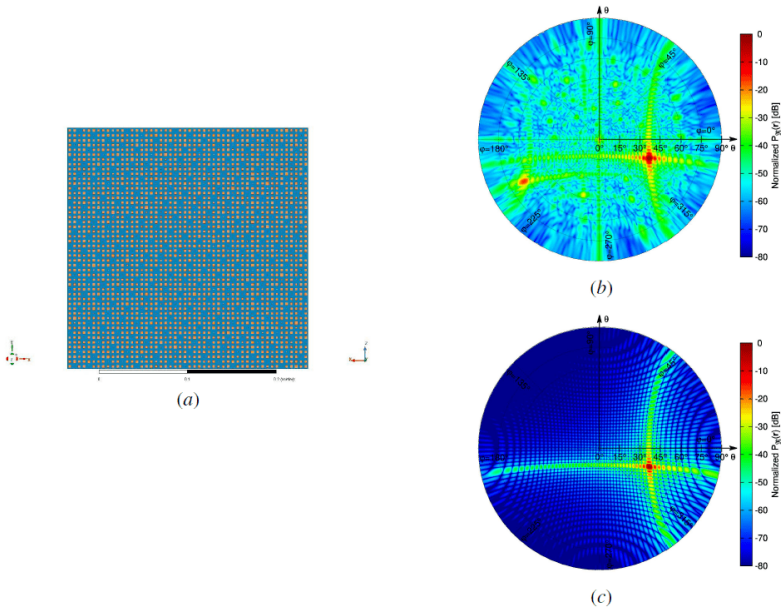

Figure 1.10: Layout of (a) the ANSYS HFSS model of the single-tile EMS and plot of (b)(c) the angular distribution of the power, $\mathcal{P}_{\Re}(r)$, reflected from the EMS on a sphere at a distance of 5 m and computed with (b) ANSYS HFSS or using (c) the closed-form relationship. [31]

The reference scenario is shown in Figure 1.11.

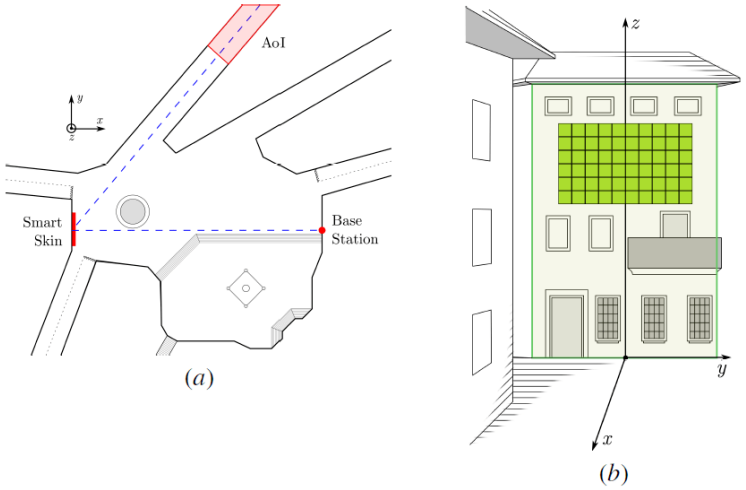

Figure 1.11: Reference scenario (a) and total admissible surface (b). [31]

Some results for particular scenarios are then presented, for example the one in Figure 1.12. The parameters are: $f = 27$ GHz, $\mathcal{S} = 15$ m^2, $L = 0.5$ m, $N = 60$, $\mathcal{P}_{th} = -70$ dB.

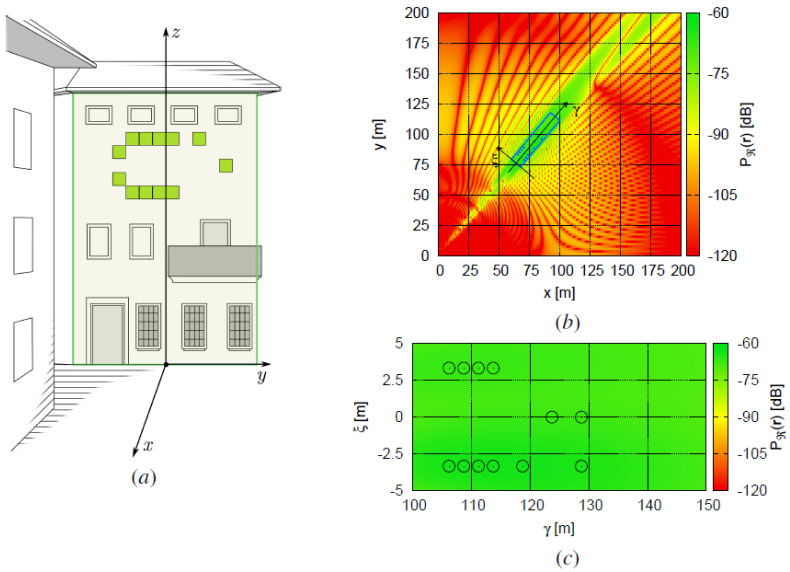

Figure 1.12: EMS layout (a) and received power $\mathcal{P}_{\Re}(r)$ in $\Psi = x \times y$ region (b) and within the AoI Ω (c). [31]

The signal turns out to be stronger not only in Ω, but also before and after, since the skin tiles generate simple pencil beams with an elongated footprint on the ground, i.e. the dots in Figures 1.12(b)-1.12(c), being the $M = 12$ points with $n = \{3, 4, 5, 6, 8, 12, 30, 32, 43, 44, 45, 46\}$ (matrix elements) where the peaks of the beams reflected from the M-EMS tiles are directed. Finally, the proposed algorithm for the optimization of the urban coverage problem shows very good results also with sparse tiles layouts and different tiles sizes. Also, the use of modular, passive and static artificial metasurfaces to be installed/embedded on the facades of urban buildings provide sustainability thanks to its "green" and non-invasive nature[31]. Other recent researches show the use of RAs acting as passive surfaces. In [32], two 800 mm×400 mm reflectarray panels (KLONES) have been designed to improve 5G mm-wave coverage in the 28 GHz band in an outdoor scenario. The two are designed to generate a broadened and deflected beam in dual-linear polarization (horizontal and vertical) with angle of incidence of the impinging field up to 50° and achievable phase range greater than 360°. They are tested in two different scenarios to evaluate their performance. The designed unit cell for these RAs is based on horizontally and vertically organized dipoles to let the phase control on both horizontal and vertical directions. The phase adjustment is achieved by varying l_{X1} and l_{X2} lengths for the vertical polarization and l_{Y1} and l_{Y2} for the horizontal one. The dielectric substrate on which the dipoles are printed is FR-4 ($\varepsilon_r = 3.6$, $\tan\delta = 0.01$) of 1.5 mm thickness. Then, the unit cell is covered by a 1.5-mm thick foam sheet which is used to protect the dipoles. The foam is glued to the upper side of the FR-4 by means of a 0.076 mm thick bonding film. The designed unit cell parameters are depicted in Figure 1.13. The performance of the reflectarray cell has been analyzed taking into account the three dielectric layers[32].

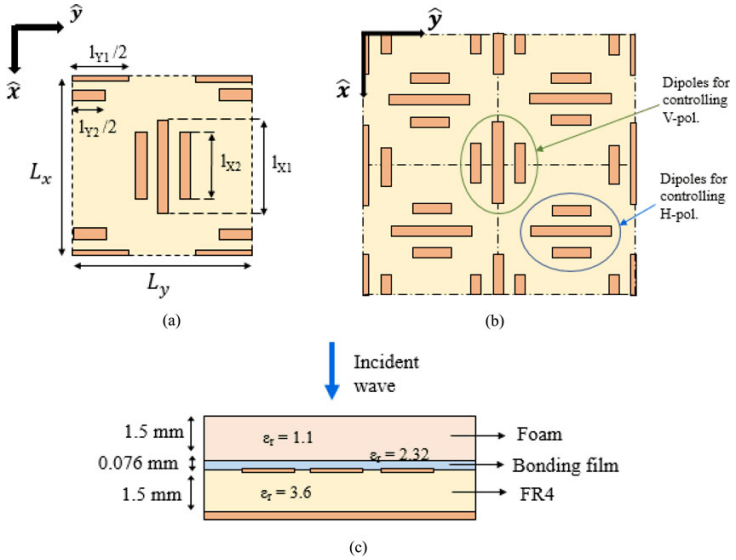

Figure 1.13: Upper view of (a) the periodic unit cell and (b) the reflectarray periodic structure. (c) Lateral view with the stack-up configuration. [32]

This unit cell design allows for higher phase change variations and more linear phase response with respect to classical unit cell approaches (square patches, etc.). Even with strong oblique incidence conditions this unit cell shows good performance. It provides the advantages of multi-layered unit cells but using only one single layer of printed elements, providing lower costs, volume and weight.

The results obtained for one of the two RAs are shown in Figure 1.14.

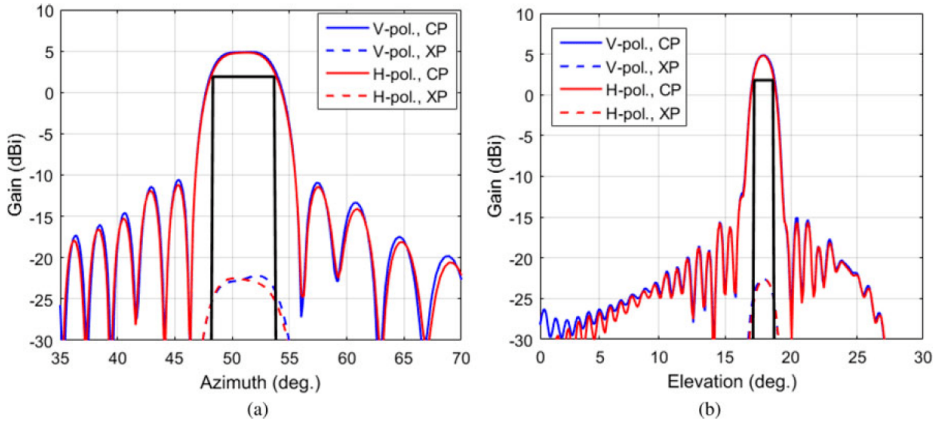

Figure 1.14: Simulated radiation patterns at 27.7 GHz in the (a) azimuth and (b) elevation planes, including co-polar (CP) and cross-polar (XP) components. [32]

For the second RA, similar results have been found. The reflectarray panels exhibit a stable performance within the 27.2-28.2 GHz band used for 5G communications, fulfilling the half-power beamwidth and beam pointing requirements of the scenario (depicted as masks in the above Figure). These results prove the potential of flat reflectarray panels as a low-cost technology to implement passive SESs that will solve coverage problems in 5G mm-wave networks[32].
Recent works from many research groups point towards the use of SESs as programmable thin surfaces (with easy integration in building facades) capable of modifying wave properties. Here are presented two of the most advanced prototypes in this direction. Firstly, it is worth to mention the MIT's RFocus prototype[33]. It is a 2-D antenna reflector made of 3200 elements, which is able to backscatter the incident signal without generating one on its own. It includes a *Software-Controlled Surface* placed in the environment, made up of thousands of simple switching elements. A controller, with optimization algorithms, that configures each element is needed, so that the surface, as a whole, directs a signal from a transmitter to a receiver without any signal amplification. These antennas are inexpensive because they don't need costly electronics, since they only act as reflectors and they do not use expensive high-speed connection wires to the transmitter. In fact, the cost is around few cents per unit element. Each of the antenna composing the whole structure may be in the OFF state (it will be transparent to an incident field) or in the ON state (truly acting as a reflector), directing the beam toward a well defined direction. The total occupied surface is around 6 m^2; the working group said: "This configuration may well be the largest published number of antennas ever used for a single communication link."[33]. A picture of RFocus is presented in Figure 1.15.

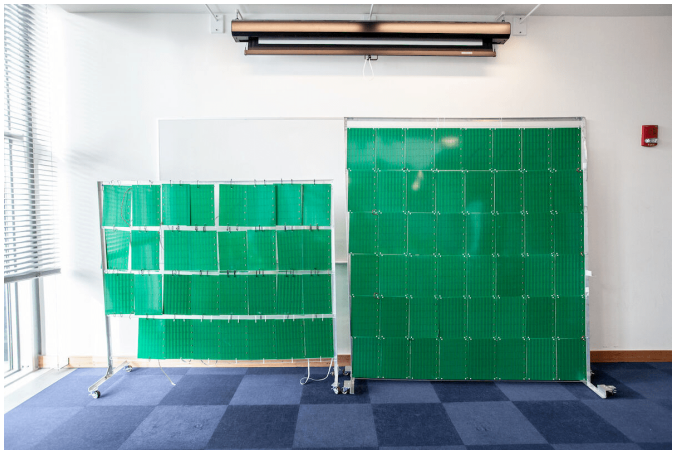

Figure 1.15: MIT's RFocus prototype. [33]

The CDF of the ratio of the improved signal strength to the signal strength when the surface is physically removed is shown in Figure 1.16.

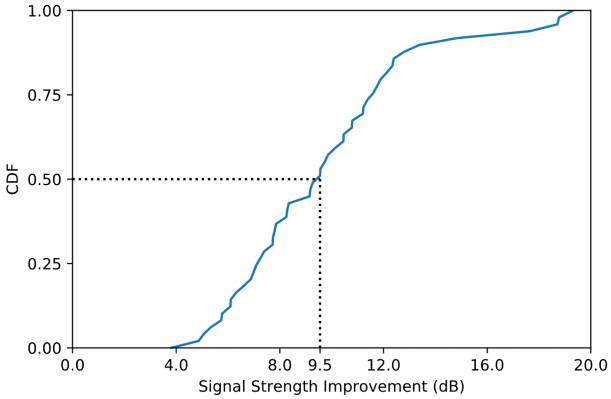

Figure 1.16: CDF of improvement in the signal strength. [33]

The medium improvement introduced by RFocus is 9.5 dB while the minimum and maximum improvements across all locations are 3.8 dB and 20.0 dB, respectively.

Lastly, it is worth to mention *the World's First Successful Trial of Transparent Dynamic Metasurface* from NTT DOCOMO, INC., Japan.

The smart glass is a thin layer of metasurface with large number of sub-wavelength sized elements, working at 28 GHz (5G radio signals), covered with

a glass substrate. Slightly moving the glass substrate, dynamic control of radio waves is achieved, in three modes: full penetration of incident radio waves, partial reflection of incident radio waves and full reflection of all radio waves. Compared to conventional dynamic control methods using semiconductors, this new design offers two advantages: it allows dynamic control while maintaining transparency of the window and it facilitates enlargement of the substrate[34]. A picture of the fabricated transparent metasurface is shown in Figure 1.17.

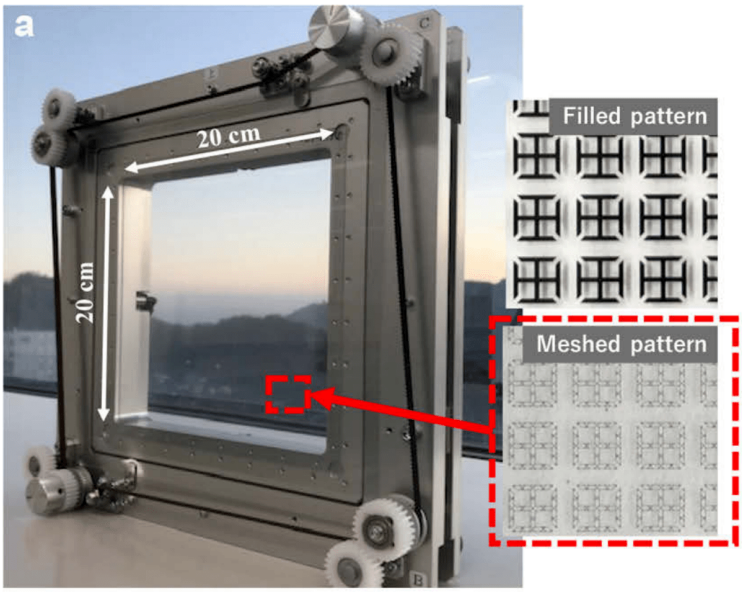

Figure 1.17: Fabricated transparent dynamic metasurface. [34]

The working principle of the transparent dynamic metasurface is based on the inter-layer distance change of the metasurface and movable transparent substrate relative spacing. When the two are in contact, the resulting resonance frequency is low since it is manly determined by the metasurface substrate. Instead, when the two substrates are separated, the resonance frequency increases since the total permittivity becomes the one of the combination of the metasurface substrate and air. The unit cell of the metasurface substrate is depicted in Figure 1.18: four gaps are constructed at the corners of the *Split-Ring Resonators* (SRRs) to yield a 4-fold rotational symmetry to support vertical and horizontal polarizations.

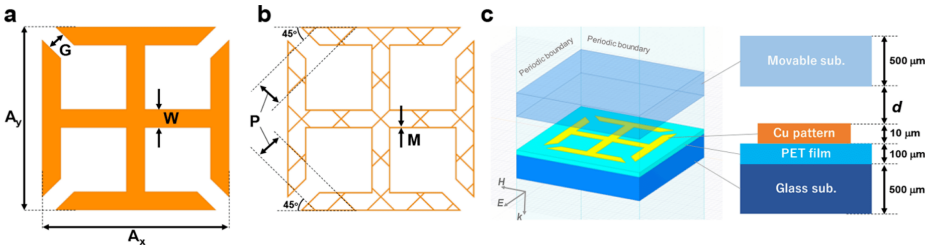

Figure 1.18: Unit cell used in transparent dynamic metasurface. [34]

There are two working bands, as depicted in Figure 1.19, namely band A and B. The band B is mainly used, since the required change in resonance frequencies to achieve the contact state with high transmittance can be smaller than that to achieve the separate state with high transmittance in band A[34].

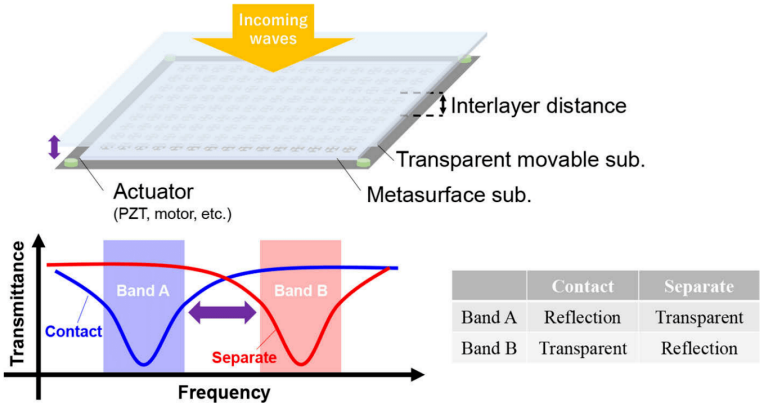

	Contact	Separate
Band A	Reflection	Transparent
Band B	Transparent	Reflection

Figure 1.19: Operating principle of the transparent dynamic metasurface. [34]

Therefore, using band B, the smart glass behaves as a transparent surface in contact state (of the two substrates), i.e. with full penetration of the incoming wave, while in reflection mode when the two substrates are separated, i.e. it allows partial or full reflection of the incident radio waves.

This surface achieves dynamic manipulation of radio-wave reflection and penetration in a highly transparent package, suitable for unobtrusive use in the windows of buildings and vehicles, as well as on billboards, with 79.5% or even higher visible light transmission rate.

Moreover, the research group is currently working to let the activation of the

transparent metasurface at frequencies higher than those of 5G technologies, in order to use it with newer wireless communication systems.

Chapter 2

Reflectarrays

As already pointed out, here the focus is on the design of passive SESs using resonant unit cells. They are the constitutive elements also of RAs, and therefore these last have been used as starting point for the analysis of the performance of a reflective surface and of the developed unit cell. For these reasons, in this Chapter they are discussed.

2.1 Introduction to Reflectarray Antenna

A reflectarray antenna is a particular type of antenna that consists of either a flat or a slightly curved reflecting surface (*reflector*) and an illuminating *feed* antenna. Figure 2.1 shows the typical geometry of a RA.

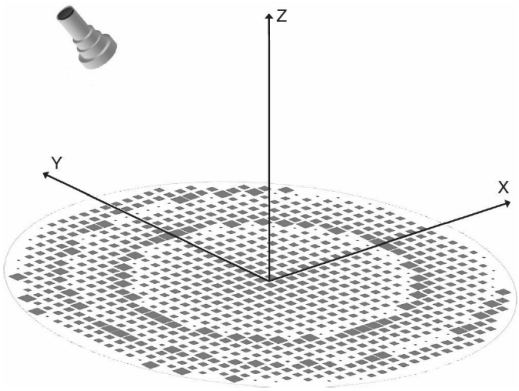

Figure 2.1: Typical planar RA geometry. [35]

It is made up by an *array* of radiating elements (usually patches) that provide a preadjusted value of phase in order to form a focused beam when it is illuminated by a feed, similarly to a parabolic antenna. They are printed a dielectric substrate material with a ground plane on the opposite side. It is worth to mention one of the most important characteristic of such a system. The feeding system eliminates the complexity and losses of the feeding network used in traditional planar arrays; as a consequence RAs have a much higher efficiency with respect to them. However, the most relevant shortcoming of this type of antenna is related to the bandwidth. This is essentially due to two facts, that are the phase response of the single radiating elements and the different path lengths from the feed to the phase front. This last problem can be solved by using larger aperture antennas while the first one has been mitigated by using new design techniques.

A typical RA configuration is shown in Figure 2.2.

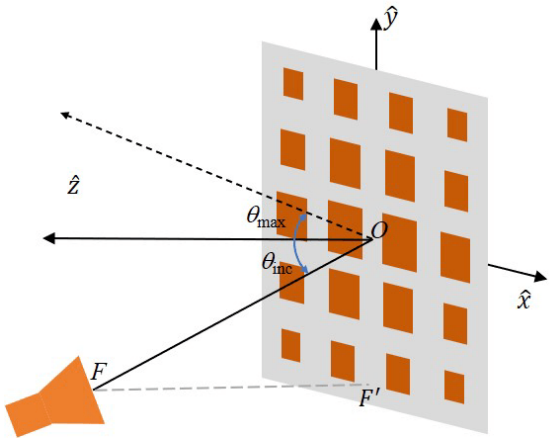

Figure 2.2: Reflectarray configuration with patch elements. [36]

In order to design a RA, it is first necessary to characterize the single reflectarray elements. There are many possible choices, for example open-ended waveguides, dipoles, rings and, the most important, patches.

Figure 2.3: A fabricated reflectarray antenna with patch elements. [37]

2.2 RA patch elements

Reflectarrays using *Printed microstrip Elements* (PEs) have been developed to achieve low reflecting surface profile, small antenna mass and low manufacturing cost [35].

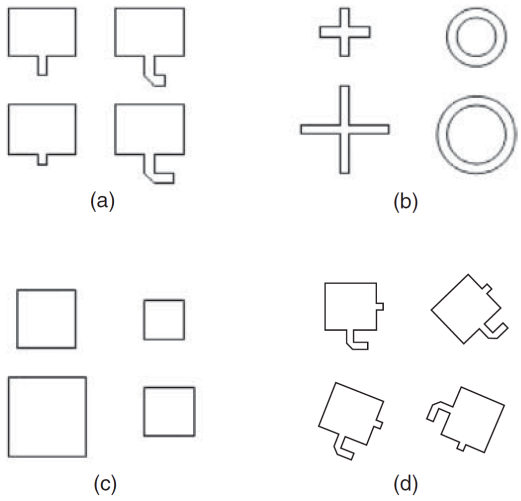

Figure 2.4: Various reflectarray elements, (a) identical patches with variable-length phase delay lines, (b) variable-size dipoles or loops, (c) variable-size patches, (d) variable angular rotations. [35]

Different types of PEs provide different scattering impedances and, thus, different phases to compensate for the different feed-path delays.

As depicted in Figure 2.4 it is possible to use

- identical patches with variable-length phase delay lines
- variable-size dipoles or loops
- variable-size patches
- variable angular rotations.

Using identical patches with variable-length phase delay lines (Figure 2.4(a)) it is possible to control the phase delay of the different paths illuminated by the feed by changing the length of the stub line attached to the patches, with the patch dimensions that must be suitably chosen to resonate at the incident wave frequency; with variable-size dipoles or loops (Figure 2.4(b)) it is possible to change the the feed-path delay by changing the dimension of the patches, varying the scattering impedance accordingly. Rotating the patches with different angles (Figure 2.4(d)) it is possible to change the delay of the elements for circular polarization of the impinging field. The most common strategy is to design patch elements with variable size (Figure 2.4(c)), for example using a square shape (the so called *square patches*) in order to get the desired phase delay. Ideally, a single resonance can provide a complete phase cycle of 360°, however, in practice, the total achievable phase will be lower ($\approx$ 300°) due to a number of factors such as the cell size (separation between patches), the substrate thickness and material. The relation between the patch sizes and the provided phase change in the reflected wave is strongly non linear, since a rapid variation is achieved near the resonant frequency and a slower one at the edges of the dimension interval. This is why the phase change versus element size diagram is called *S-curve*, to highlight this behavior. An example is shown in Figure 2.5.

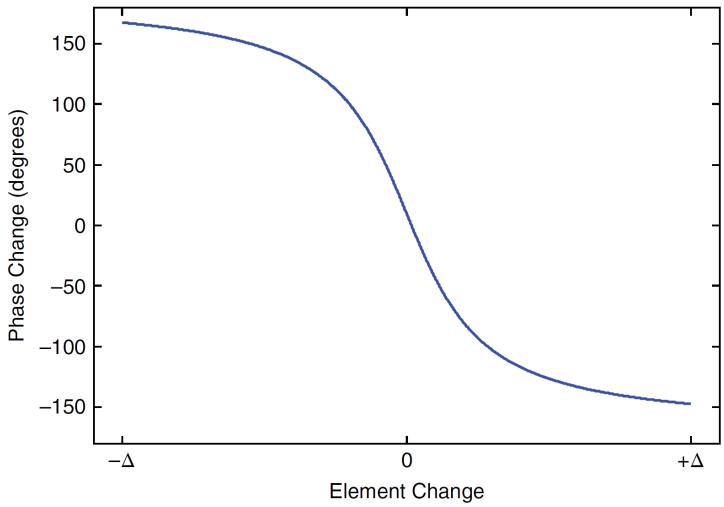

Figure 2.5: Example of S-curve for variable size patches. [37]

Besides square patches, it is also possible to use any other shape wish to provide sufficiently large phase interval, as presented in the following. In addition, multiple resonances of the patch elements can be exploited to achieve even larger phase delays.

2.3 Advantages of printed Reflectarray

Printed RAs have many advantages as anticipated in 2.1. They are lightweight, small with low profile thanks to the printed patches and pretty cheap due to the low cost manufacturing of PCBs using etching processes. Additionally, due to their shape, there is no need for power dividers which leads to very low resistive *Insertion Loss* and an efficiency greater than 50%. Electronic phase shifters can be incorporated in the elements and, thanks to this beam scanning capability, there is no need for complicated and very expensive beamforming networks. A sufficiently large tilt angle of the main beam can be achieved with proper design. For spacecraft applications, reflectarrays can be made foldable, in order to reduce their dimension ($\approx$ 10 meters) and also inflatable antennas can be deployed to simplify the opening procedure. Some test have been done to integrate RAs with solar cells [38] to reduce the occupied space. These antennas can work with μm-wave and mm-wave frequencies ans, similarly to parabolic reflectors, with multiple feed elements at the

focal area of the antenna.

2.4 Disadvantages of printed Reflectarray

The most important disadvantage is the very narrow bandwidth of the reflectarray, around 10%. With respect to them, parabolic reflectors have an almost (theoretical) infinite bandwidth which allows the latter to be used for certain applications. The bandwidth of RAs is essentially limited by two factors as anticipated in 2.1:

1. the narrow bandwidth of the patch element itself on the reflectarray surface
2. the differential spatial phase delay.

The two will be now analyzed in details. The first point regards the very small bandwidth of the PEs, around 3-5%. To achieve wider bandwidth there are many solutions, for example using a thicker substrate (up to 15% bandwidth can be achieved) or using multiple layer implementations.

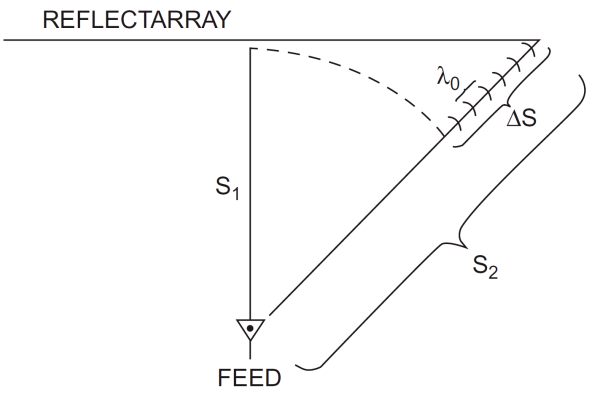

Figure 2.6: Differential spatial phase delay of reflectarray. [35]

The second point requires more attention. Referring to Figure 2.6, it is possible to observe that the distance between two different elements on the antenna surface with respect to the feed antenna is not the same. In fact, the distance S_1, between the feed and the central element is much smaller compared to S_2, which is the distance between the feed and an element on the reflectarray side. The path difference can be expressed by

$$\Delta S = S_2 - S_1 = (N + d) \cdot \lambda \tag{2.1}$$

where N is an integer, d is a fractional number and λ is the free-space wavelength. In order to reduce the path difference the parameter d must be compensated, for example, choosing the right size of the patches, to get the required phase shift. However, also with this solution, the problem is still present when a small frequency variation takes place. In fact, if $f \to f + \Delta f$ implies $\lambda \to \lambda + \Delta\lambda$ which means

$$\Delta S = (N + d) \cdot \lambda \Rightarrow \Delta S' = (N + d) \cdot (\lambda + \Delta\lambda) \tag{2.2}$$

and the implemented compensation does not work anymore. The error is

$$\Delta S' - \Delta S = (N + d) \cdot \Delta\lambda \tag{2.3}$$

that can be a quite large portion of a wavelength or 360°.

At this point, other solutions can be used to reduce the above-mentioned error.

Firstly, the parameter N must be reduced; a RA with an higher focal length-to-diameter ratio (f/D) can be exploited in order to reduce the path difference ΔS. Another solution simply consists in the usage of smaller aperture antennas. If patches with delay lines are used, a compensation line of $(N + d) \cdot \Delta\lambda$ instead of $d\Delta\lambda$ can be engaged as delay line, but an additional insertion loss will be present.

A rarely adopted solution is to make use of a concavely curved surface RA with piecewise flat approximated surfaces instead of the standard flat one, as in [39], [40]. With respect to the curved parabolic reflectors, the *conformal* RAs, reach larger beam scanning angles using phase shifters inserted into each radiating element. For space applications, piecewise flat surfaces, are also easier to be folded, in order to reduce the occupied volume.

2.5 Introduction to Conformal Reflectarray Antenna

A Conformal Reflectarray antenna can be seen as a reflectarray bent around a curved surface, as, for instance, a cylinder with a given radius of curvature R. An

example is shown in Figure 2.7.

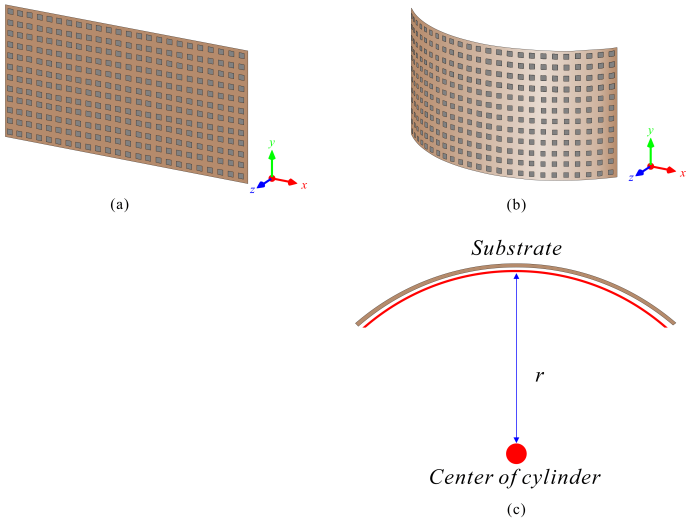

Figure 2.7: Planar reflectarray (a), convex conformal reflectarray (b) and cross-section of the convex conformal reflectarray with the description of the radius of curvature R (c). [41]

There are two possible types of Conformal Reflectarrays, as shown in Figure 2.8: the *concave* and the *convex* one. The first one is similar to a parabolic antenna and therefore it has performance generally better than that of a planar configuration, but it is less interesting from the application point of view.

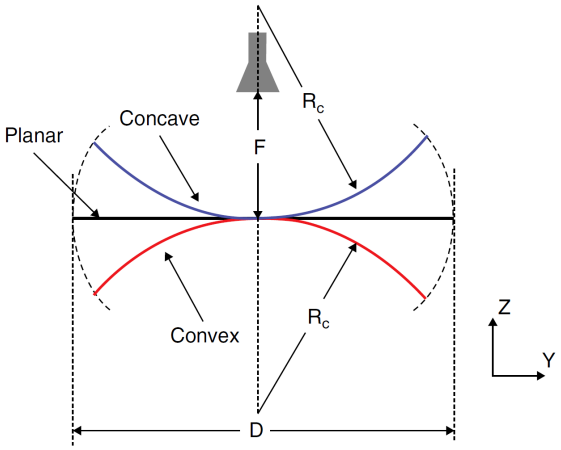

Figure 2.8: Cross-section of the concave and convex conformal cylindrical reflectarray systems. [42]

Vice versa, a *Convex* RA (CRA in the following) has more potential applications, since it can be integrated in parts of an airplane, high-speed train, or other vehicle. In the case of the antennas mounted on the fuselage of an aircraft, the use of CRAs represents a good alternative to other configurations, since it allows an easy placement of both feed and reflecting surface, a good integration and camouflage on the structure where they are located, including the possibility of beam scanning[43] with full azimuth and wide elevation coverage.

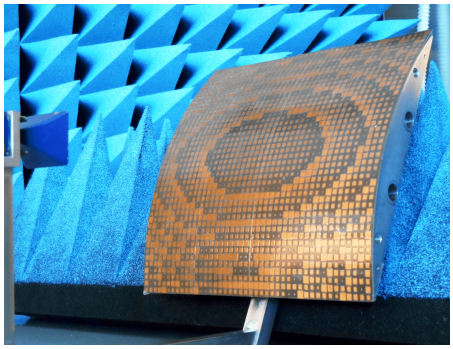

Figure 2.9: A fabricated convex conformal reflectarray antenna with square patch elements. [43]

2.6 Reflectarray analysis

Good characterization of phase shift and dissipative losses for each polarization on the incident field must be done to get the desired behavior of the antenna. When the RA is illuminated by a feed, a collimated or shaped beam is generated by its elements. An example of *pencil beam* is shown in Figure 2.10.

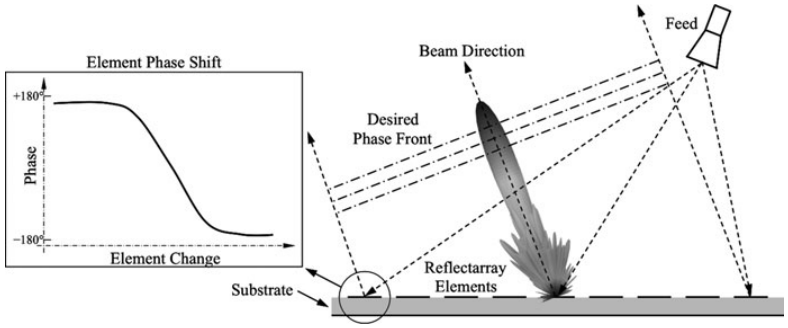

Figure 2.10: Example of S-curve and reflected beam for a RA. [44]

To produce a tilted reflected beam it is necessary to choose proper phase delay value for the PEs, for example, adjusting their sizes.

Usually, the feed horn is modeled as a $\cos^q(\theta)$ function, but specific simulations and characterizations can be done to evaluate its specific radiation pattern.

2.6.1 Single patch element characterization

In order to analyze the behavior of the whole antenna, it is mandatory to start from the single element characterization (the UC). As already stated in the previous parts, an S-curve diagram with the reflection coefficient phase change versus physical parameter for a certain UC must be obtained, with orthogonal or oblique plane wave incidence. The *infinite array model* can be used, applying the Floquet's theorem. The latter implies the analysis of only one periodic cell array, infinitely extended, as in Figure 2.11, which provides a good prediction of the real mutual coupling between two different cells.

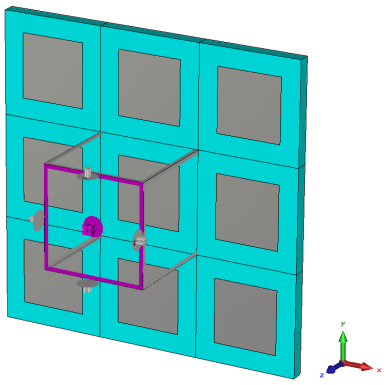

Figure 2.11: Unit cell and nearest neighbors cells.

For example, a unit cell with the following parameters has been designed and analyzed using the *CST Microwave Studio* software [45]:

- Design frequency $f = 11.725$ GHz

Substrate parameters:

- Substrate thickness 1.6 mm

- Substrate $\varepsilon_r = 3.92$ (FR-4, $\tan(\delta) = 0.0125$)
- Cell size (substrate width) $px = py = \dfrac{\lambda}{2} \approx 12$ mm

Patch parameters:

- Metal width W (variable)
- Metal thickness 0 mm (PEC)

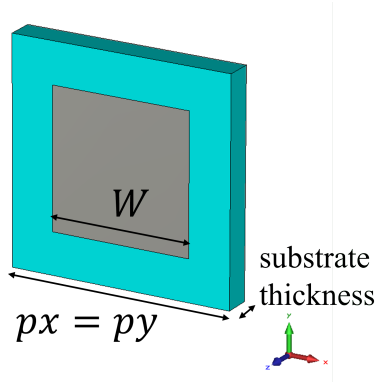

Figure 2.12: Designed unit cell with square patch.

Figure 2.12 shows the designed UC with the related parameters.

The obtained S-curve for this UC is depicted in Figure 2.13, with variable W from 2 to 8 mm.

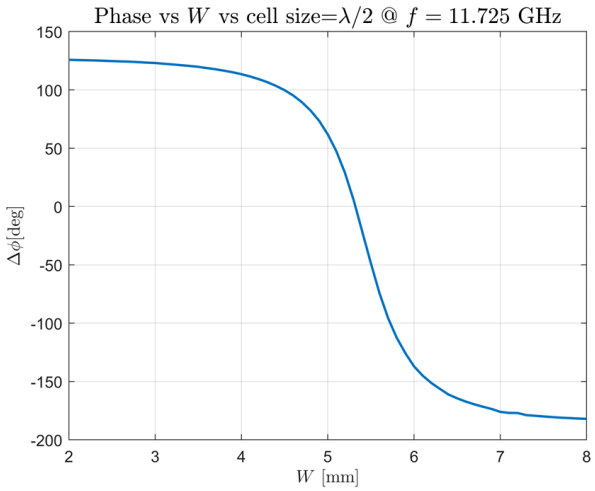

Figure 2.13: Obtained S-curve for the designed unit cell with square patch.

By varying the cell size ($\lambda/2$, 0.4λ and $\lambda/3$), with $W \in [2,8]$ mm, it is possible to obtain different phase curves, at 11.725 GHz, as shown in Figure 2.14.

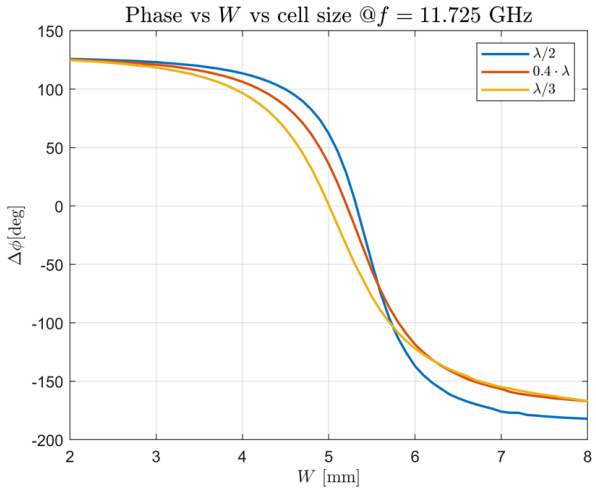

Figure 2.14: Obtained S-curves for the designed unit cell with different cell sizes.

Also the substrate thickness can be changed which leads to different phase change behaviors, as in Figure 2.15, where the cell size is fixed to $\lambda/2$, the patch size is $W = 5.4$ mm, varying the frequency from 10.725 to 12.725 GHz and the substrate thickness from 1.5 to 3.5 mm with 0.5 mm step.

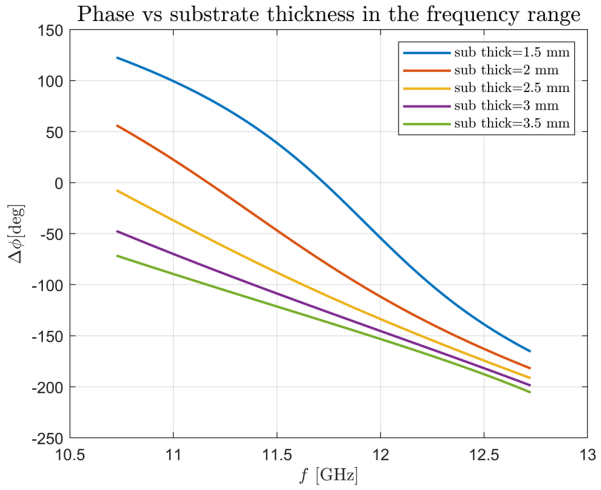

Figure 2.15: Obtained S-curves for the designed unit cell with different substrate thicknesses.

2.6.2 Required phase distribution

To produce a reflected beam in a specific direction defined by two angles (θ_b, ϕ_b) it is necessary to provide a progressive phase distribution for each array element.

Figure 2.16 depicts the geometry of the reflected beam.

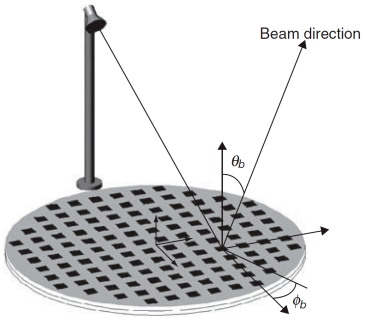

Figure 2.16: Reference system for the phase distribution evaluation. [35]

2.6.2.1 Planar case phase distribution

From array theory, to get a beam in a certain direction for a planar reflectarray antenna, the required phase distribution can be evaluated with

$$\phi(x_i, y_i) = -k_0 \sin\theta_b \cos\phi_b \, x_i - k_0 \sin\theta_b \sin\phi_b \, y_i \tag{2.4}$$

with $k_0 = 2\pi/\lambda$ the propagation constant in vacuum and (x_i, y_i) the coordinates of the i-th element in the array with respect to the antenna center.

The phase of the reflected field from the antenna is the sum of the phase change due to the feed phase center distance with respect to the RA (called d_i) and the phase shift introduced by each element, in mathematical form:

$$\phi(x_i, y_i) = -k_0 \, d_i + \phi_R(x_i, y_i) \tag{2.5}$$

being $\phi_R(x_i, y_i)$ the required phase at each element.

Therefore, it is possible to derive the latter from 2.4 and 2.5 as

$$\phi_R(x_i, y_i) = k_0(d_i - (x_i \cos\phi_b + y_i \sin\phi_b)\sin\theta_b) \tag{2.6}$$

It is possible to evaluate the required phase shift for each element by computing

2.6 for example with *Matlab*. For centered focal point and a reflected pencil beam orthogonal to the antenna surface, a 24×24 elements square RA requires the phase distribution shown in Figure 2.17, at a frequency $f = 30$ GHz and cell size equal to 0.45λ.

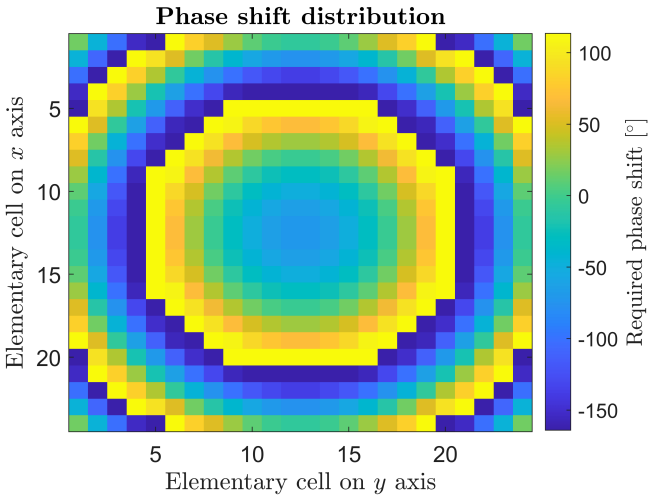

Figure 2.17: Required phase distribution for a square 24×24 planar RA.

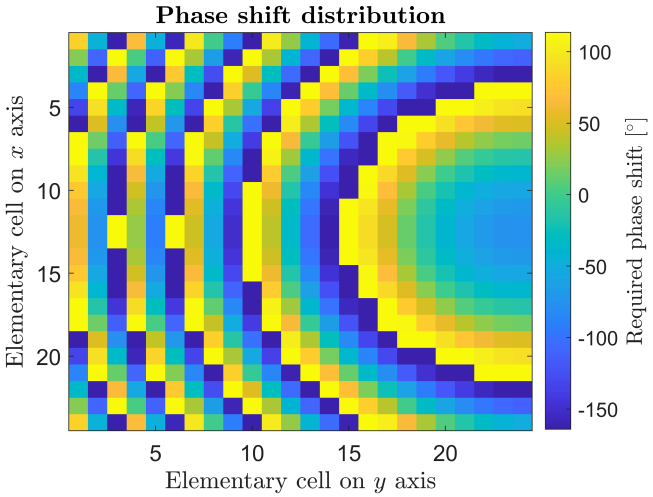

Figure 2.18: Required phase distribution for a square 24×24 planar RA with tilted beam.

For $\theta_b = 25°$, i.e. tilted beam with respect to the vertical coordinate, the required phase distribution is shown in Figure 2.18: it is possible to observe the different

pattern of the diagram.

As an example, by using an S-curve similar to the one provided in Figure 2.13 (obtained for a specific UC, i.e. with certain materials, dimensions, etc), it is possible to obtain the patch size distribution of Figure 2.19 for the designed RA with the phase distribution of Figure 2.17, that will be printed on the chosen substrate to realize the complete antenna.

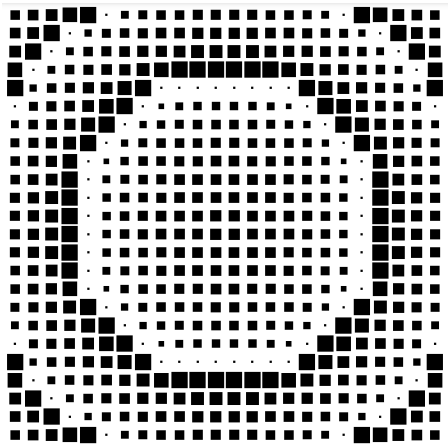

Figure 2.19: Required patch size distribution for a square 24×24 planar RA.

2.6.2.2 Conformal case phase distribution

For the convex conformal case (CRA) the reference system is depicted in Figure 2.20.

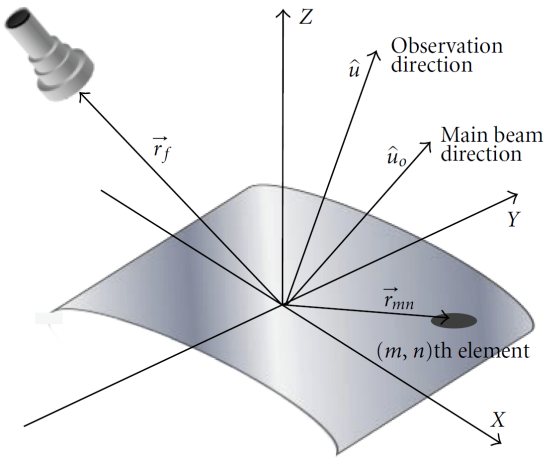

Figure 2.20: Reference geometry for the phase distribution of a CRA. [42]

Due to the curved surface of a convex conformal reflectarray antenna, the phase evaluation becomes a 3D problem instead of the 2D problem of the planar case. In this case, also the "elevation" of the unit cell element must be considered, i.e. the z component of the system in Figure 2.20.

With these assumptions, one can modify the planar formula in 2.6 by adding the above mentioned z component, using trigonometry, as

$$\phi_R(x_i, y_i) = k_0(d_i - (x_i \cos\phi_b + y_i \sin\phi_b)\sin\theta_b - z_i \cos\theta_b) \tag{2.7}$$

By using the same parameters of the RA in Figure 2.17, it is possible to evaluate now the phase distribution of a conformal reflectarray antenna, for example, varying the radius of curvature R.

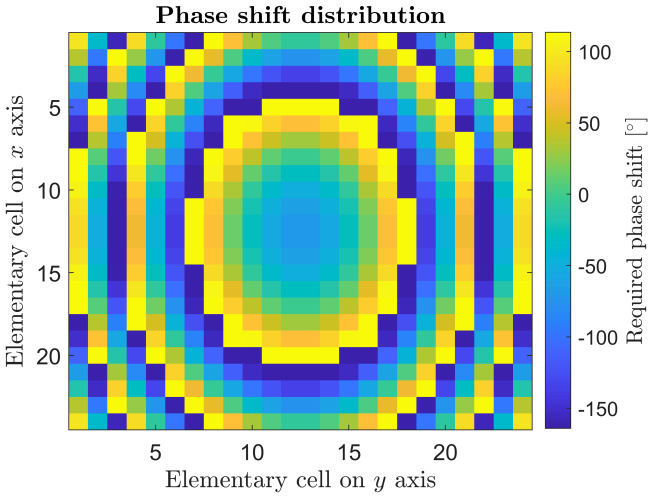

Figure 2.21: Required phase distribution for a square 24×24 CRA with radius of curvature $R = 20\lambda$.

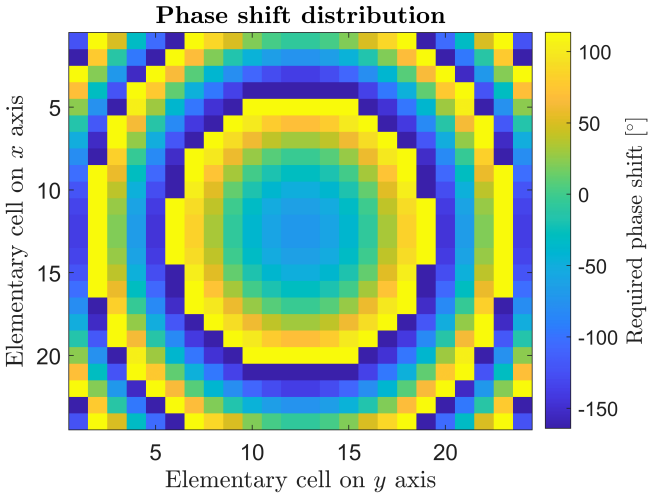

Figure 2.22: Required phase distribution for a square 24×24 CRA with radius of curvature $R = 40\lambda$.

It is possible to see from Figure 2.21 and 2.22 that for large radii of curvature the phase distribution of the conformal case is approximately the same as the planar case, while for smaller radii, the curvature of the surface will be much more accentuated. As a consequence, the distance between the elements and the feed antenna will be very different with respect to the planar case and therefore

the phase distribution will vary accordingly. The patch size distribution for the designed CRA with the phase distribution of Figure 2.21, that will be printed on the chosen substrate to realize the complete antenna, is shown in Figure 2.23.

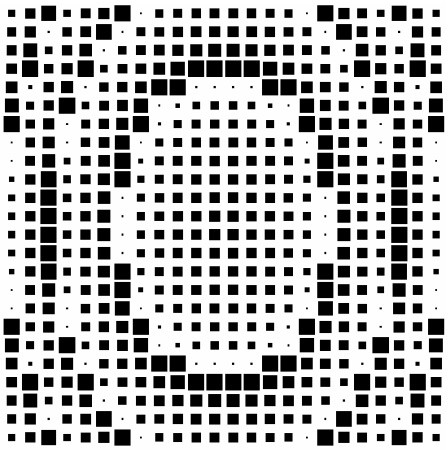

Figure 2.23: Required patch size distribution for a square 24×24 CRA.

2.6.3 Radiation analysis technique

As outlined in the previous section, the challenge here is that electrically large surfaces as the reflectarray antenna, made up of thousands of elements with dimensions smaller than the wavelength, requires a very high computational time and resources for the full-wave analysis. Despite this drawback, the full-wave analysis approach is generally considered to be the most accurate technique to obtain the current distributions on the reflectarray elements. Once they are obtained, far-field transformations of the currents are exploited for the total array and the radiation pattern can be evaluated.

Although a full-wave analysis is required at the final stage of the antenna design, one can use an approximated computation approach with faster and low time consuming performance at least for the initial design part.

The method presented in the following exploits the *array theory*: the radiation pattern is evaluated by summation of the single element excitation vector function.

2.6.3.1 Planar radiation analysis

Modeling the feed antenna radiation pattern with a simple model, as rotationally symmetric, given by

$$E^F(\theta_f, \varphi_f) = \begin{cases} \cos^q(\theta_f) & \text{for } 0 \leq \theta_f \leq \pi/2 \\ 0 & \text{elsewhere} \end{cases} \tag{2.8}$$

where θ_f is the elevation angle and q is the *feed power pattern*, it is possible to evaluate the total radiation pattern as the sum of the single elements radiation patterns. These can be also modeled as a cosine q function:

$$E^E(\theta_p, \varphi_p) = \begin{cases} \cos^q(\theta_p) & \text{for } 0 \leq \theta_p \leq \pi/2 \\ 0 & \text{elsewhere} \end{cases} \tag{2.9}$$

with θ_p the elevation angle in local coordinates on the antenna aperture.

With the conventional array theory, the radiation pattern of a 2D planar with M×N elements array can be written as

$$\vec{E}(\hat{u}) = \sum_{m=1}^{M} \sum_{n=1}^{N} \vec{A}_{mn}(\hat{u}) \cdot \vec{I}(\vec{r}_{mn}) \tag{2.10}$$

with

$$\hat{u} = \hat{x} \sin\theta \cos\varphi + \hat{y} \sin\theta \sin\varphi + \hat{z} \cos\theta \tag{2.11}$$

where the coordinate reference systems are depicted in Figure 2.24 and 2.25.

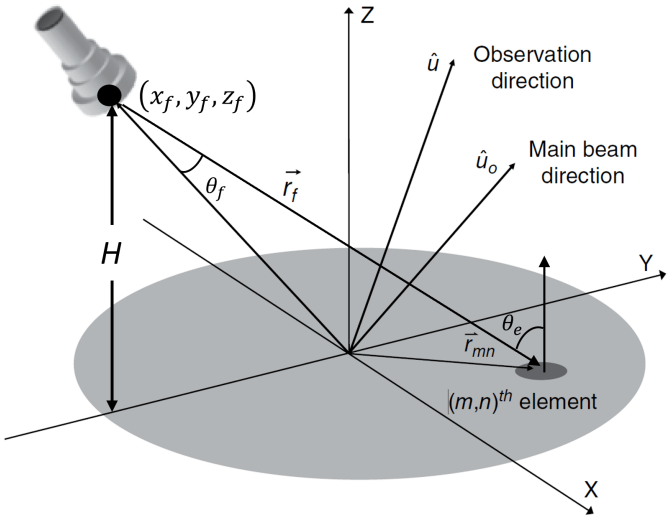

Figure 2.24: Coordinate system for the array theory method. Adapted from [37]

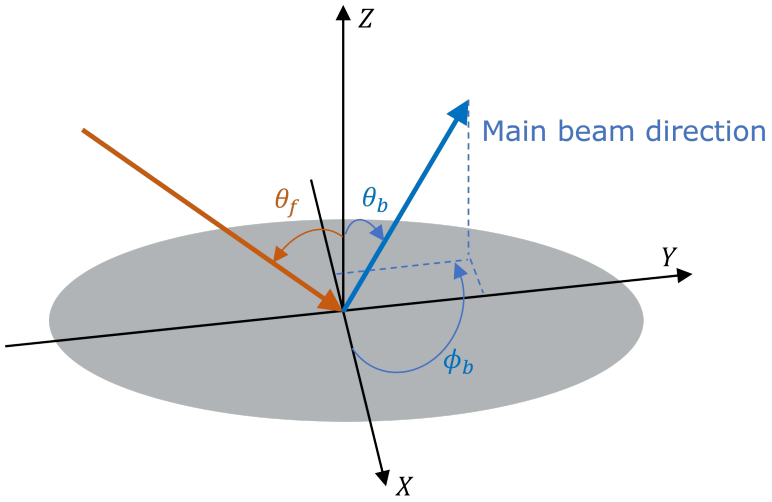

Figure 2.25: Coordinate system for the feed and main beam directions.

With respect to the spherical coordinates:

- θ_f depends on the considered case
- $\phi_f = 270°$
- θ_b depends on the considered case

- $\phi_b = 90°$

The other parameters are

- $\vec{A}$ is the element pattern vector function
- $\vec{I}$ is the element excitation vector function
- $\hat{r}_{mn}$ is the position vector of the mn-th element.

To simplify calculations, one can approximate $\vec{A}$ with a scalar function A with no azimuthal dependency as

$$A_{mn}(\theta, \varphi) \approx \cos^{q_e}(\theta) \cdot e^{jk(\vec{r}_{mn} \cdot \hat{u})} \tag{2.12}$$

ad the element excitation function $\hat{I}$ as

$$I(m,n) \approx \frac{cos^{q_f}\theta_f(m,n)}{|\hat{r}_{mn} - \hat{r}_f|} \cdot e^{-jk(|\vec{r}_{mn} - \hat{r}_f|)} \cdot |\Gamma_{mn}| e^{j\phi_{mn}} \tag{2.13}$$

by considering the feed as a cosine q function as in 2.8, where $|\hat{r}_{mn} - \hat{r}_f|$ is the Euclidean distance between the feed and the element and θ_f the spherical angle in the feed coordinate system.

the receive mode pattern of the element is taken into account by $|\Gamma_{mn}|$, which can also be approximated by a cosine q_e function, as in 2.9, using local element coordinates, as

$$|\Gamma_{mn}| = \cos^{q_e}\theta_e(m,n) \tag{2.14}$$

This value is directly obtained by the unit cell analysis.

With reference to Figure 2.24, the ϕ_{mn} parameter, i.e. the required phase delay of the mn-th element, fix the main beam direction $\hat{u}_o$. If local periodicity approximation is taken into account, it does contain the mutual coupling effects, as anticipated in 2.6.1.

With the approximations in 2.12, 2.13 and 2.14, the radiation pattern in 2.10 becomes

$$E(\theta,\varphi)=\sum_{m=1}^{M}\sum_{n=1}^{N}\cos^{q_e}\theta\cdot\frac{cos^{q_f}\theta_f(m,n)}{|\hat{r}_{mn}-\hat{r}_f|}\cdot e^{-jk(|\vec{r}_{mn}-\hat{r}_f|-\hat{r}_{mn}\cdot\hat{u})}\cdot\cos^{q_e}\theta_e(m,n)e^{j\phi_{mn}} \tag{2.15}$$

In general, the array theory formulation will yield good main beamwidth, beam direction, and general pattern shape; it also allows for program development and fast computational time. However, the cosine q model does not account for the polarization of the feed horn and the elements, therefore the cross-polarization is not modeled in this procedure.

2.6.3.2 Conformal radiation analysis

The formulation developed for planar reflectarray antennas can be generalized to analyze the performance of conformal reflectarrays. The array summation technique can still be used if the elements on the conformal surface are correctly modeled, including the mutual coupling.

The reference system is the same used in the phase distribution evaluation, depicted in Figure 2.20. The radiation pattern of a conformal reflectarray with M×N elements can be calculated using the vectorized array summation formulation used for the planar case, although with some adjustments.

If the surface is not highly curved, one can approximate each unit cell with a planar surface tangential to the conformal surface.

For the element pattern modeling there are two important considerations:

- for the receiving mode pattern, the exact angle of incident must be evaluated for each element;
- for the transmitting mode pattern, the correct orientation of the local cell coordinate with respect to the global ones must be considered.

With these assumptions the element pattern function A can be written as

$$A_{mn}(\theta,\varphi)\approx\cos^{q_e}(\theta_{\text{local}})\cdot e^{jk(\vec{r}_{mn}\cdot\hat{u})} \tag{2.16}$$

which is the same formulation of the planar case (in 2.12) but using local coordinates for the radiating element.

The receive mode pattern is the same of the planar case (in 2.14) but with θ_e that depends on the element location and on the surface orientation too.

Finally, the radiation pattern of a conformal reflectarray can be written as

$$E(\theta,\varphi) = \sum_{m=1}^{M}\sum_{n=1}^{N} \cos^{q_e}\theta_{\text{local}} \cdot \frac{cos^{q_f}\theta_f(m,n)}{|\hat{r}_{mn} - \hat{r}_f|} \cdot e^{-jk(|\vec{r}_{mn}-\hat{r}_f|-\hat{r}_{mn}\cdot\hat{u})} \cdot \cos^{q_e}\theta_e(m,n)e^{j\phi_{mn}} \tag{2.17}$$

which is, formally, similar to the planar case (in 2.15 where θ_f is the spherical angle in the feed coordinates, $\hat{r}_f$ is the position vector of the feed, the required phase delay ϕ_{mn} of the mn-th element is adjusted to tilt the main beam in the $\hat{u}_o$ direction) but using the unit cell local coordinates.

The radiation pattern of a conformal reflectarray for various radii of curvature is shown in Figure 2.26, where the feed parameters are $q_f = 6.5$, $f/D = 0.75$ (f is the feed-antenna distance and D is the physical antenna aperture), the element is modeled with $q_e = 1$ and $R_C = \infty$ refers to the planar case.

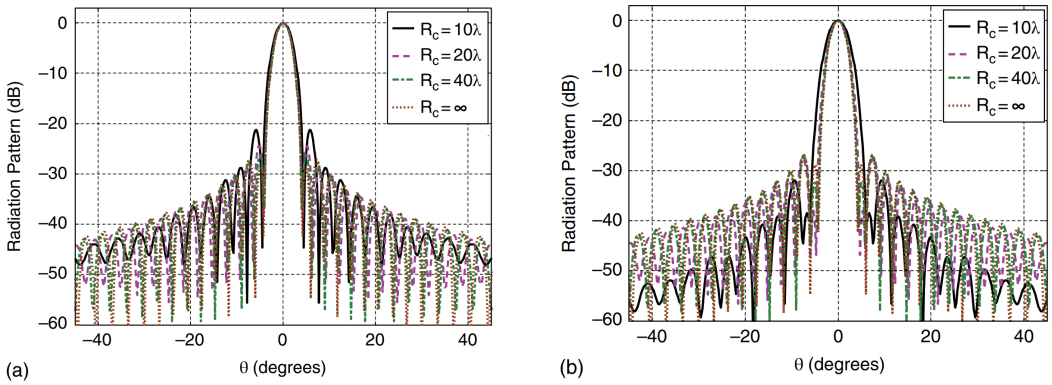

(a) Concave case **(b)** Convex case

Figure 2.26: Radiation patterns of cylindrical reflectarrays. [37]

It can be seen that the convex design produces higher *Side Lobe Levels* (SLLs) with respect to the planar case while the concave design has lower SLLs and presents a much wider bandwidth.

2.7 Reflectarray practical design approach

As already highlighted in Section 2.6, the design of the single unit cell must be optimized in order to get the desired scattering from the feed signal with the required far-field beam efficiency.

2.7.1 Single element parameters

There are five important parameters that govern the element selection that will be presented in the following.

2.7.1.1 Element reflection phase

The element reflection diagram (S-curve) is desirable to have minimum slope at the center to reduce the sensitivity to fabrication tolerances and frequency variations and a theoretical $\pm 180°$ phase change in the patch size variation interval. For this evaluation, the approximation with the infinite array approach can be used, supposing all identical elements, using Floquet modes.

2.7.1.2 Element beamwidth

The element beamwidth must be correctly adjusted with respect to the f/D value in order to accommodate most incident angles from the feed. An illustration is provided in Figure 2.27. If the elements have a small beamwidth, for an antenna with small f/D, the edge elements do not receive energy effectively from the illuminating feed.

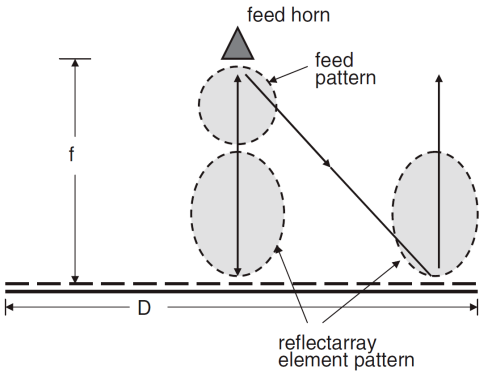

Figure 2.27: Element beamwidth illustration. [35]

2.7.1.3 Element bandwidth

As already highlighted in the introduction of this work, the microstrip patch elements have very small bandwidth (around $3-5\%$) that can be enlarged by using multiple layers up to 15%.

2.7.1.4 Element reflection efficiency

In a reflectarray the energy is scattered back due to the presence of the ground plane. There are three different scattered components:

- the *re-radiated component* due to the patch resonance;
- the *specular reflected component* due to the ground plane;
- the *scattered component* due to the non-resonant structures of the patches.

Due to the small thickness of the substrate (around 0.1λ) the first two are predominant. A reflectarray is made up of different size patch elements: this means each of them will resonate at a different frequency and only the one with a particular size will resonant at the desired frequency f_0. Only the resonant dimension patches have the complete re-radiated energy, while the others will back-scatter both re-radiated and reflected energy, contributing to an higher inefficiency.

Apart from the different size of the elements, also the position is very important. In fact elements located at the center of the antenna will have both re-radiated and

reflected waves in the same direction while edge elements have only the re-radiated component along the main beam direction. The reflected component will be in a different direction with respect to the main beam: this contributes to the sidelobes generation and a general inefficiency of the system. A representation of the problem is available in Figure 2.28.

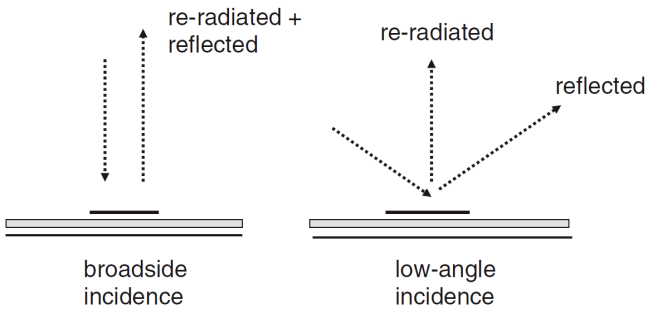

Figure 2.28: Element reflected and re-radiated waves representation with a focus (on the right) on the edge elements small angle problem. [35]

To minimize this waste of energy one can design an antenna with large f/D ratio (i.e. larger feed distance f or smaller antenna aperture D) and minimize the reflection component.

2.7.1.5 Element spacing

The final parameter is the element spacing. All the elements must be separated by a proper distance d to avoid grating lobe type of radiation. The general design formula is

$$\frac{d}{\lambda} \leq \frac{1}{1+\sin\theta} \tag{2.18}$$

where d is the separation of the elements and θ is the incident angle between the feed radiation and the element position on the antenna surface.

for central element, perpendicular incidence implies $\theta \approx 0°$ and therefore $d \lessapprox 0.95\lambda$ while for edge element with angled incidence (around 45°) the required spacing is $d \lessapprox 0.6\lambda$.

Usually the same spacing value is kept for the entire antenna; as a worst case scenario, the smaller d condition (i.e. the one of the edge elements) is considered.

Grating lobes are formed due to the different incident angles of the center elements with respect to the edge ones; the element spacing must be appropriately design in order to avoid energy waste, for example with a large f/D value.

2.7.2 Reflectarray geometry design

The choice of the proper reflectarray geometrical dimensions yields to a good efficiency of the antenna.

There are many degrading factors taken into account account in the total reflectarray efficiency: the most important ones will be analyzed in the following.

2.7.2.1 Illumination efficiency

Illumination efficiency is a measure of the uniformity of the feed illumination of the reflectarray[46].

The mathematical expression is given by

$$\eta_I = \frac{1}{\pi a^2} \frac{\left[\int_0^{2\pi}\int_0^a |E_y(\rho,\phi)|\rho\, d\rho\, d\phi\right]^2}{\int_0^{2\pi}\int_0^a |E_y(\rho,\phi)|\rho\, d\rho\, d\phi} \tag{2.19}$$

assuming that the aperture field is $y-$polarized and the aperture is circular with radius a. The illumination also depends on the radiation pattern of the constituent elements of the reflectarray: the broadside of the single element leads to a reduced intercepted power from the feed when it is illuminated with rays from the feed that are away from this broadside direction.

2.7.2.2 Spillover efficiency

The *spillover efficiency* is defined as the percentage of radiated power from the feed that is intercepted by the reflecting aperture with respect to the total radiated power, in mathematical form:

$$\eta_s = \frac{\int_0^{2\pi}\int_0^{\psi/2} |g(\theta,\phi)| d\theta\, d\phi}{\int_0^{2\pi}\int_0^{\pi} |g(\theta,\phi)| d\theta\, d\phi} \tag{2.20}$$

being ψ the subtended angle of the reflectarray and $g(\theta, \phi)$ the feed radiation pattern as reported in Figure 2.29.

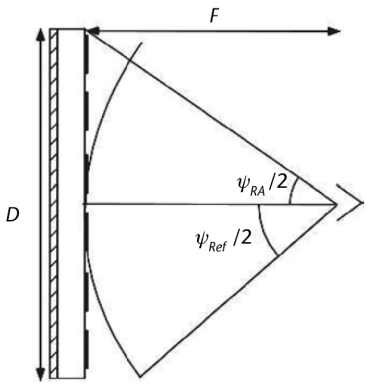

Figure 2.29: Side view of the reflectarray for the spillover efficiency definition, with $\psi_{RA} = \psi$. [46]

2.7.2.3 Aperture efficiency

The *aperture efficiency* is defined as

$$\eta_a = \eta_I \cdot \eta_s \tag{2.21}$$

being η_I the *illumination efficiency* and η_s the *spillover efficiency*. As an example, the efficiencies for an half-meter 32 GHz circular aperture reflectarray with a fixed f/D ratio of 1 versus the feed pattern factor q (feed beamwidth) are presented in Figure 2.30.

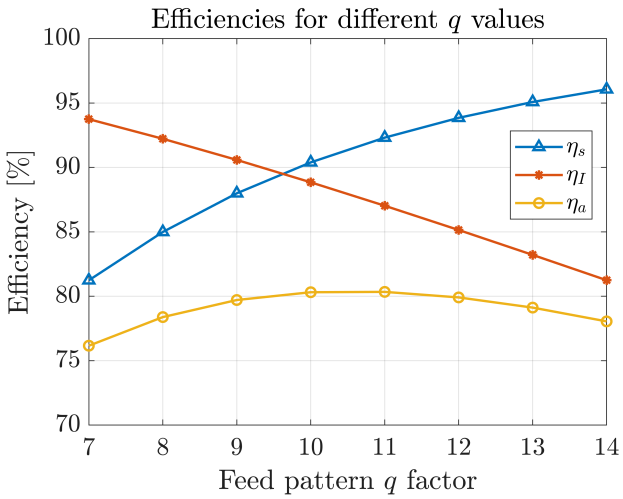

Figure 2.30: Spillover and illumination efficiencies versus feed pattern shape.

From Figure 2.30 it is possible to see that the maximum aperture efficiency is achieved for $q \simeq 10.5$ for this specific antenna.

As a general rule, a reflectarray becomes more efficient for larger electrical apertures but its bandwidth will be reduced.

For a $\cos^q(\theta)$ feed pattern, the spillover efficiency can be written as

$$\eta_s = 1 - \cos^{q+1}(\psi_{RA}/2) \tag{2.22}$$

being ψ_{RA} the subtended angle as in Figure 2.29.

The illumination efficiency for a reflectarray illuminated by the same feed pattern is

$$\eta_I = \frac{2q}{\tan^2(\psi_{RA}/2)} \frac{(1 - \cos^{q/2-1}(\psi_{RA}/2))^2}{\left(\frac{q}{2} - 1\right)^2 (1 - \cos^q(\psi_{RA}/2))} \tag{2.23}$$

The aperture efficiency can be evaluated with 2.21 and a representation of it for different q values is provided in Figure 2.31.

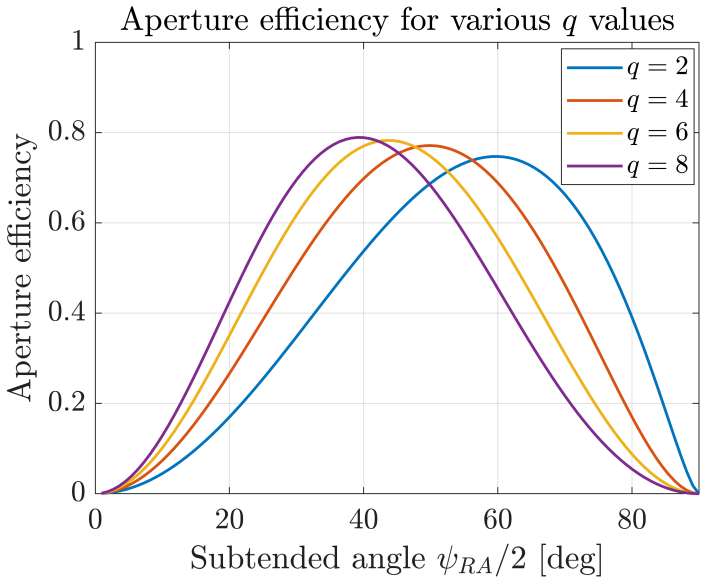

Figure 2.31: Aperture efficiency for different q values of the feed pattern.

There is an optimum f/D ratio for which the aperture efficiency is maximized; in other terms there is an optimum subtended angle to maximize. The relation between the subtended angle and the f/D parameter, referring to Figure 2.29, can be derived using trigonometry as

$$\frac{\psi_{RA}}{2} = \arctan\left(\frac{D}{2f}\right) \tag{2.24}$$

2.7.2.4 Blockage efficiency

The *blockage efficiency* refers to the block of the field radiation due to the feed assembly (the so called *feed blockage* or *aperture blockage* phenomenon). For this reason the gain is reduced, SLLs are enhanced and the overall performance are worsen. This adverse effect can be computed using

$$\eta_b = \frac{1}{\pi a^2} \frac{\left| \int_0^{2\pi} \int_0^b E_y(\rho, \phi) \rho \, d\rho \, d\phi \right|^2}{\rho \, d\rho \, d\phi} \tag{2.25}$$

where a is the circular antenna radius and b the radius of the feed region. In case of center-fed reflectarray antenna one can design the reflected beam in a different

direction with respect to the feed assembly: in this case the blockage effect can be almost completely avoided. Additionally, offset-fed configuration can be used to further mitigate this phenomenon.

The problem can be immediately pointed out in Figure 2.32.

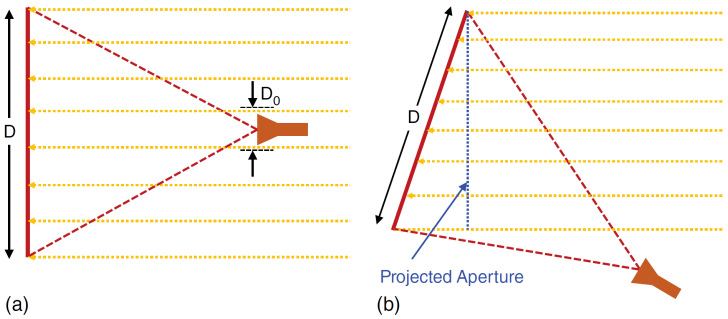

Figure 2.32: Aperture blockage in front-fed reflectarray systems: (a) symmetric, (b) offset. [37]

As depicted in Figure 2.32 (a) there is a *blockage diameter* D_0 due to the presence of the feed itself in the field radiation region for the symmetric (center) feed configuration. With the offset-fed configuration in Figure 2.32 (b) it is clear that the feed does not cause problems anymore, therefore a great advantage over the symmetric configuration is earned.

2.7.2.5 Dielectric and conductor loss

The *dielectric and conductor loss* account for the non ideality of the the dielectric substrate and conductor material used. The total *loss factor* can be written as

$$\eta_l = \frac{\sum_{n=1}^{N} |\Gamma_n|^2}{N} \tag{2.26}$$

being N the total number of elements on the reflectarray structure, each of them with a Γ_n reflection coefficient (in a realistic case, smaller than unity).

When the metal conductivity (refer to Appendix A for the material characteristic definitions) is above a certain limit or the dielectric loss tangent is below a certain value, the phase of reflection coefficient varies with a 360° range. In this situation,

when the conductor and dielectric losses increase but do not exceed the limit, the element loss will increase, but it will not affect the phase range[37]. If this is not true, a new limited angular phase range can be observed.

2.7.3 Reflectarray design step-by-step procedure

The general step-by-step design procedure for a reflectarray antenna (both planar and conformal) is illustrated in the following diagram.

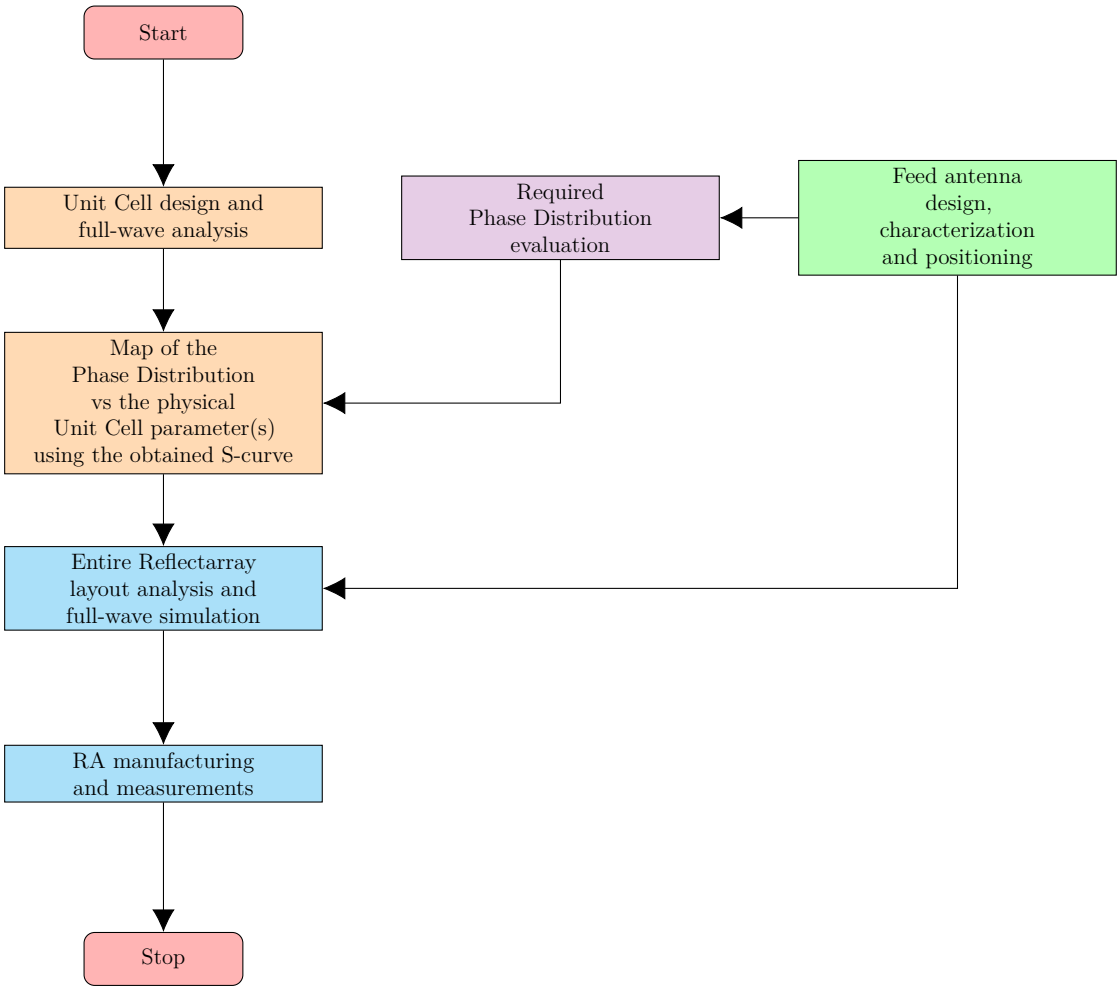

Figure 2.33: RA design flowchart.

Now, each of the blocks in Figure 2.33 will be analyzed separately.

1. **Unit Cell design and full-wave analysis**: the unit cell design is strictly connected to its full-wave analysis. Once a geometry is defined and the substrate is selected, the choice of the geometrical parameter(s) to use for controlling the variation of the reflection coefficient is done through the full-wave analysis of the unit cell, embedded in a periodic lattice and illuminated by an incident plane wave. In this way it is possible to evaluate the phase change versus element dimensions (the S-curve);

2. **Feed antenna design, characterization and positioning**: a proper feed antenna must be chosen or designed (if not available with the desired specifications) using appropriate design approaches in order to build the whole reflectarray structure with the desired feed location;

3. **Required Phase Distribution evaluation**: in parallel with point 1, it is also possible to evaluate the required phase distribution of the reflectarray antenna that provides the wanted radiation characteristics (radiation pattern, directivity, gain) with the given constraints (feed position, reflected beam shape and direction, etc);

4. **Map of the Phase Distribution vs the physical Unit Cell parameter(s) using the obtained S-curve**: using the S-curve obtained in point 1, it is possible to correlate the required phase for each element (obtained in point 3) with the unit cell patch dimensions, to get the *patch size distribution* (the *mask*) that will be printed on the antenna substrate (refer to Appendix B for details);

5. **Entire Reflectarray layout analysis and full-wave simulation**: at this point the complete antenna is designed; it is the time to analyze its radiation characteristics by simulating it with full-wave technique;

6. **RA manufacturing and measurements**: using the *mask* obtained in point 4, it is possible to print the antenna on the chosen substrate, with proper geometry shape and ground plane. Measurements must be done and compared with theoretical simulation results, in order to validate the entire design.

Chapter 3

Design of innovative fractal unit cell

A new UC has been designed to improve the performance of the conventional square patch re-radiating element. The main goal is to obtain a phase curve (S-curve) covering a phase range of at least 360°, with a slope that is not too steep. In fact, a limited phase range (i.e. less than 360°) will provide high phase errors in the complete surface design; moreover, a very steep S-curve will lead to greater phase errors due to the tolerances of the manufacturing process. In literature there are a lot of proposed unit cell designs, which provide better performance with respect to the square patches in relation to the intended use. For example, some of them are designed to provide a wider bandwidth, while others are optimized to reduce mutual coupling between elements[47]. Also, controlling polarization, and maximizing the aperture efficiency while minimizing losses are challenging parameters in the unit cell design in addition to size and weight: for example, think about applications in mobile devices where miniaturization and low profile are often important design goals. Some UCs have been design with very complex shapes, as the one depicted in Figure 3.1.

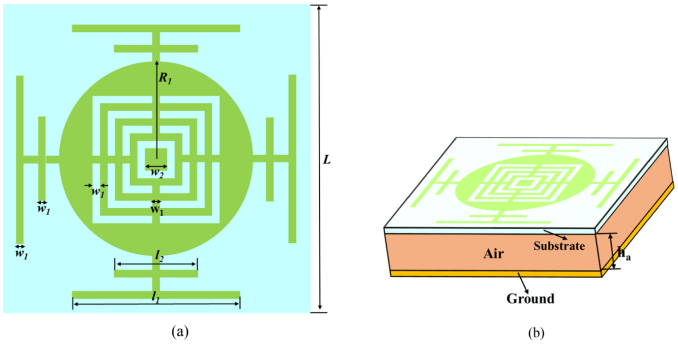

Figure 3.1: Complex unit cell. [48]

Others have rather simple design but are highly effective in achieving large phase ranges, as the *Double Ring Unit Cell*, depicted in Figure 3.2.

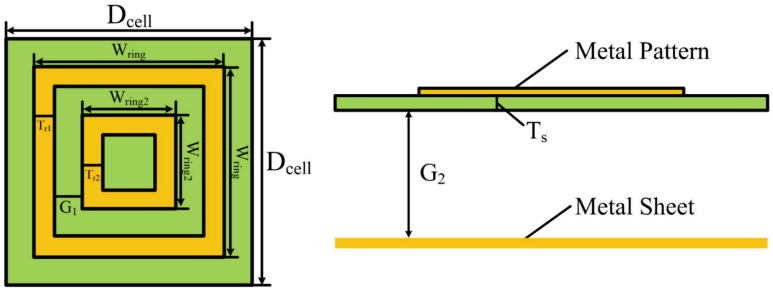

Figure 3.2: Double ring unit cell. [49]

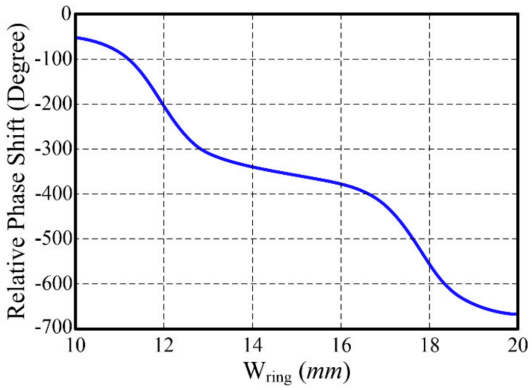

Figure 3.3: Phase range of the double ring unit cell. [49]

As can be seen from Figure 3.3, the achieved phase range of the Double Ring

configuration is very large, around 620°, which is wide enough to compensate the incident waves because only a phase shifting range of 360° is required to set any reflection angle. This is possible thanks to the dual-resonance structure of the two concentric square rings.

3.1 Innovative unit cell idea

The first idea was to design a unit cell with a patch shape similar to first-order fractal structure[50]. Searching in literature, one can find are other researches that have been carried out on this special shape. Specifically, the shape depicted in Figure 3.4 (in particular, the *Minkowski* fractal geometry) provided good results[50], printed on a Diclad870 substrate with standard thin thickness ($\varepsilon_r = 2.33$ and $h = 0.762$ mm) at the frequency $f_0 = 10$ GHz. The cell size is initially set to a value of $0.6\lambda \times 0.6\lambda$ at the design frequency and is considered to be generated from a $L = 7.86$ mm square patch length with scaling factor S from 0 up to 0.25.

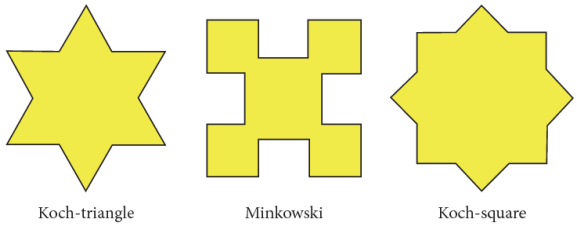

Figure 3.4: First-order fractal patch shape. [51]

The obtained results (i.e. the phase range versus the scaling factor S) are shown in Figure 3.5, both simulated and measured ones for 0.6λ cell size with $L = 7.86$ and for 0.3λ cell size with $L = 7.6$ mm.

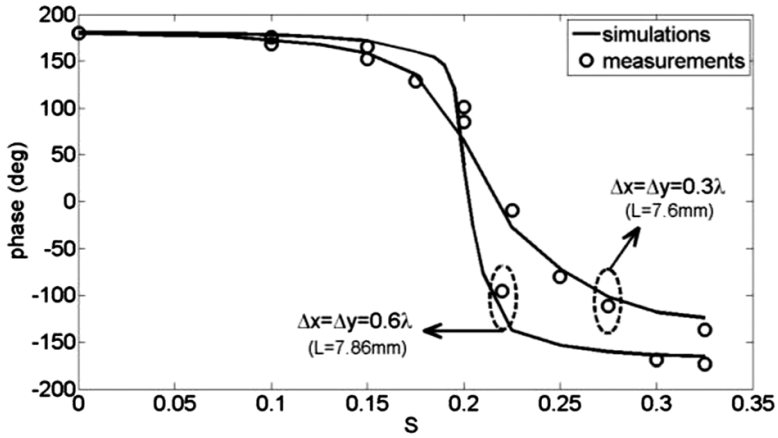

Figure 3.5: Results of the fractal patch shape. [50]

The achieved phase range of the 0.6λ unit cell is around 350° (instead of 330°) with a slightly smaller bandwidth (1% with respect to 1.8%) with respect to square patches. The second case (0.3λ cell size), instead, has a smaller phase range (320°) but a larger bandwidth (3.6%)[50].

3.2 Fractal unit cell definition

Based on the previously mentioned results, some attempts have been carried out in order to further improve the UC performance. The working frequency is considered to be $f_0 = 30$ GHz.

Since many attempts have been done, phases and magnitude plots may show some sharp behavior due to the low amount of points taken in the simulation. This is fine because, after finding a suitable unit cell, a more precise and accurate analysis will be performed.

3.2.1 Variation of W_{in}

The first designed unit cell has the following parameters (referring to Figure 3.6):

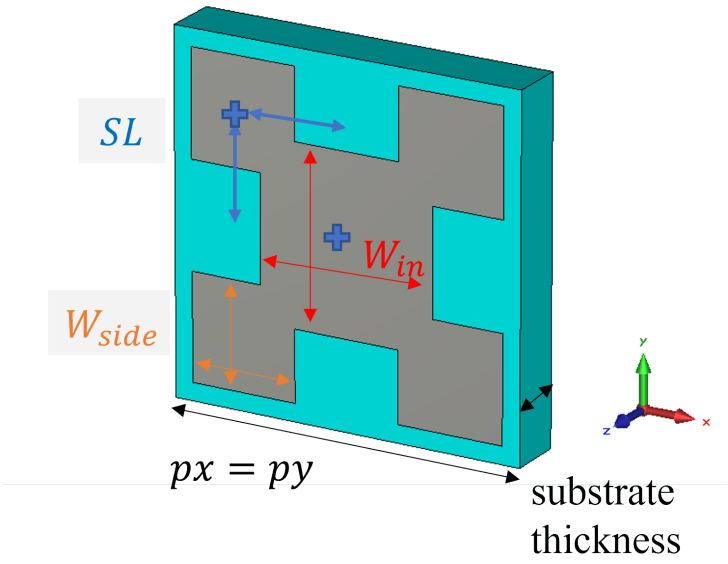

Figure 3.6: First designed fractal unit cell.

Substrate:

- material: Diclad527, with $\varepsilon_r = 2.55$, $\tan\delta = 0.0022$
- thickness: 0.8 mm
- cell size: $px = py = \frac{\lambda}{2} = 5$ mm (horizontal and vertical dimensions)

Metal patch:

- $W_{in} = [1.6,4.4]$ mm (central square side, variable)
- $W_{side} = 1.5$ mm (side squares size)
- $SL = 1.5$ mm (side squares center position)
- thickness: 0 mm (PEC)

The unit cell analysis has been carried out by varying W_{in} from 1.6 to 4.4 mm, as shown in Figure 3.7.

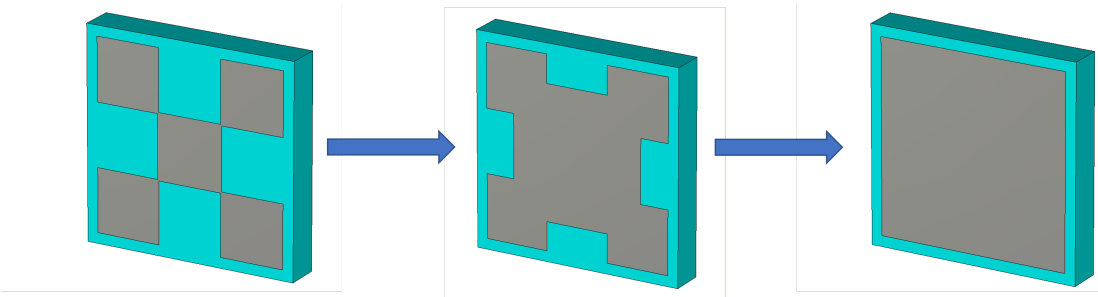

Figure 3.7: First designed fractal unit cell, varying dimensions.

The unit cell has been simulated with the *CST Microwave Studio* software in order to evaluate the phase range and the relative magnitude variation. The results are shown in Figure 3.8.

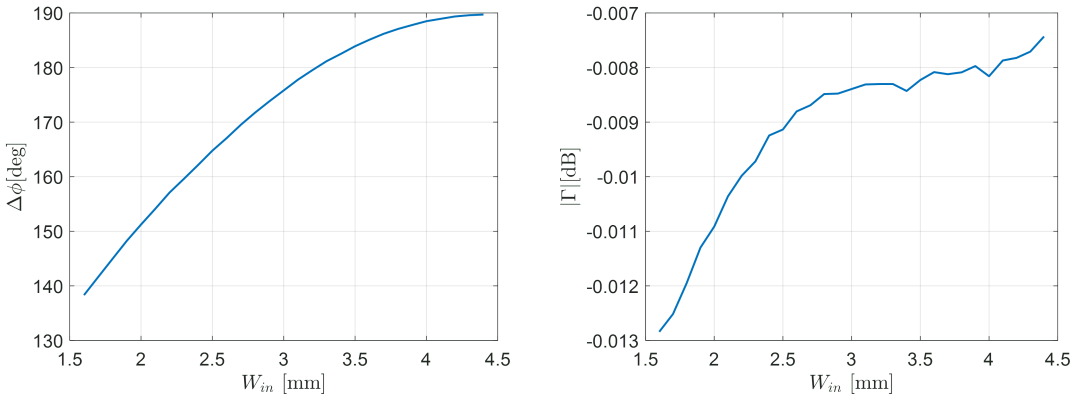

Figure 3.8: Phase and magnitude variation of the first designed fractal unit cell.

It is possible to see that phase range is very limited ($\approx 50°$); the magnitude plot does not show high resonances which is deemed satisfactory.

3.2.2 Variation of W_{side}

Using the same parameters of the unit cell in Figure 3.6, now W_{side} has been considered as the variable parameter, instead of W_{in} as in the previous case.

The unit cell analysis has been carried out by varying W_{side} from 0.6 to 1.5 mm, fixing $W_{in} = 2.5$ mm, as shown in Figure 3.9.

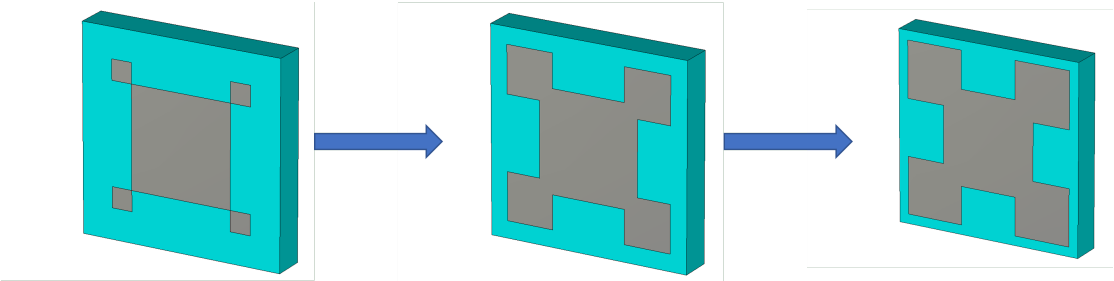

Figure 3.9: Second designed fractal unit cell, varying dimensions.

The unit cell has been simulated with the *CST Microwave Studio* software in order to evaluate the phase range and the relative magnitude variation. The results are shown in Figure 3.10.

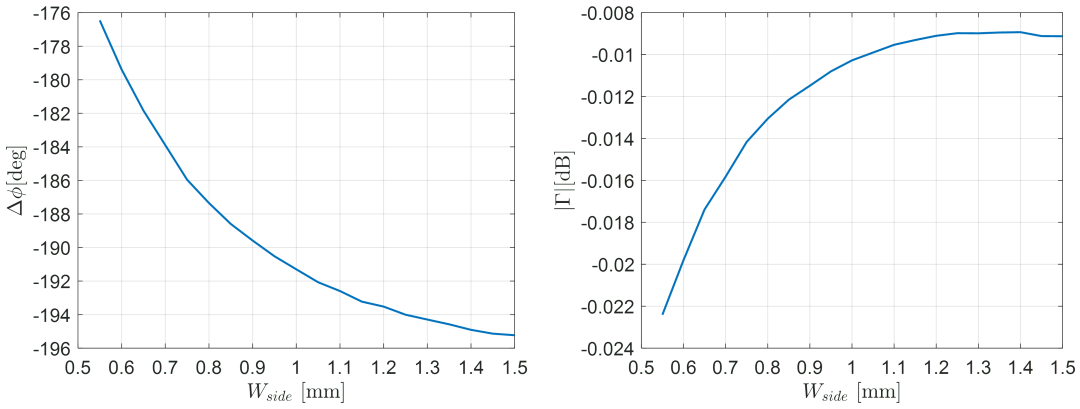

Figure 3.10: Phase and magnitude variation of the second designed fractal unit cell.

It is possible to see that phase range is even worse ($\approx 20°$) with respect to the previous case; again, the magnitude plot does not show high resonances which is suitable.

3.2.3 Variation of W_{in} and SL with respect to W_{side}

With reference to Figure 3.6, the third configuration has been designed by varying SL and W_{in} with respect to W_{side}. The chosen parameters are:

- W_{side} = [0.5,1.4] (variable)

- $W_{in} = 1.67 \cdot W_{side}$
- $SL = W_{side}$

The unit cell analysis has been carried out by varying W_{side} from 0.5 to 1.4 mm, as shown in Figure 3.11.

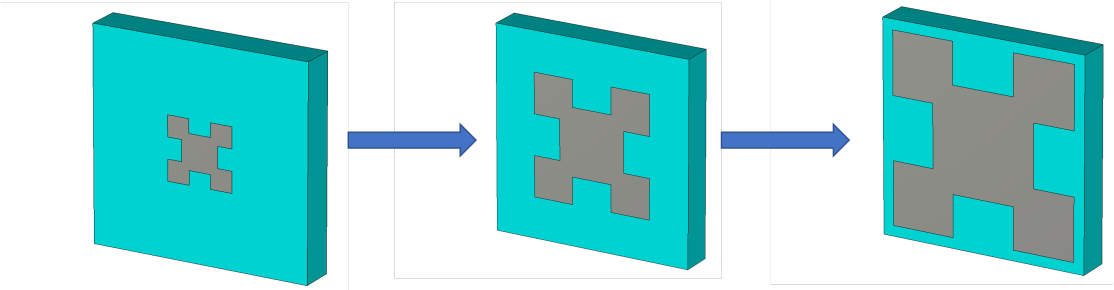

Figure 3.11: Third designed fractal unit cell, varying dimensions.

The unit cell has been simulated with the *CST Microwave Studio* software in order to evaluate the phase range and the relative magnitude variation. The results are shown in Figure 3.12.

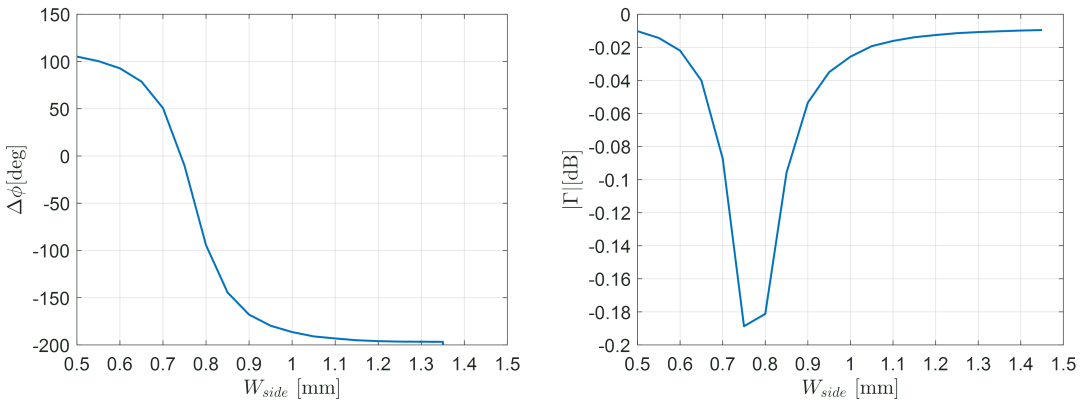

Figure 3.12: Phase and magnitude variation of the third designed fractal unit cell.

It is possible to see that phase range is very large ($\approx 300°$) with respect to the other attempts; the magnitude plot shows a resonance with a minimum peak of around -0.2 dB that is surely acceptable. In this case, it is possible to see that,

since each dimension of the patch is varied proportionally with respect to the other ones, very good results are achieved. The following results are provided going in this direction for the parameter choice, in order to reach at least 360° of phase variation.

3.2.4 Use of a central inset

With reference to Figure 3.6, the fourth configuration has been designed starting from the third one, with:

- $W_{side} = [0.5,1.4]$ (variable)
- $W_{in} = 1.67 \cdot W_{side}$
- $SL = W_{side}$

making hollow the central square, adding a new parameter:

- $In_W = 0.25 \cdot W_{side}$

which is the thickness of the central ring, as in Figure 3.13.

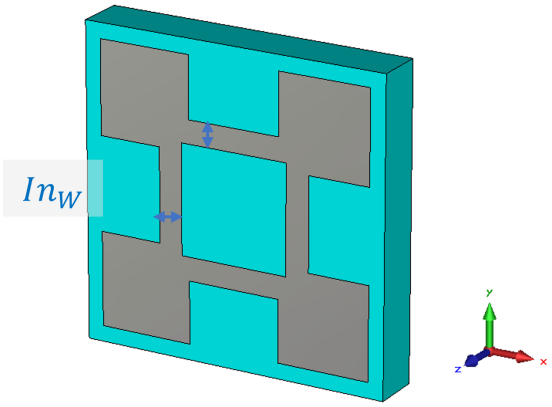

Figure 3.13: Fourth designed fractal unit cell, highlighting the new In_W parameter.

The unit cell analysis has been carried out by varying W_{side} from 0.5 to 1.4 mm, as shown in Figure 3.14.

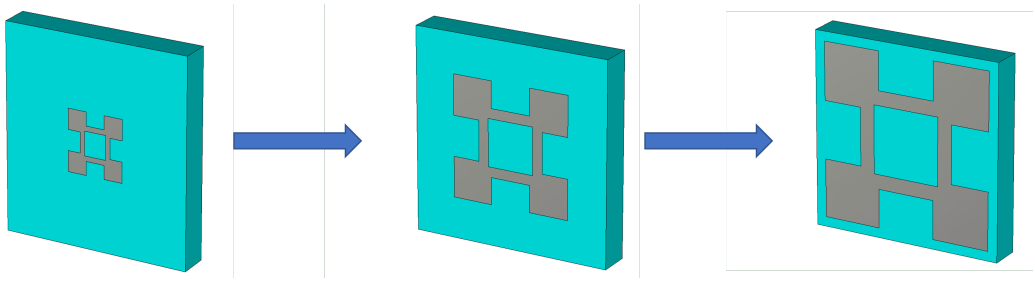

Figure 3.14: Fourth designed fractal unit cell, varying dimensions.

The unit cell has been simulated with the *CST Microwave Studio* software in order to evaluate the phase range and the relative magnitude variation. The results are shown in Figure 3.15.

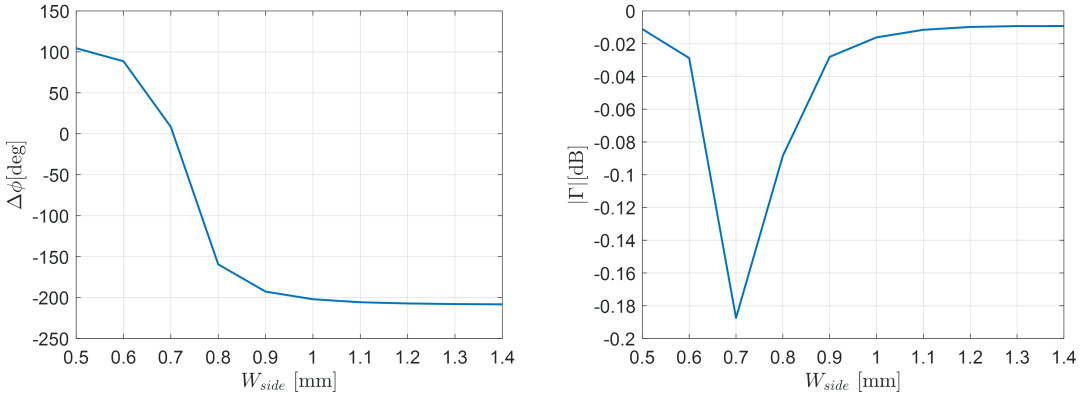

Figure 3.15: Phase and magnitude variation of the fourth designed fractal unit cell.

It is possible to see that phase range is still rather large ($\approx 300°$) with respect to the third configuration; the magnitude plot is similar to the one of the third configuration too. It is possible to see that no important improvements are provided using this new configuration.

3.2.5 Use of side insets

With reference to Figure 3.6, the fifth configuration has been designed starting from the third one, with:

- W_{side} = [0.5,1.4] (variable)

- $W_{in} = 1.67 \cdot W_{side}$
- $SL = W_{side}$

making hollow the side squares, adding a new parameter:

- $In_{side} = 0.133 \cdot W_{side}$

which is the thickness of the side rings, as in Figure 3.16.

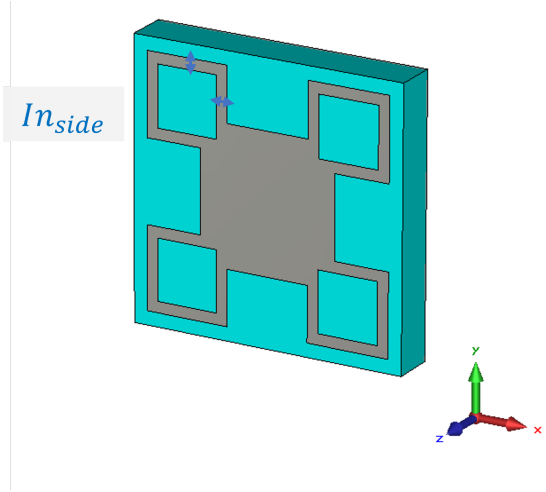

Figure 3.16: Fifth designed fractal unit cell, highlighting the new In_{side} parameter.

The unit cell analysis has been carried out by varying W_{side} from 0.5 to 1.4 mm, as shown in Figure 3.17.

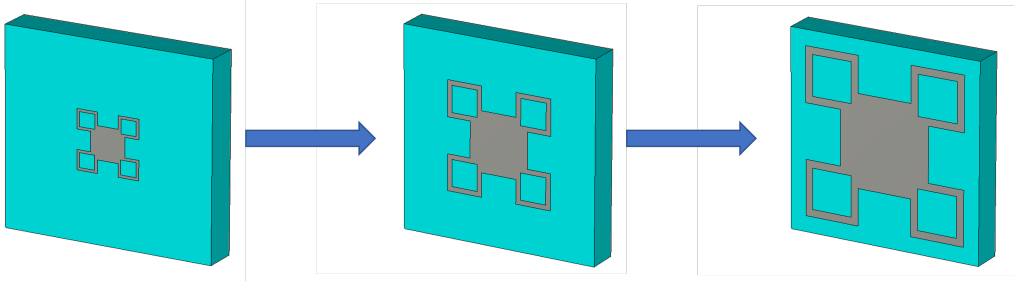

Figure 3.17: Fifth designed fractal unit cell, varying dimensions.

The unit cell has been simulated with the *CST Microwave Studio* software in order to evaluate the phase range and the relative magnitude variation. The results are shown in Figure 3.18.

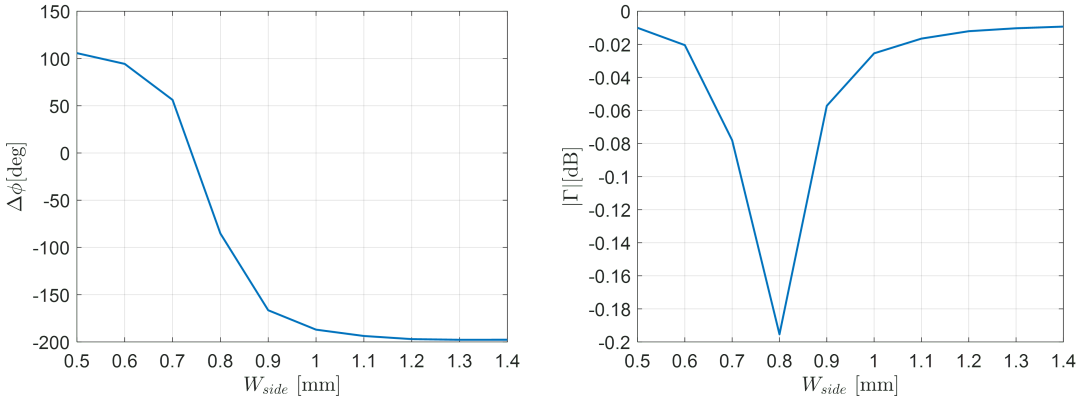

Figure 3.18: Phase and magnitude variation of the fifth designed fractal unit cell.

In this case, the phase range is still rather large ($\approx 300°$), similarly to the third configuration; the same applies also for the magnitude plot. As in the fourth configuration, no significant enhancements are achieved using this new configuration of the unit cell.

3.2.6 Use of central double rings

Using the parameters depicted in Figure 3.6, the sixth configuration has been designed starting from the fourth one (Figure 3.13), with:

- $W_{side} = [0.5,1.4]$ (variable)
- $W_{in} = 1.67 \cdot W_{side}$
- $SL = W_{side}$
- $In_W = 0.25 \cdot W_{side}$

making a double ring in the central position, adding two new parameters:

- $In_{space} = 0.15 \cdot W_{side}$
- $In_h = 0.15 \cdot W_{side}$

which are the spacing between the two rings and the thickness of the inner ring, respectively, as in Figure 3.19.

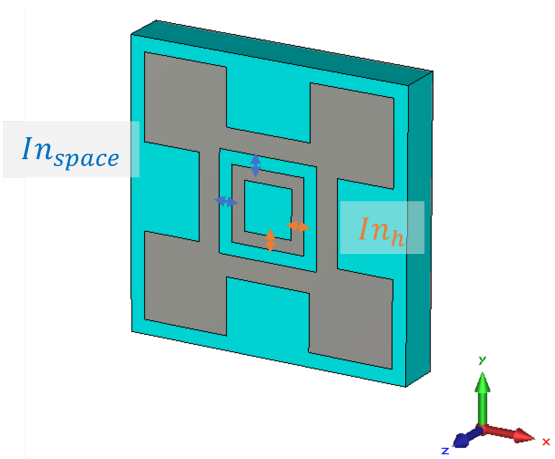

Figure 3.19: Sixth designed fractal unit cell, highlighting the new In_{space} and In_h parameters.

The unit cell analysis has been carried out by varying W_{side} from 0.5 to 1.4 mm, as shown in Figure 3.20.

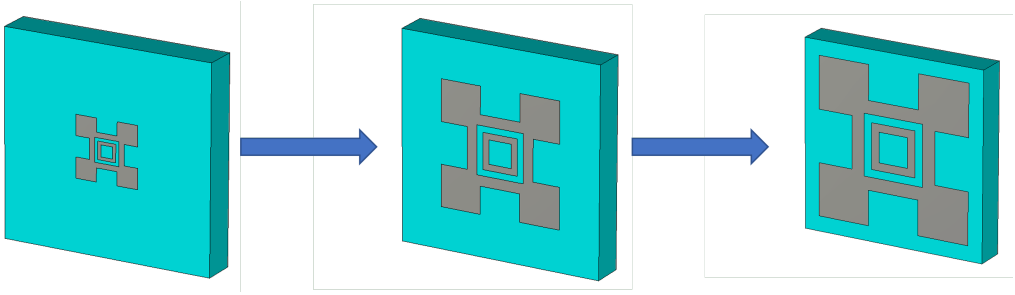

Figure 3.20: Sixth designed fractal unit cell, varying dimensions.

The unit cell has been simulated with the *CST Microwave Studio* software in order to evaluate the phase range and the relative magnitude variation. The results are shown in Figure 3.21.

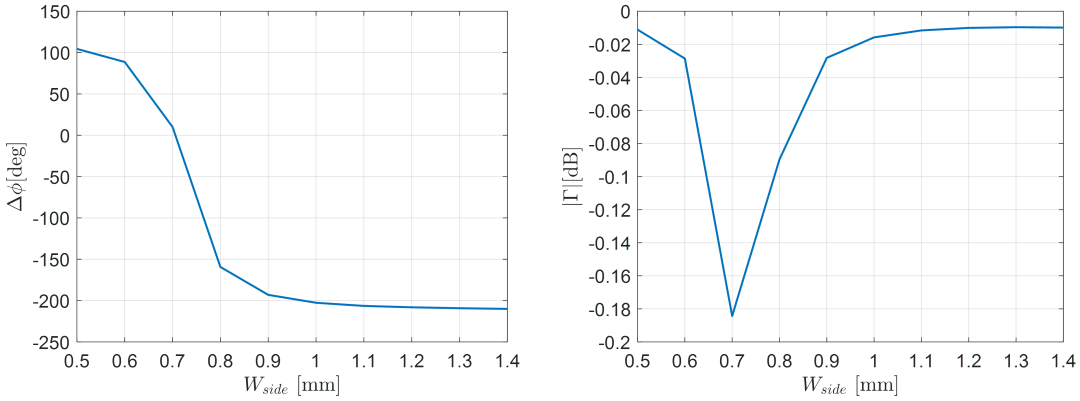

Figure 3.21: Phase and magnitude variation of the sixth designed fractal unit cell.

Once again, it is possible to see that no major improvements are gained with this new configuration with respect to the third one, and of course, with respect to the fourth and fifth ones too. The effort to create a more complex structure with more degrees of freedom did not lead to further significant improvements.

3.2.7 Increase of the central double rings

Using the parameters depicted in Figure 3.6, the seventh configuration has been designed starting from the sixth one (Figure 3.19), with:

- $W_{side} = [0.5,1.4]$ (variable)
- $W_{in} = 2.5 \cdot W_{side}$
- $SL = W_{side}$
- $In_W = 0.25 \cdot W_{side}$
- $In_{space} = 0.15 \cdot W_{side}$
- $In_h = 0.25 \cdot W_{side}$

making a larger double ring in the central position, in fact W_{in} and In_h have been increased with respect to the sixth case, as in Figure 3.22.

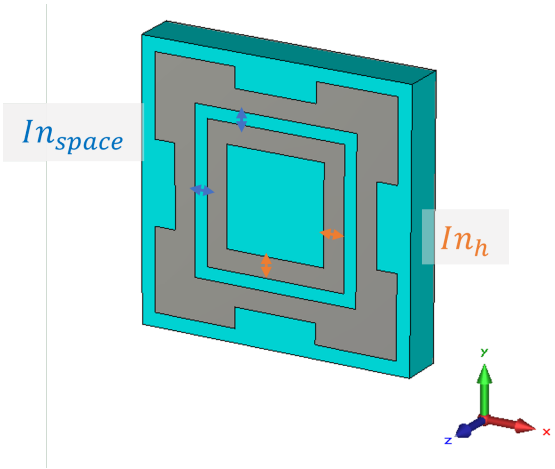

Figure 3.22: Seventh designed fractal unit cell.

The unit cell analysis has been carried out by varying W_{side} from 0.5 to 1.4 mm, as shown in Figure 3.23.

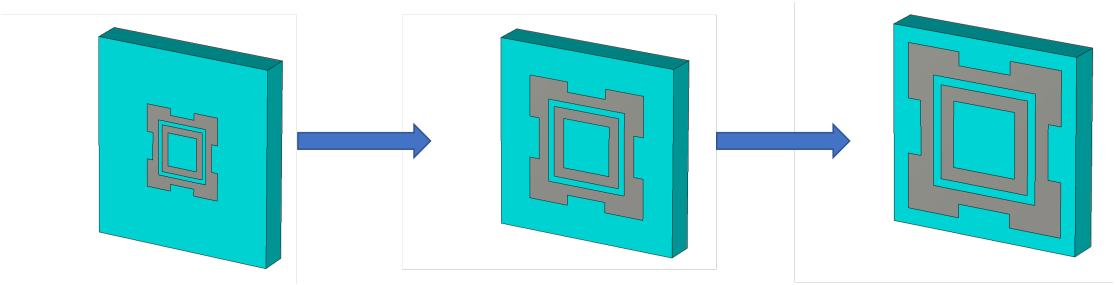

Figure 3.23: Seventh designed fractal unit cell, varying dimensions.

The unit cell has been simulated with the *CST Microwave Studio* software in order to evaluate the phase range and the relative magnitude variation. The results are shown in Figure 3.24.

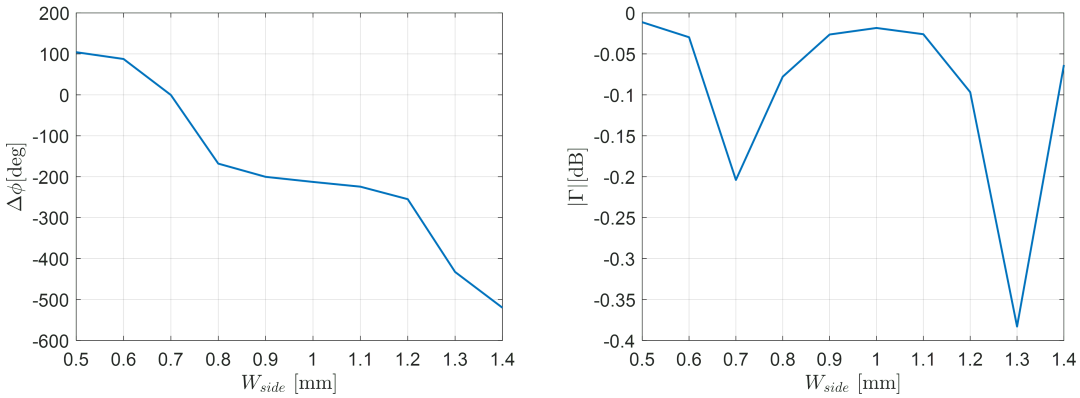

Figure 3.24: Phase and magnitude variation of the seventh designed fractal unit cell.

The situation now is much different from the previous cases: as can be seen from the magnitude plot, this structure has a double-resonant capability and the total phase range that is achieved is around 600°, meaning a great improvement. This unit cell will be recalled later for further use.

3.2.8 Use of side insets with fixed size

Using the parameters depicted in Figure 3.6, the eighth configuration has been designed starting from the fifth one (Figure 3.16), with:

- $W_{side} = 1.5$ mm
- $W_{in} = [2,3.9]$ mm (variable)
- $SL = W_{side}$
- $In_{side} = 0.133 \cdot W_{side}$

making a larger central square with fixed hollow side patches, with variable W_{in} and fixed W_{side} dimensions.

The unit cell analysis has been carried out by varying W_{in} from 2 to 3.9 mm, with fixed $W_{side} = 1.5$ mm, as shown in Figure 3.25.

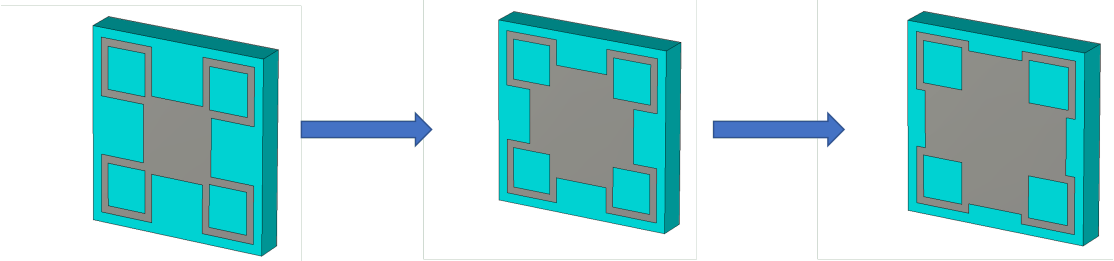

Figure 3.25: Eight designed fractal unit cell, varying dimensions.

The unit cell has been simulated with the *CST Microwave Studio* software in order to evaluate the phase range and the relative magnitude variation. The results are shown in Figure 3.26.

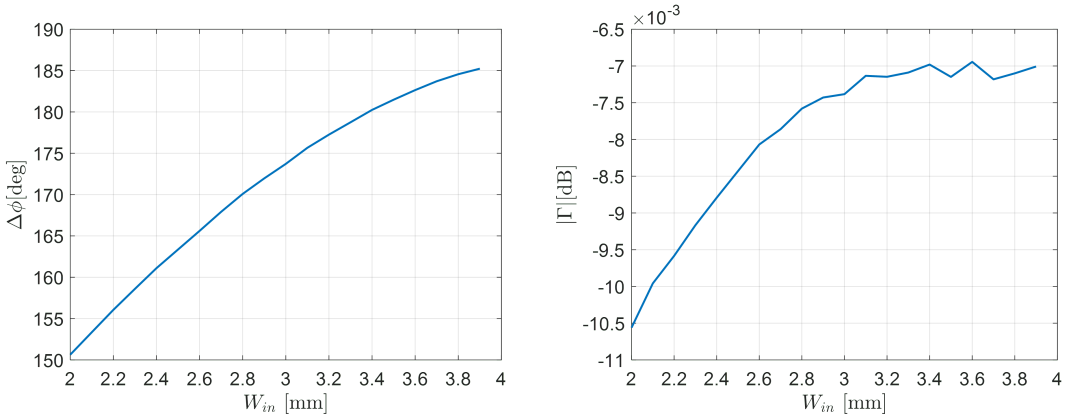

Figure 3.26: Phase and magnitude variation of the eighth designed fractal unit cell.

By looking at the results, one can see that the phase range is very limited ($\approx 35°$); the magnitude plot does not show high resonances, which is acceptable. Thus, this configuration does not provide any improvement.

3.2.9 Use of side insets with fixed size with central double ring

With reference to Figure 3.6, the ninth configuration has been designed starting from the eighth one (starting from the shape depicted in Figure 3.16), with:

- $W_{side} = 1.5$ mm
- $W_{in} = [1.5,4]$ mm (variable)
- $SL = W_{side}$
- $In_{side} = 0.133 \cdot W_{side}$
- $In_W = 0.1 \cdot W_{in}$
- $In_{space} = 0.1 \cdot W_{in}$
- $In_h = 0.1 \cdot W_{in}$

making a larger central double ring with fixed hollow side patches, with variable W_{in} and fixed W_{side} dimensions, as in Figure 3.27.

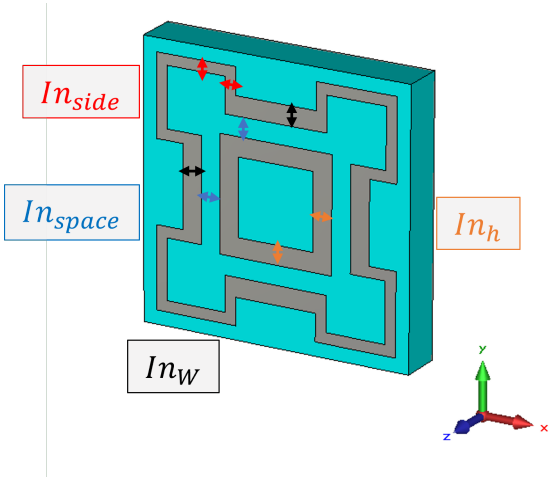

Figure 3.27: Ninth designed fractal unit cell.

The unit cell analysis has been carried out by varying W_{in} from 1.5 to 4 mm, with fixed $W_{side} = 1.5$ mm, as shown in Figure 3.28.

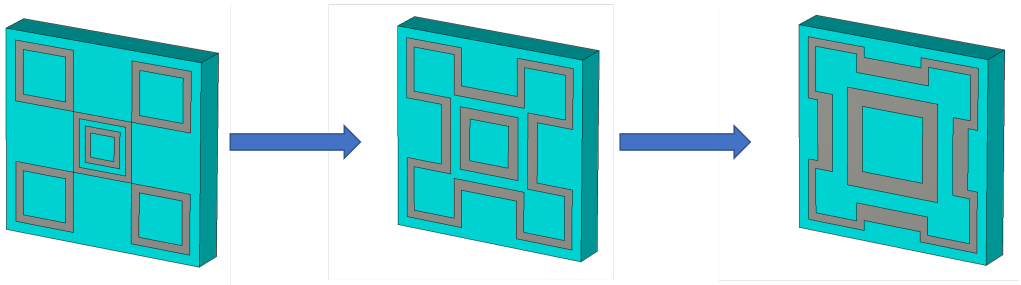

Figure 3.28: Ninth designed fractal unit cell, varying dimensions.

The unit cell has been simulated with the *CST Microwave Studio* software in order to evaluate the phase range and the relative magnitude variation. The results are shown in Figure 3.29.

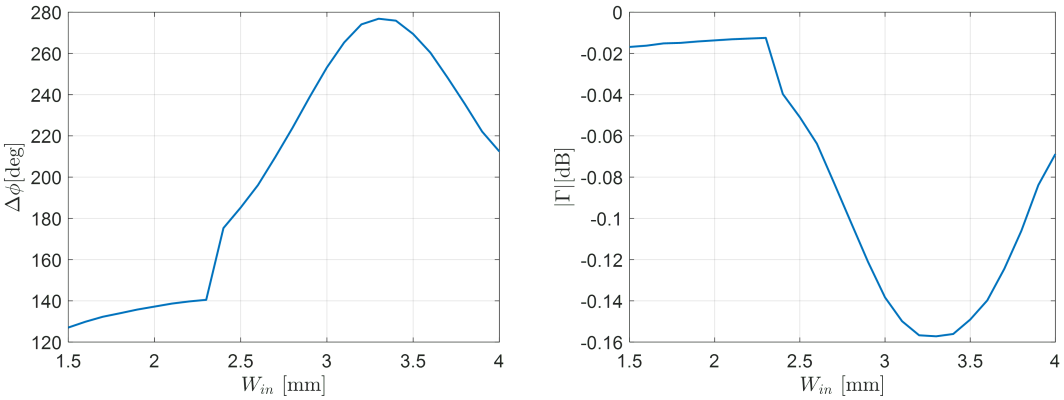

Figure 3.29: Phase and magnitude variation of the ninth designed fractal unit cell.

It is possible to see that phase range is limited ($\approx 150°$) also with a non smooth phase variation; the magnitude plot does not show high resonances which is appropriate. This configuration cannot be used for the intended purpose.

3.2.10 Use of a central square

With reference to Figure 3.19, the following configuration has been designed starting from the sixth one, with:

- $W_{side} = [0.5,1.5]$ mm (variable)

- $W_{in} = 2.5 \cdot W_{side}$
- $SL = W_{side}$
- $In_W = 0.25 \cdot W_{side}$
- $In_{space} = 0.15 \cdot W_{side}$

making a central filled square patch (instead of an hollow one), as in Figure 3.30.

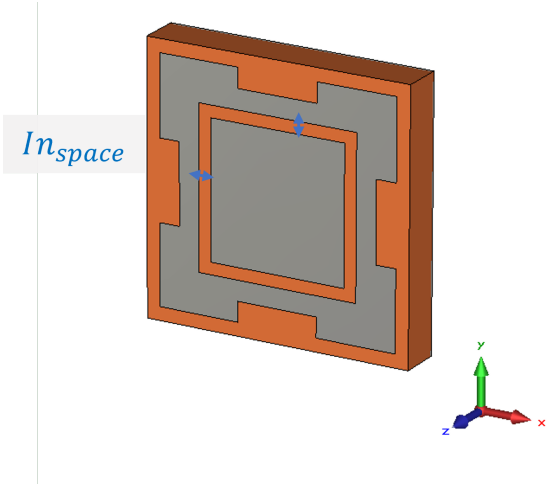

Figure 3.30: Tenth designed fractal unit cell.

The unit cell analysis has been carried out by varying W_{side} from 0.5 to 1.5 mm, as shown in Figure 3.31.

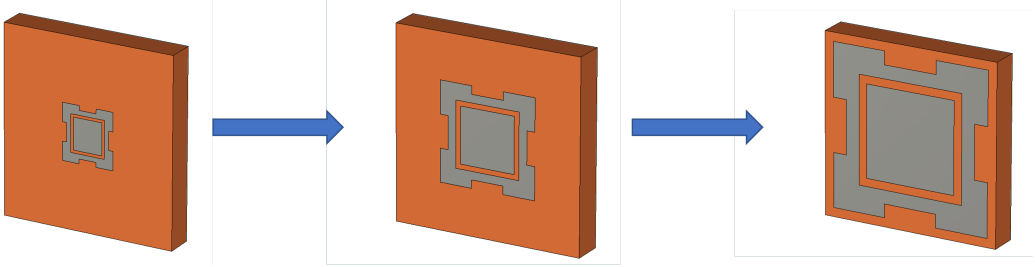

Figure 3.31: Tenth designed fractal unit cell, varying dimensions.

The unit cell has been simulated with the *CST Microwave Studio* software in order to evaluate the phase range and the relative magnitude variation. The results are shown in Figure 3.32.

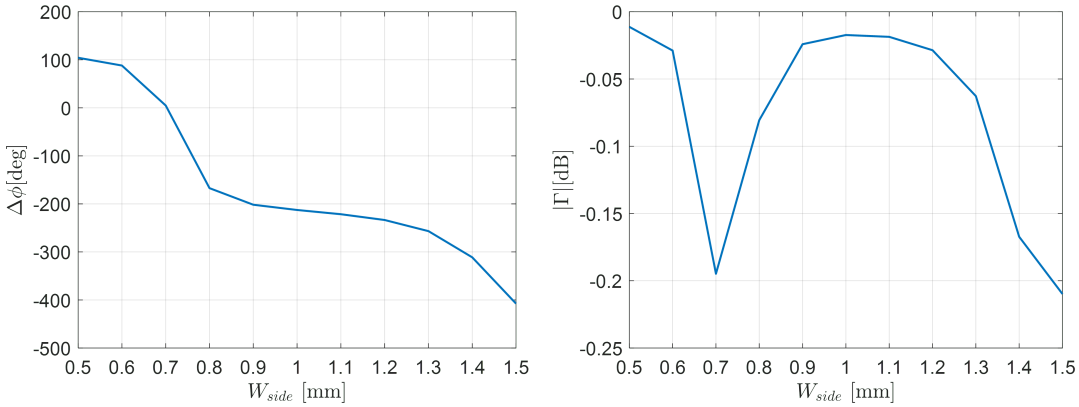

Figure 3.32: Phase and magnitude variation of the tenth designed fractal unit cell.

It is possible to see that phase range is still rather good ($\approx 500°$) with respect to the sixth case; the magnitude plot does not show high resonances (around 0.2 dB) which is fine. This configuration in simpler with respect to the sixth one since does not have a central ring but a filled square, leading to an higher simplicity in the design and manufacturing processes. This configuration will be further improved in order to get the target unit cell.

3.2.11 Increase of the spacing

With reference to Figure 3.30, the following (eleventh) configuration has been carried out starting from the tenth one, with:

- $W_{side} = [0.5,4]$ mm (variable)
- $W_{in} = 2.5 \cdot W_{side}$
- $SL = W_{side}$
- $In_W = 0.25 \cdot W_{side}$
- $In_{space} = 0.2 \cdot W_{side}$

where the only change is the increasing of the In_{space} parameter from $0.15 \cdot W_{side}$ to $0.2 \cdot W_{side}$, as in Figure 3.33.

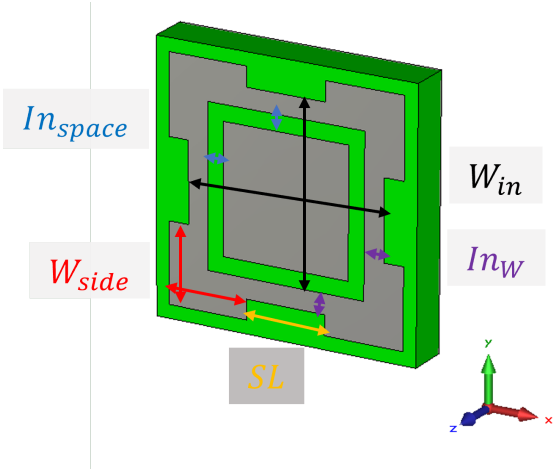

Figure 3.33: Eleventh designed fractal unit cell.

The unit cell analysis has been carried out by varying W_{side} from 0.5 to 1.5 mm, as shown in Figure 3.34.

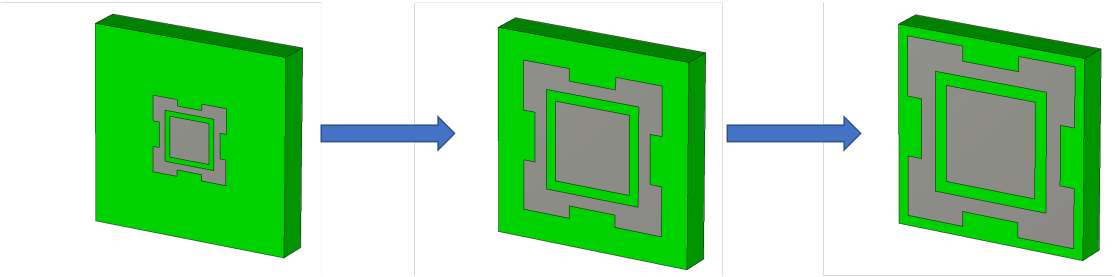

Figure 3.34: Eleventh designed fractal unit cell, varying dimensions.

The unit cell has been simulated with the *CST Microwave Studio* software in order to evaluate the phase range and the relative magnitude variation. The results are shown in Figure 3.35.

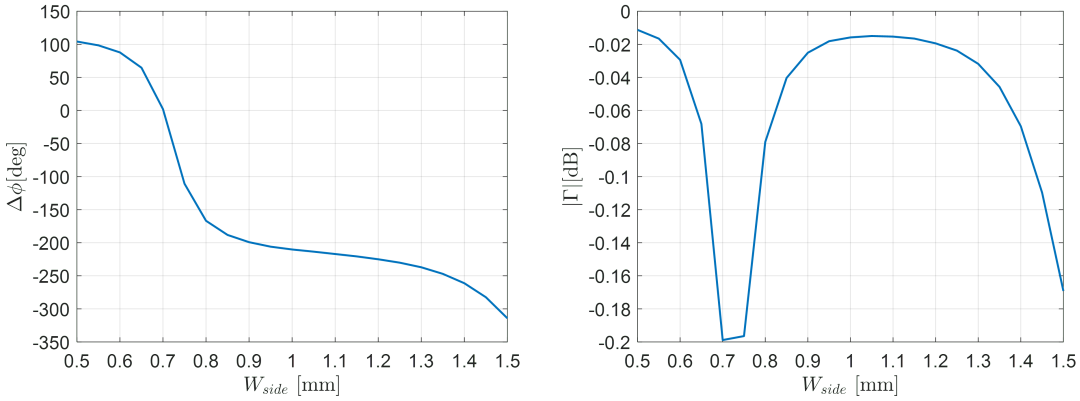

Figure 3.35: Phase and magnitude variation of the eleventh designed fractal unit cell.

It is possible to see that phase range is still rather good ($\approx 400°$) with respect to the tenth case; the magnitude plot does not show high resonances (around 0.2 dB) which is admissible. This configuration has been chosen due to manufacturing reasons: in the tenth one the spacing between the outer ring and the central patch was too small and difficult to be printed. This configuration has therefore an increase spacing to improve manufacturing processes.

A further improvement of the In_{space} parameter up to $0.25 \cdot W_{side}$ has been simulated but the achieved phase range was smaller with respect to the above-mentioned one (around 360°), as can be seen in Figure 3.36.

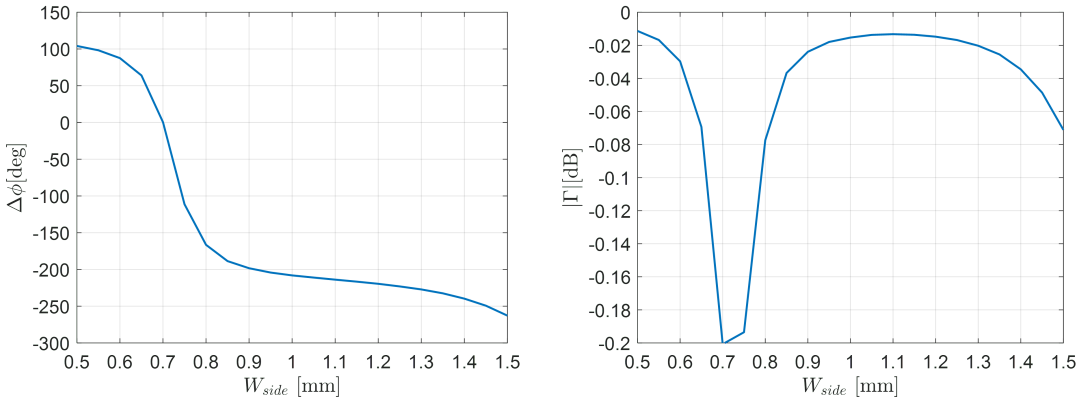

Figure 3.36: Phase and magnitude variation of the twelfth designed fractal unit cell, with larger spacing parameter $In_{space} = 0.25 \cdot W_{side}$.

To further improve this eleventh configuration, an increased thickness substrate can be considered, in order to keep a large phase variation with the same unit cell shape. This final configuration is described in the following section.

3.3 Final unit cell configuration

With reference to Figure 3.37, the final configuration has been designed starting from the eleventh one, with:

Substrate:

- material: Diclad527, with $\varepsilon_r = 2.55$, $\tan\delta = 0.0022$
- thickness: 1.6 mm
- cell size: $px = py = \frac{\lambda}{2} = 5$ mm (horizontal and vertical dimensions)

Metal patch:

- $W_{side} = [0.5,1.5]$ mm (variable)
- $W_{in} = 2.5 \cdot W_{side}$
- $SL = W_{side}$
- $In_W = 0.25 \cdot W_{side}$
- $In_{space} = 0.2 \cdot W_{side}$
- thickness: 0 mm (PEC)

where the only change is the increase of the substrate thickness parameter from 0.8 mm to 1.6 mm, as in Figure 3.37.

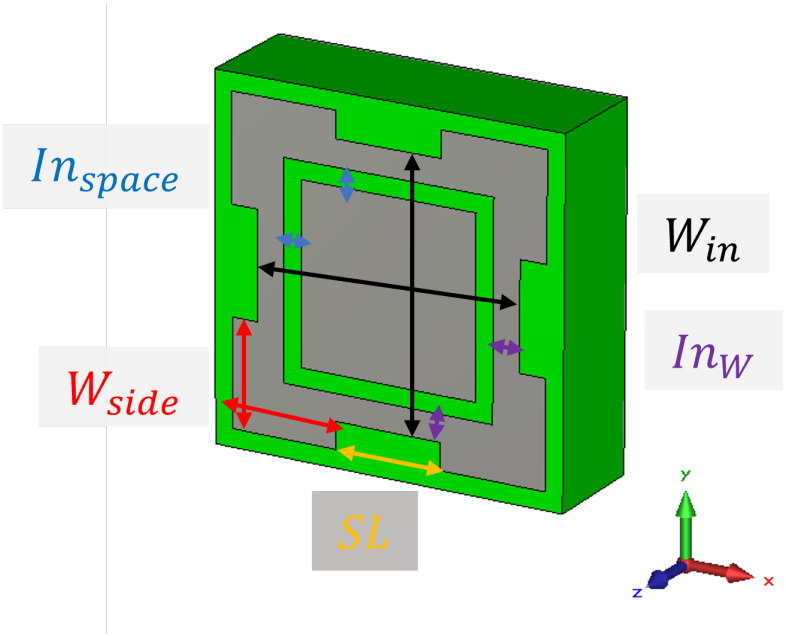

Figure 3.37: Final designed unit cell.

The unit cell analysis has been carried out by varying W_{side} from 0.5 to 1.5 mm, as shown in Figure 3.38.

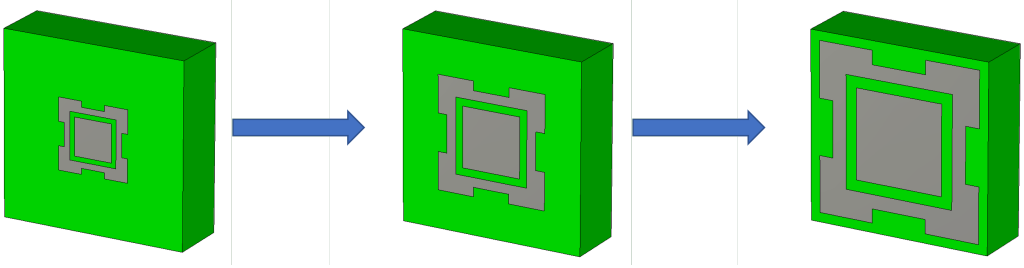

Figure 3.38: Final designed unit cell, varying dimensions.

The unit cell has been simulated with the *CST Microwave Studio* software in order to evaluate the phase range and the relative magnitude variation. The results are shown in Figures 3.39 and 3.40.

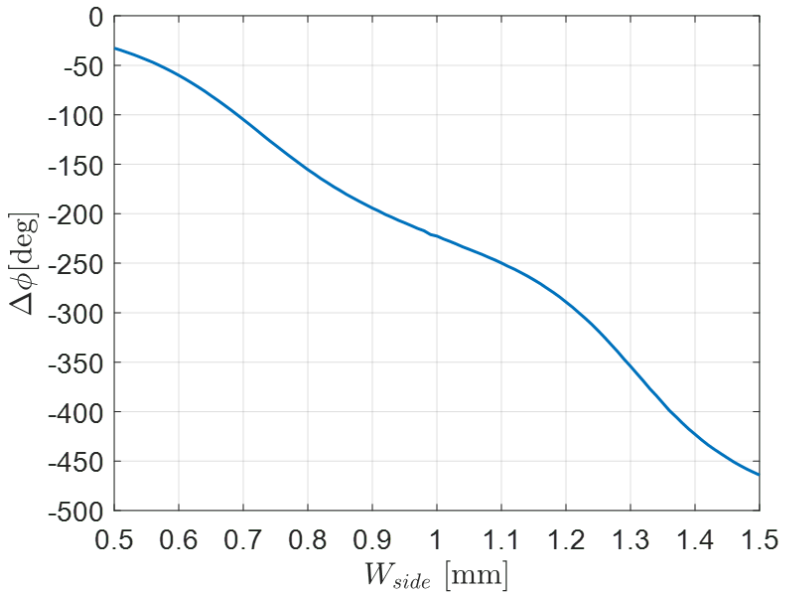

Figure 3.39: Results of the phase variation of the final designed unit cell.

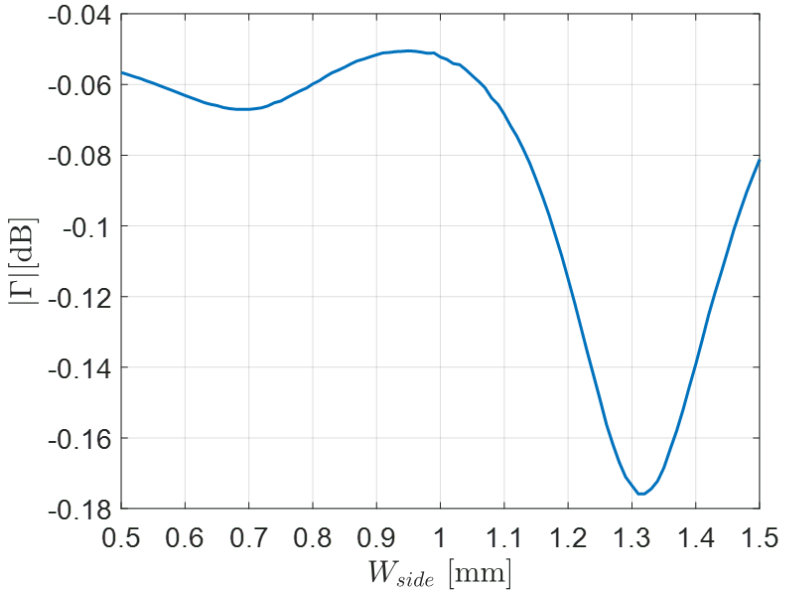

Figure 3.40: Results of the magnitude variation of the final designed unit cell.

It is possible to see that phase range is still satisfactory ($\approx 400°$); the magnitude

plot does not show high resonances (around 0.18 dB) which is admissible. This configuration has been analyzed with a smaller step size in the simulation process in order to better analyze its behavior. Also, other kinds of simulations have been done in order to fully characterize this final unit cell configuration for later use in a complete reflectarray configuration. For this purpose, a proper DXF file is then created using this new unit cell (see Appendix B.3).

3.3.1 Frequency behavior

In order to analyze the frequency bandwidth of the final version of the new unit cell, it is possible to simulate it using the *CST Microwave Studio* software in a certain frequency range. In this case the chosen frequencies are 29,30 and 31 GHz. In Figure 3.41 it is possible to observe the unit cell behavior with respect to the three frequencies: a smooth phase variation is obtained for the three curves and they are almost parallel one to each other. The frequency behavior is, in this case, almost linear, which leads to a good bandwidth of the new unit cell.

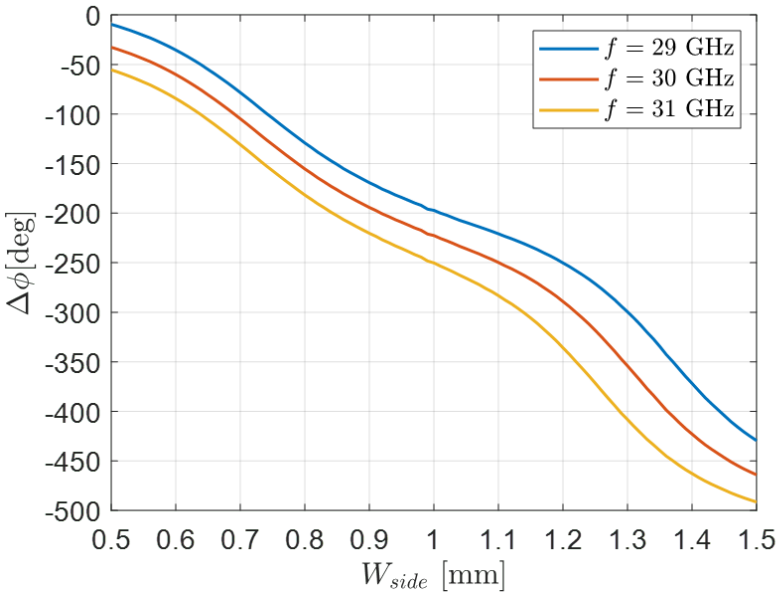

Figure 3.41: Results of the phase variation of the final designed unit cell at 29, 30 and 31 GHz.

Moreover, the magnitude can be analyzed in order to inspect whether important

resonance phenomena take place in the variation of the unit cell dimensions inside the mentioned bandwidth. The magnitude plot is shown in Figure 3.42.

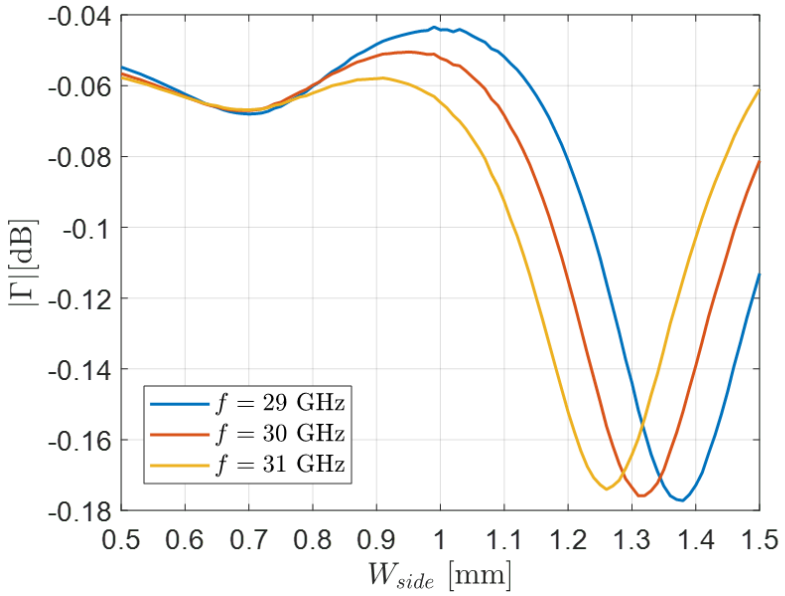

Figure 3.42: Results of the magnitude variation of the final designed unit cell at 29, 30 and 31 GHz.

From the magnitude plot, it is possible to see that no major resonance phenomena occur in the variation range of the unit cell parameters for all the three considered frequencies.

3.3.2 Angle of incidence dependency

Another important parameter that must be considered in the unit cell characterization is the *angle of incidence*: it is the angle formed by the impinging wave on the unit cell and its surface. The angle of incidence results of the unit cell are provided in Figures 3.43 and 3.44, where the phase and magnitude plots, at $f = 30$ GHz, are depicted, respectively.

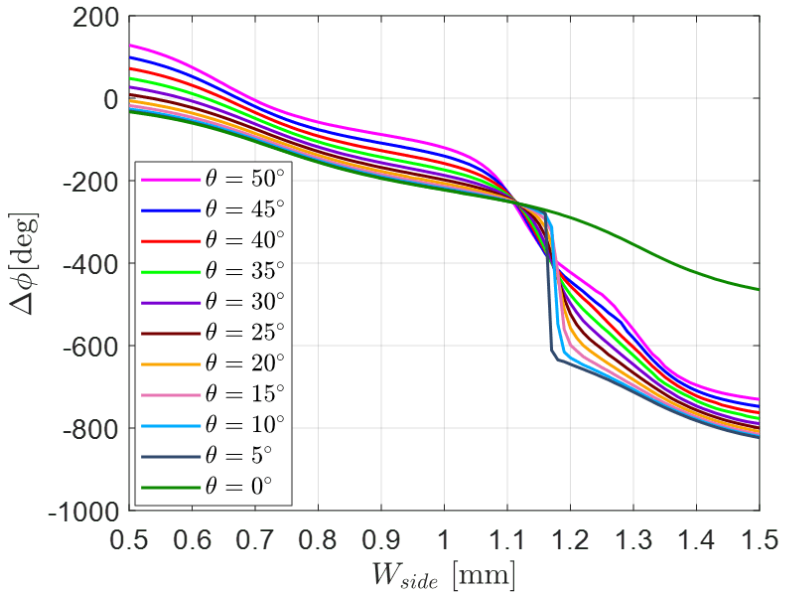

Figure 3.43: Results of the phase variation of the final designed unit cell for different angles of incidence, with $f = 30$ GHz.

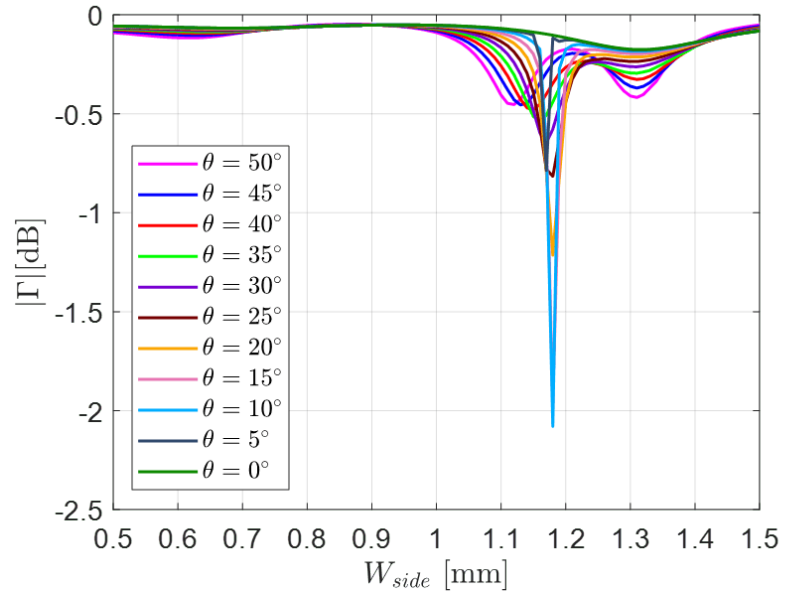

Figure 3.44: Results of the magnitude variation of the final designed unit cell for different angles of incidence, with $f = 30$ GHz.

As can be seen, there is a large unwanted step in the phase variation diagram: what can be done is to avoid the W_{side} variation range between 1.1 and 1.2 mm in order to eliminate it. Also, the entire phase diagram can be shifted in order to produce a more readable plot.

The new phase variation diagram, for different angles of incidence, is depicted in Figure 3.45, while the magnitude plot is now omitted, since the absence of large resonances has been already verified beforehand.

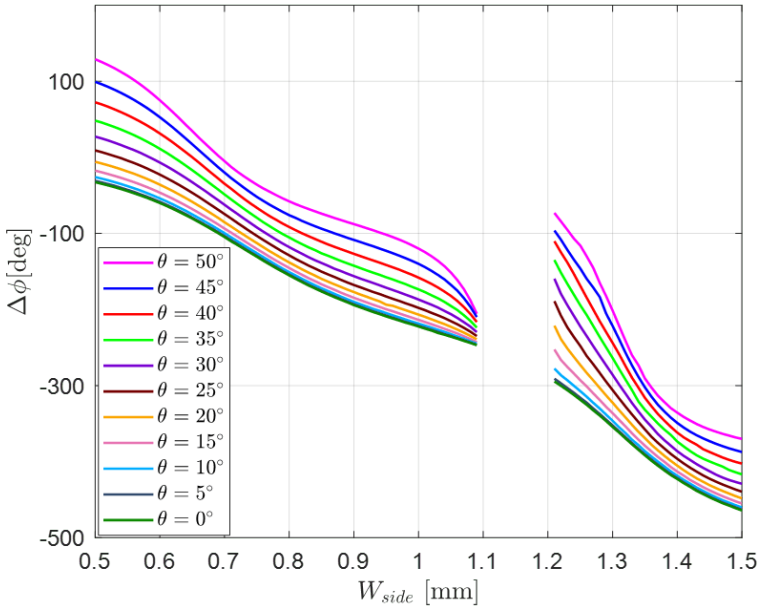

Figure 3.45: Phase variation of the final unit cell for different angles of incidence, with restricted range of dimensions, with $f = 30$ GHz.

This analysis has been done also for angles of incidence in the range [55°,85°], but such high angles hardly ever been used and therefore, after verifying that there were no important resonances, the plots are here omitted.

The same analysis done at $f = 30$ GHz, has also been carried out at $f = 31$ GHz, in order to check whether major resonances occur at the upper frequency in the considered range. The angle of incidence results of the unit cell at $f = 31$ GHz are provided in Figures 3.46 and 3.47, where the phase and magnitude plots, at $f = 31$ GHz, are depicted, respectively.

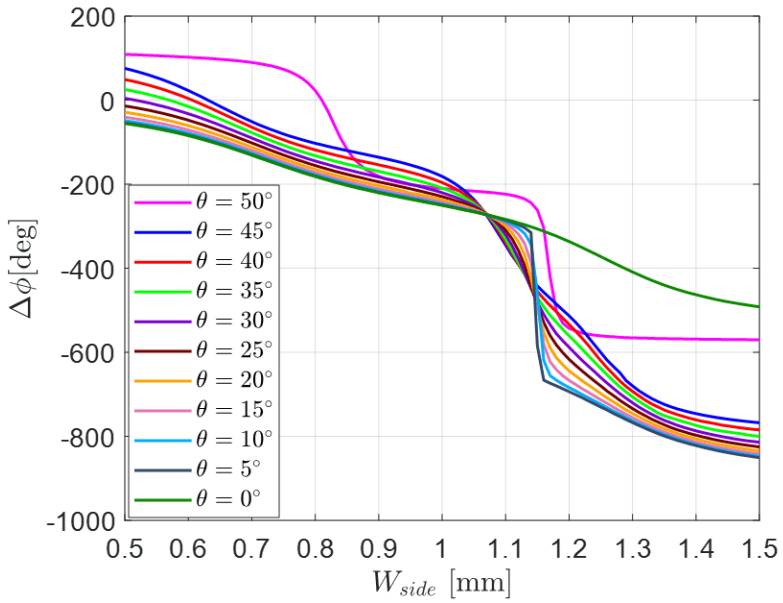

Figure 3.46: Results of the phase variation of the final designed unit cell for different angles of incidence, with $f = 31$ GHz.

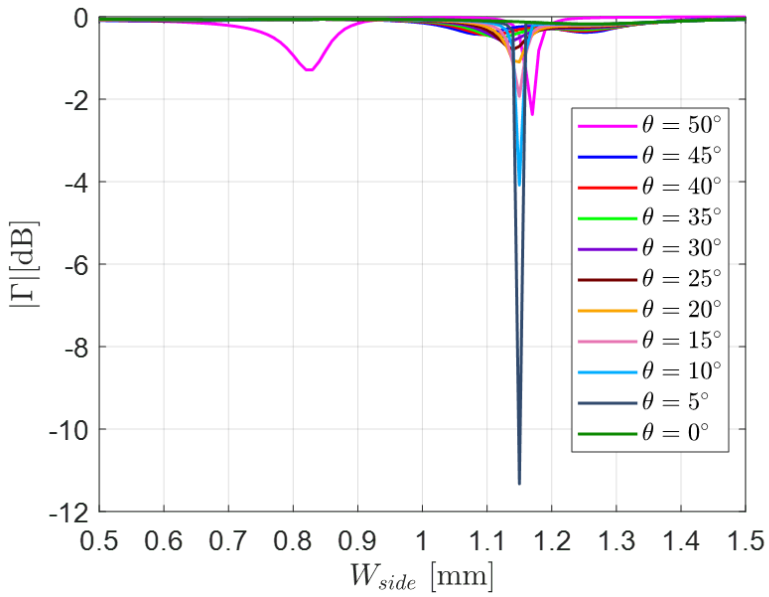

Figure 3.47: Results of the magnitude variation of the final designed unit cell for different angles of incidence, with $f = 31$ GHz.

From the Figures it is possible to see an important resonance that occurs for values of W_{side} between 1.1 and 1.2 mm: this is not a problem since this range has been already removed as a result of the 30 GHz analysis. Since there are no other important resonances, we can conclude that there are no additional ranges of the parameter variation that need to be removed.

Also in this case, the range of angles between 55° and 85° is omitted since it's not of primary importance for the scope of this work and, moreover, no major resonances occur in this range.

3.3.3 Design of RA using innovative unit cell

To validate the design of the innovative unit cell, a comparison with the square patch unit cell is carried out for a 24×24 RA antenna, using a feed horn.

3.3.3.1 Feed horn

The employed feed horn design procedure is explained in details in [52]. The idea was to design an ad-hoc feed to optimize the entire antenna system performance of a CRA according to some design specifications, working in the frequency band $29 - 31$ GHz. The aim of the optimization process was to determine the radius of the aperture, the number of modes and the set of weights of the modes on the circular aperture, that allow to maximize the CRA gain and to minimize its cross-pol and SLL. Also, easy realization and low sensitivity to manufacturing tolerances were design requirements.

The feed horn used in all the designs is depicted in Figure 3.48 and its radiation characteristics are shown in Figure 3.49.

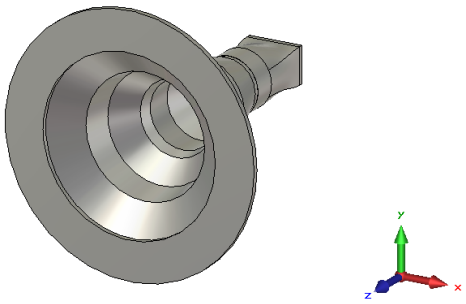

Figure 3.48: Employed feed horn.

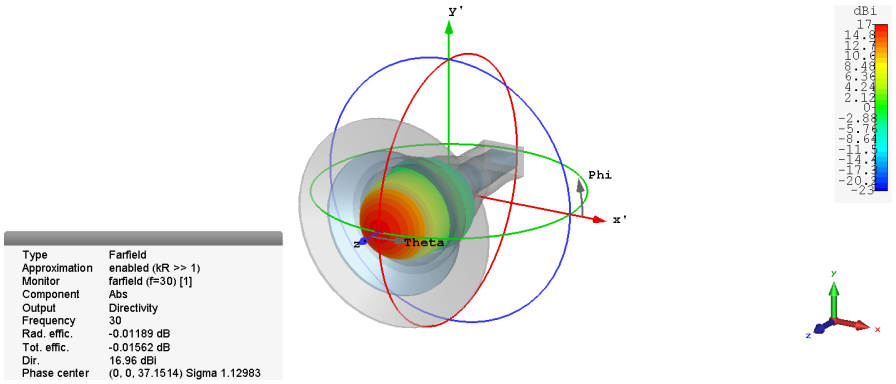

Figure 3.49: Employed feed horn farfield results.

3.3.3.2 Design of RA using innovative unit cell, 24×24 elements

Using the unit cell described in Section 3.3, a 24×24 elements planar RA has been designed, with the following specifications:

- Working band: $29 - 31$ GHz (the design has been done at the central frequency of 30 GHz)
- Cell size: $\frac{\lambda}{2} = 5$ mm
- Number of elements in the x direction: $N_x = 24$

- Number of elements in the y direction: $N_y = 24$
- Aperture $D = 120$ mm
- Beam coordinates: $\theta_b = 25°$ and $\phi_b = 0°$
- Feed coordinates: $f/D = 1$, $\theta_f = 25°$

(for the coordinate systems refer to Section 2.6.3.1).

The required phase of each re-radiating element (evaluated with the formula in Section 2.6.2.1), along with the required W_{side} distribution (evaluated according to the S-curve of Figure 3.39 and referred to simply as W) and the associated error have been evaluated using *Matlab* and depicted in Figure 3.50. Using this unit cell, since the phase range is greater than 360°, the phase error is due to the rounding error between the desired phase values and the actual simulated ones and this is why it is so small with respect to the square patch case.

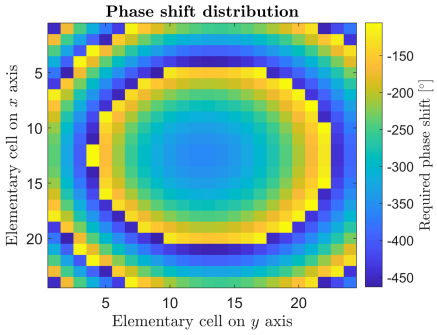

(a) Required phase distribution.

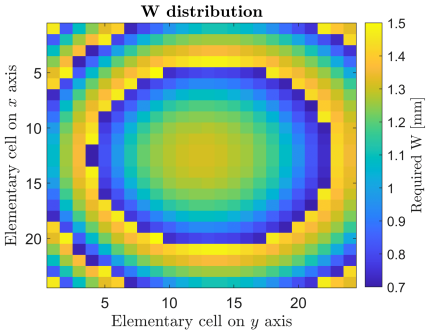

(b) Required W distribution.

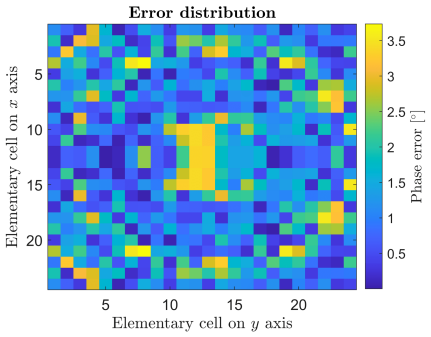

(c) Obtained phase error.

Figure 3.50: Obtained distributions for the designed planar 24×24 RA, using the innovative unit cell.

The designed structure is shown in Figure 3.51.

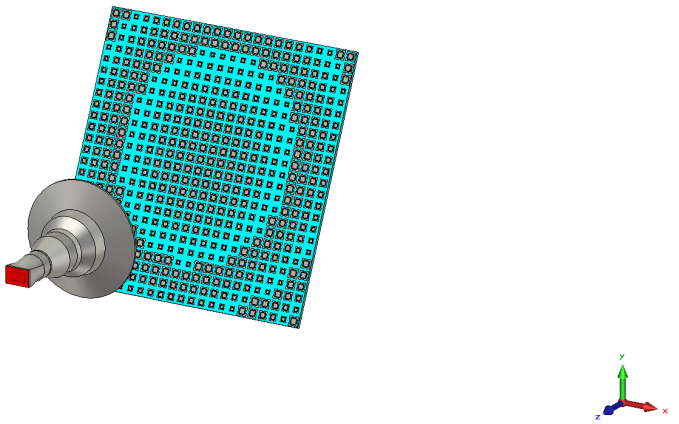

Figure 3.51: Designed planar innovative unit cell 24 × 24 RA.

By using the *CST Microwave Studio* software, a full-wave simulation of the structure has been performed, and the resulting radiation patterns are depicted in Figures 3.52 and 3.53.

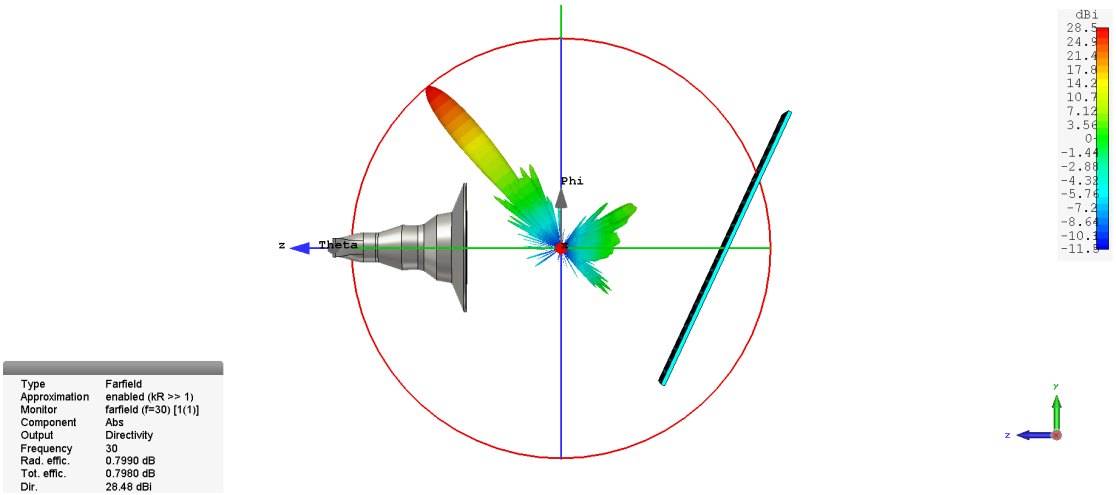

Figure 3.52: 3D radiation pattern at 30 GHz for the planar innovative unit cell 24 × 24 RA.

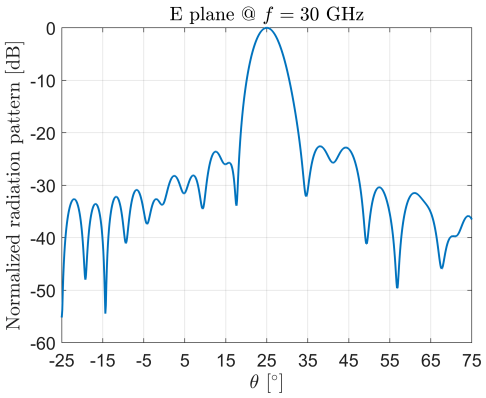

(a) E-plane of the radiation pattern.

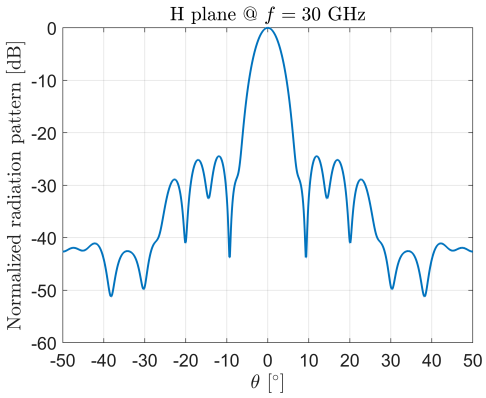

(b) H-plane of the radiation pattern.

Figure 3.53: Radiation pattern cuts at 30 GHz for the planar innovative unit cell 24×24 RA.

In this case, the analysis has been also carried out in the entire frequency band, specifically at 29, 30 and 31 GHz. The results are shown in Figure 3.54.

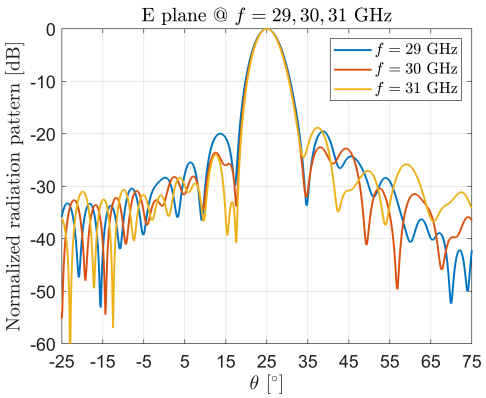

(a) E-plane of the radiation pattern.

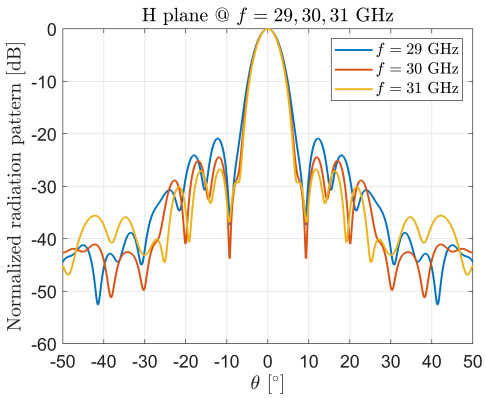

(b) H-plane of the radiation pattern.

Figure 3.54: Radiation pattern cuts at 29, 30 and 31 GHz for the planar innovative unit cell 24×24 RA.

The gain variation in the working frequency band is shown in Figure 3.55.

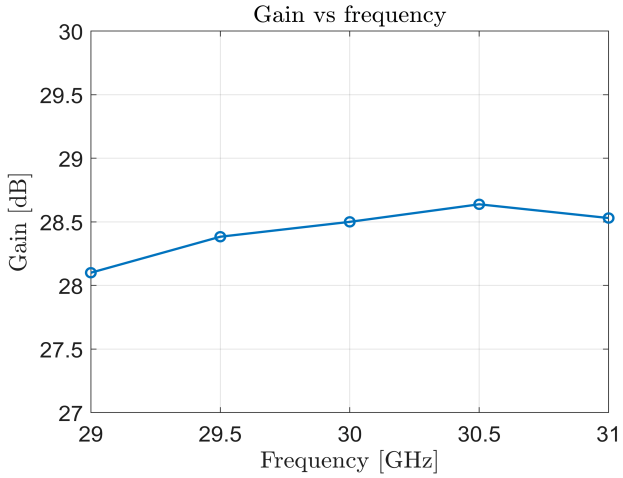

Figure 3.55: Gain versus frequency for the planar innovative unit cell 24 × 24 RA.

From the gain versus frequency plot, depicted in Figure 3.55, it is possible to see that the maximum gain is around 28.5 dB and, from the E and H plane plots shown in Figure 3.53, one can see that the SLL is about -23 dB, at the design frequency.

3.3.3.3 Comparison with the square patch configuration

In this Subsection, the above mentioned 24 × 24 planar configuration is compared with the square patch one, using the same cell size, substrate thickness and all the parameters are kept identical for the two cases. Since the lasts square patch RAs have been designed with a substrate thickness of 0.8 mm and cell size of 4.5 mm, a new S-curve has been obtained from simulations for the square patches, using the same specifications of the innovative unit cell (e.g. substrate thickness of 1.6 mm and so on).

The square patch results taken individually are here omitted, since they provide more interesting results by comparing them with the innovative unit cell ones. The comparison plots of the radiation patterns at 30 GHz are shown in Figure 3.56.

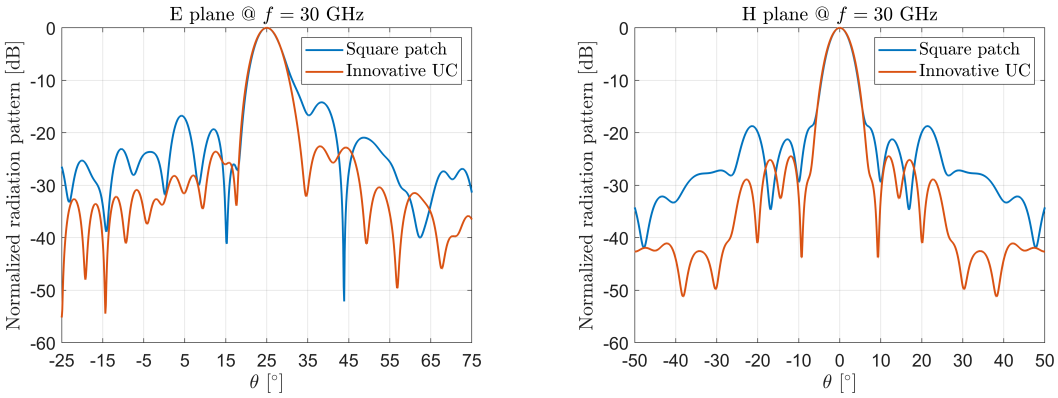

(a) E-plane of the radiation pattern.

(b) H-plane of the radiation pattern.

Figure 3.56: Comparison of the radiation pattern cuts at 30 GHz for the planar innovative unit cell 24×24 RA and the square patch one.

The comparison of the gain variation in the working frequency band is shown in Figure 3.57.

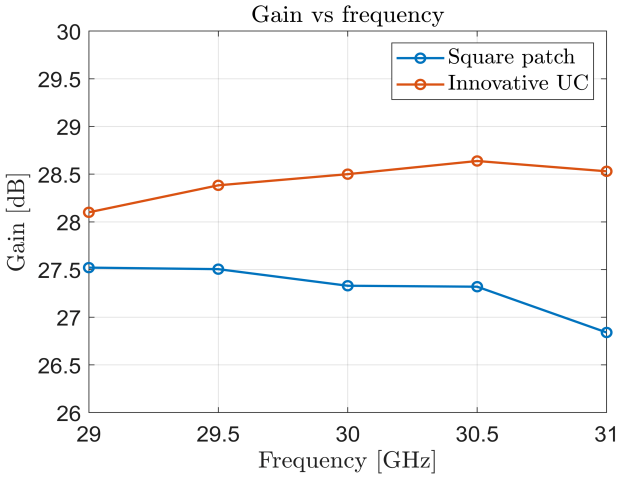

Figure 3.57: Gain versus frequency comparison for the planar innovative unit cell 24×24 RA and the square patch one.

From the gain versus frequency comparison plot, depicted in Figure 3.57, it is possible to observe that the gain of the innovative unit cell configuration is higher. In particular, it is greater than than 1 dB with respect to the square patch one at the design frequency of 30 GHz; this means a meaningful performance improvement.

Also, from the E and H plane comparison plots, shown in Figure 3.56, and from Table 3.1, one can see that, at the design frequency, the SLL is about 8 dB less with respect to the square patch configuration, indicating better performance as well.

Considered unit cell	Gain [dB]	SLL [dB]
Square patch	27.3	-14.3
Innovative UC	28.5	-22.6

Table 3.1: Performance comparison of the RAs at $f = 30$ GHz.

3.3.4 Double parameter technique

There are many methods to increase the number of degrees of freedom to achieve higher performance in terms of bandwidth of a unit cell. As already highlighted in the introduction Chapter, one can use a multi-layer structure, but this increases the manufacturing costs. Another important technique is the so called *Double Parameter technique*.

This technique in based on the variation of two parameters of the unit cell, instead of only one (W_{side}, that has been used up to now). The goal is to use one parameter for the compensation of the spatial phase shift and the other one is used to compensate the phase shift due to the frequency variation in a specific frequency range. As can be seen from Figure 3.58, the dimension of the central square patch has been chosen as the second parameter, called $W_{central}$, in addition to the usual W_{side} parameter. The choice of the parameters is not unique, i.e. one can choose any two independent parameters of the unit cell and make them vary. In this case, the first parameter, W_{side} (in the following, the *first parameter*), and the second one, $W_{central}$ (in the following, the *second parameter*), are used, respectively.

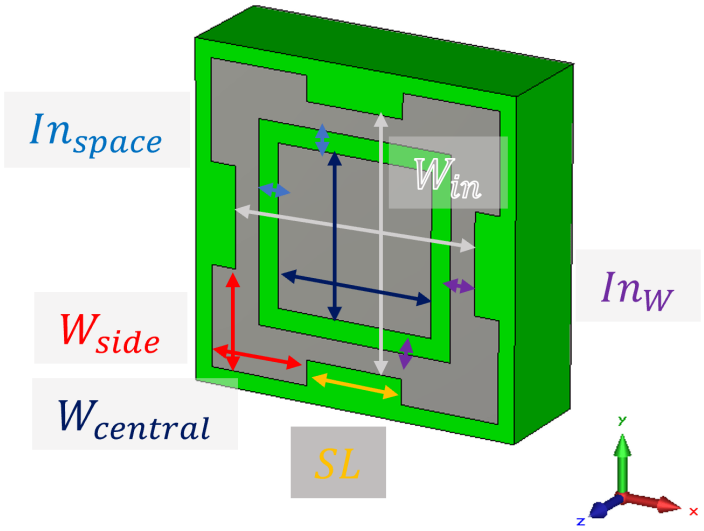

Figure 3.58: Final designed unit cell with double parameter technique.

The geometrical parameter values are

- W_{side} = [0.5,1.5] mm (variable, *first parameter*)
- $W_{central}$ = [0.2,2.8] mm (variable, *second parameter*)

while the other ones are identical with respect to the one parameter unit cell.

An important point is that no all the entire range of variation of the second parameter is used for each value of the first parameter. In fact, one should ensure that the central square patch is not larger with respect to the outer "ring" of the unit cell, in order to avoid superposition. In this case, a condition on the In_{space} parameter has been imposed, that is

$$In_{space} \geq 0.1 \text{ mm} \tag{3.1}$$

in order to get at least 0.1 mm of spacing between the two unit cell parts.

The obtained phase variation is no more a single *curve*, as in the one parameter case, but instead is a *surface*, since the phase is a function of two variables in this case. The obtained magnitude and phase surfaces at 29, 30 and 31 GHz are depicted in Figures 3.59 and 3.60, respectively.

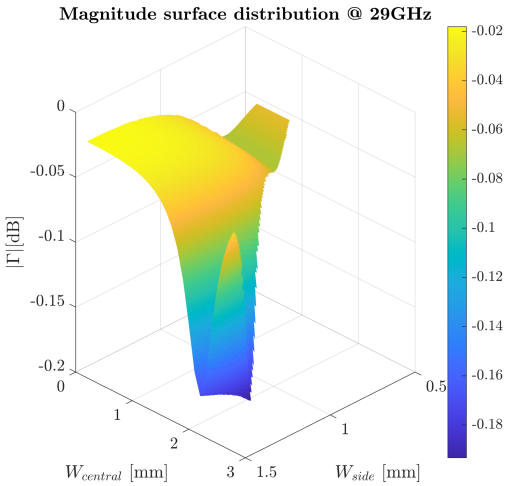

(a) Magnitude surface at 29 GHz.

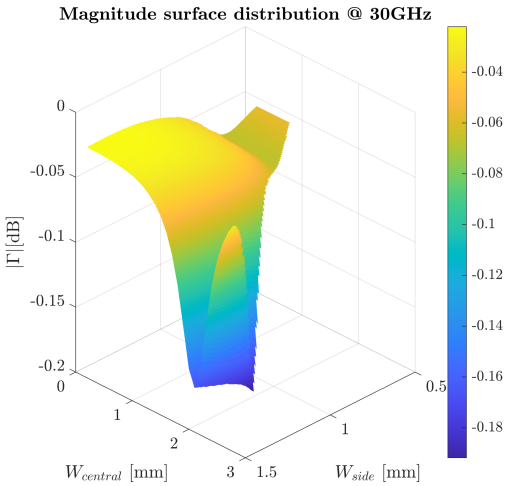

(b) Magnitude surface at 30 GHz.

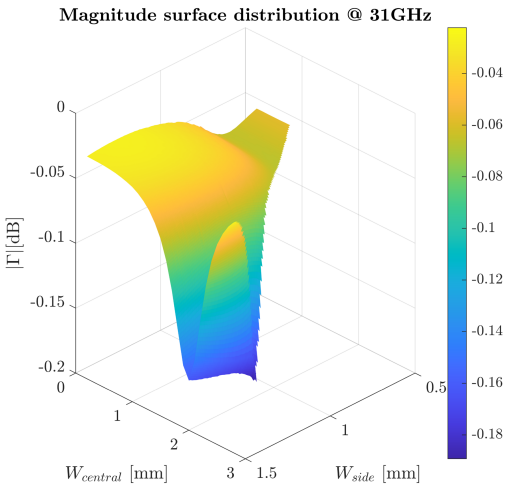

(c) Magnitude surface at 31 GHz.

Figure 3.59: Magnitude surfaces at 29, 30 and 31 GHz for the unit cell.

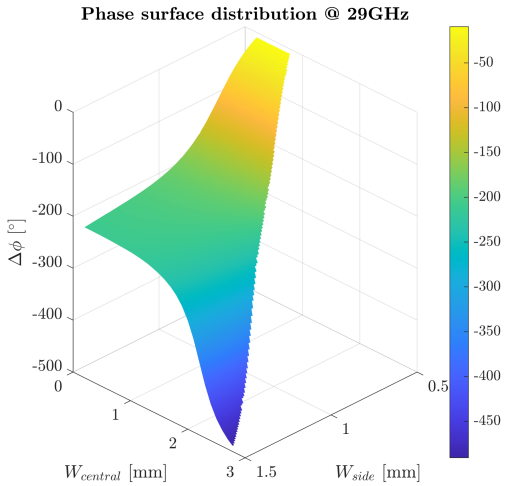

(a) Phase surface at 29 GHz.

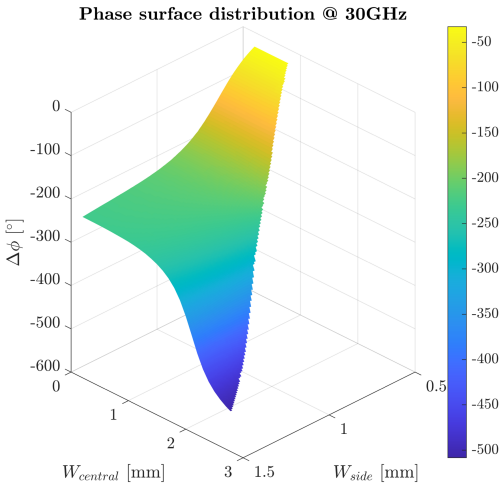

(b) Phase surface at 30 GHz.

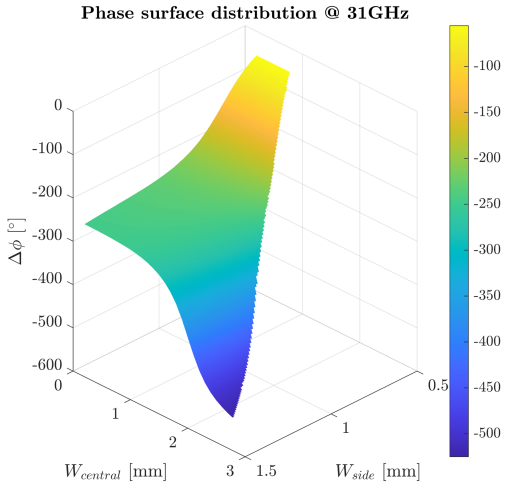

(c) Phase surface at 31 GHz.

Figure 3.60: Phase surfaces at 29, 30 and 31 GHz for the unit cell.

Once all these surfaces have been obtained from simulations, it is necessary to evaluate the so called *difference surface*. Since the goal of the second parameter is to compensate the phase shift introduced by the frequency change, the latter must be evaluated literally as the difference of the surfaces at two different frequencies. For example, if the goal is to compensate the frequency change between 30 and 31

GHz, one should compute the difference between the 30 GHz and 31 GHz phase surfaces, obtaining the related *30-31 GHz difference phase surface*, as in Figure 3.61a.

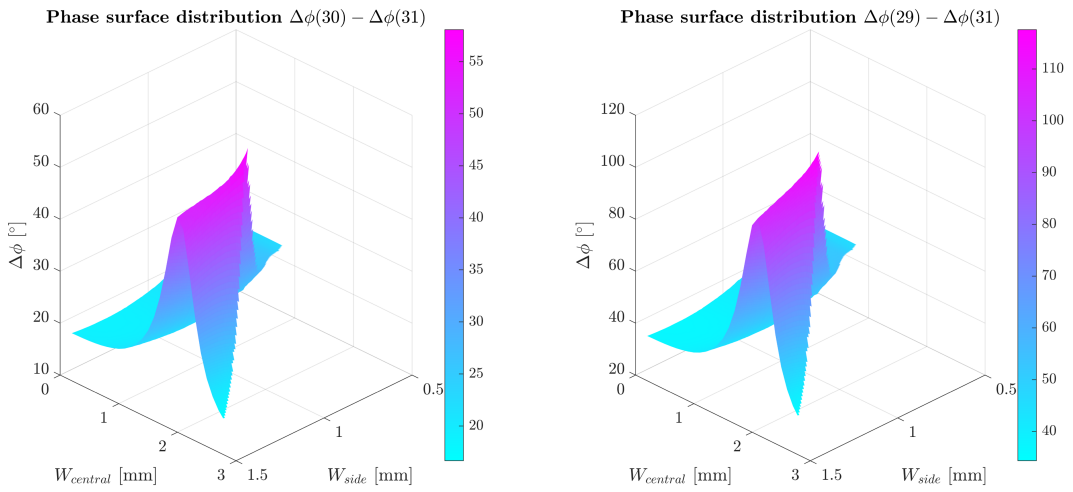

(a) 30-31 GHz difference phase surface.

(b) 29-31 GHz difference phase surface.

Figure 3.61: Difference phase surfaces.

In this case the 30-31 GHz and 29-31 GHz difference surfaces have been evaluated, as shown in Figure 3.61 and will be considered in the following.

As already mentioned, one parameter is used to provide the required spatial delay phase. Once the first parameter has been chosen correctly, for the second parameter we have a set of values to draw from. The latter is used to *compensate* the phase shift due to frequency variation and this compensation, i.e. the choice of the second parameter, can be done in two different ways, as listed below.

- *Minimization* technique: the second parameter value is chosen in such a way that the difference phase surface has minimum value, that is, the simulated phase at the first frequency has minimum variation with respect to the one at the second frequency;

- *Compensation* technique: the second parameter value is chosen in such a way that the difference phase surface has the nearest value with respect to the required phase variation from one frequency to the other one.

Summarizing, using these techniques, it is possible to increase the bandwidth of the surface, because the design is not only done at the desired frequency, but also in the frequency band of interest. In the next Chapter, where these two techniques will be further analyzed and used for the design of the innovative SES, it will be possible to appreciate the advantages of these design techniques with respect to the single parameter one and also to quantify the related performance increase from the perspective of gain or *Radar Cross Section* (RCS) (using a *Plane Wave* as the source of the impinging field) and bandwidth, by using *CST Microwave Studio* software to simulate the structures and analyzing the related radiation patterns.

Chapter 4

Design of innovative smart electromagnetic surfaces

The goal is to design a SES, where the electromagnetic field that is incident on the designed surface is modeled as a plane wave, that is, a type of wave that has constant and uniform wavefront, propagating in a certain direction, perpendicular with respect to them, working in the band $29 - 31$ GHz.

The design process starts from a RA with the feed in order to evaluate the performance of it by using square patches. Then, the f/D parameter (the distance between the feed and the surface) will be increased more and more, emulating the *far field* condition. This is very useful because, moving the feed away from the surface, allows getting closer and closer to the condition of incident plane wave. In this way, the behavior and the performance of the surface can be analyzed and design decisions can be made accordingly.

Since the increase in performance of the innovative unit cell with respect to the square patch has already been demonstrated in Section 3.3.3.3, it will be possible to design the innovative smart electromagnetic surface by making use of the new unit cell and the plane wave source, avoiding the use of the feed. In this case, a new formula for the required phase for each surface element will be provided, for both the planar and conformal case.

Time domain simulations are carried out to obtain the corresponding radiation patterns and performance of some designed surfaces.

Finally, some SESs will be designed with particular constraints in order to be accommodated in the urban environment, for example on public lighting, since, as already mentioned in a past Chapter, this latter is the final goal of this work. Also, the *Double Parameter* technique has been used and conclusions will be then drawn on these last designs.

4.1 Design of RA using square patches

In this section some preliminary results on RAs with square patches are presented, for both planar and conformal cases, using the feed horn illustrated in Section 3.3.3.1.

The parameters of the square patch unit cell that has been used are:

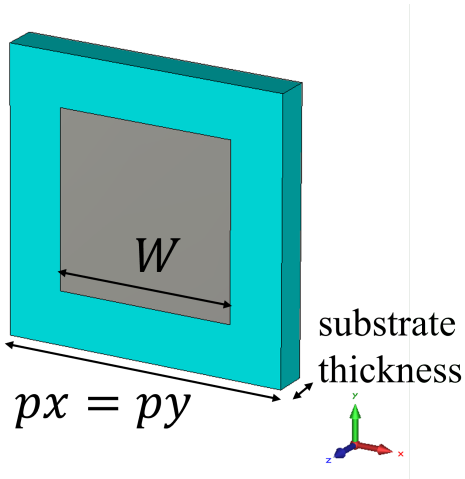

Figure 4.1: Square patch unit cell.

Substrate:

- material: Diclad527, with $\varepsilon_r = 2.55$, $\tan\delta = 0.0022$
- thickness: 0.8 mm
- cell size: $px = py \approx \frac{\lambda}{2} = 4.5$ mm (horizontal and vertical dimensions)

Metal patch:

- $W = [0.5,4]$ mm (square side, variable)

- thickness: 0 mm (PEC)

Considering the infinite array approach, the unit cell has been analyzed with the *CST Microwave Studio* software, in order to compute the phase of the reflected field, varying W between 0.5 and 4 mm. The obtained S-curve is depicted in Figure 4.2.

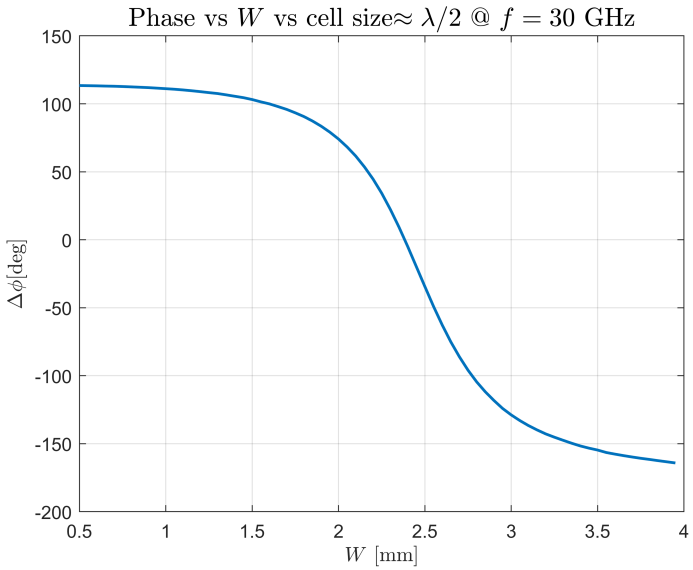

Figure 4.2: Square patch unit cell S-curve.

It is possible to see that the obtained phase range is about 270°, that is less with respect to the ideal 360°, as mentioned in Section 2.2. The steepness of the curve is limited since the cell size is chosen to be less than half wavelength.

4.1.1 Planar RA with 41×41 elements

Using the square patch unit cell shown before, a 41×41 elements RA has been designed, with the following specifications:

- Working band: $29 - 31$ GHz (the design has been done at the central frequency of 30 GHz)
- Cell size: $\approx \frac{\lambda}{2} = 4.5$ mm
- Number of elements in the x direction: $N_x = 41$

- Number of elements in the y direction: $N_y = 41$
- Aperture $D = 184.5$ mm
- Beam coordinates: $\theta_b = 25°$ and $\phi_b = 0°$
- Feed coordinates: $f/D = 1.2$, $\theta_f = 25°$

(for the coordinate systems refer to Section 2.6.3.1).

The required phase of each re-radiating element (evaluated with the formula in Section 2.6.2.1), along with the required W distribution (evaluated according to the S-curve of Figure 4.2) and the associated error (due to the phase range that is less than 360°) have been evaluated using *Matlab* and depicted in Figure 4.3.

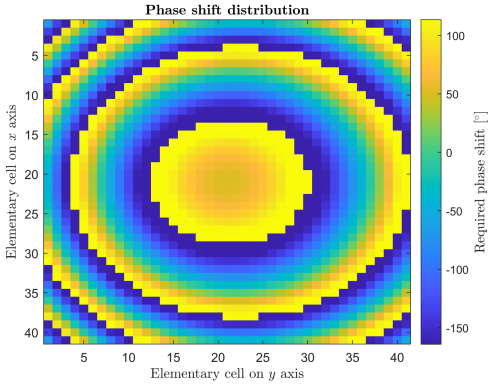

(a) Required phase distribution.

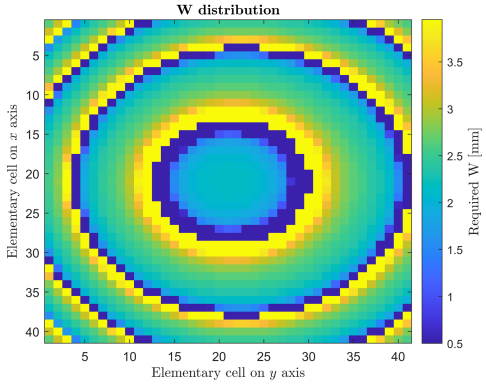

(b) Required W distribution.

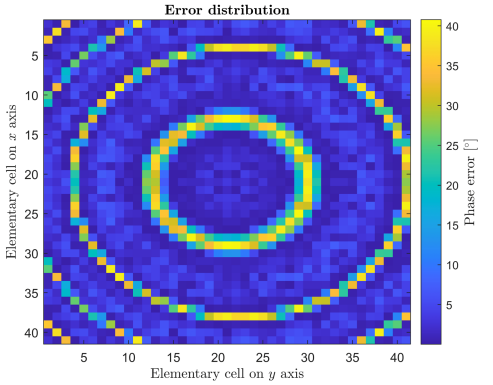

(c) Obtained phase error.

Figure 4.3: Obtained distributions for the designed planar square patch 41×41 RA,

The designed structure is shown in Figure 4.4.

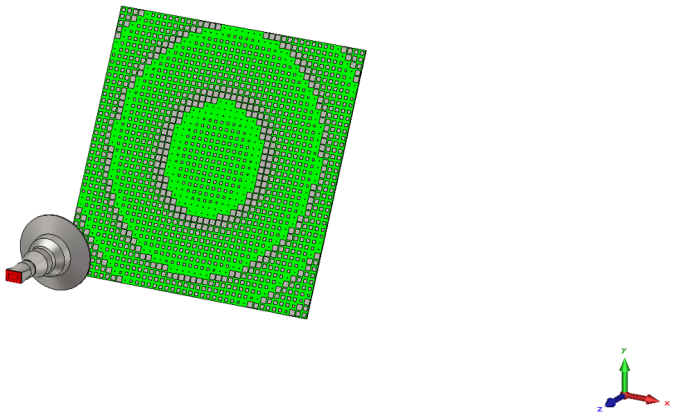

Figure 4.4: Designed planar square patches 41 × 41 RA,

By using the *CST Microwave Studio* software, a full-wave simulation of the structure has been performed, and the resulting radiation patterns are depicted in Figures 4.5 and 4.6.

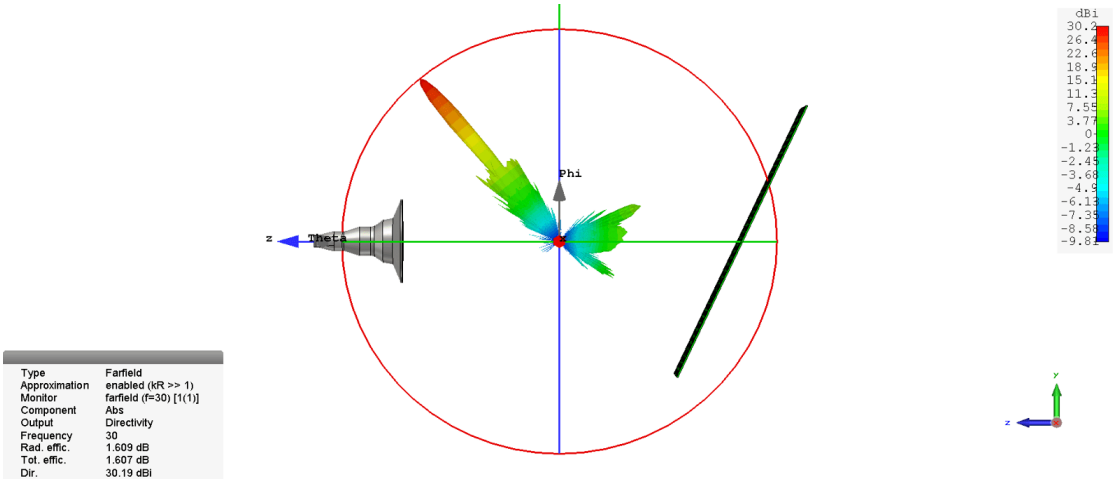

Figure 4.5: 3D radiation pattern at 30 GHz for the planar square patches 41 × 41 RA,

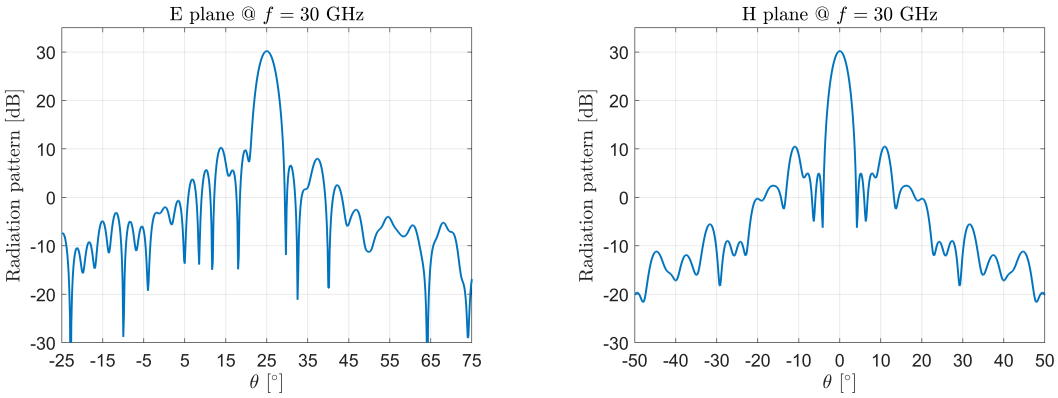

(a) E-plane of the radiation pattern.

(b) H-plane of the radiation pattern.

Figure 4.6: Radiation pattern cuts at 30 GHz for the planar square patches 41×41 RA,

From the E and H planes it is possible to see that the maximum gain is around 30 dB and the SLL is about -20 dB.

In these first examples the simulation of the RAs has been carried out only at the design frequency of 30 GHz and not in the entire bandwidth: this will be done in the next stages.

4.1.2 Conformal RA with $R = 20\lambda$, 41×41 elements

Using the square patch unit cell shown before, a 41×41 elements CRA has been designed, with the following specifications:

- Working band: $29 - 31$ GHz (the design has been done at the central frequency of 30 GHz)
- Cell size: $\approx \frac{\lambda}{2} = 4.5$ mm
- Number of elements in the x direction: $N_x = 41$
- Number of elements in the y direction: $N_y = 41$
- Aperture $D = 184.5$ mm
- Beam coordinates: $\theta_b = 25°$ and $\phi_b = 0°$

- Feed coordinates: $f/D = 1.2$, $\theta_f = 25°$
- Radius of curvature: $R = 20\lambda$

(for the coordinate systems refer to Section 2.6.3.1).

The required phase of each re-radiating element (evaluated with the formula in Section 2.6.2.2), along with the required W distribution (evaluated according to the S-curve of Figure 4.2) and the associated error (due to the phase range that is less than 360°) have been evaluated using *Matlab* and depicted in Figure 4.7.

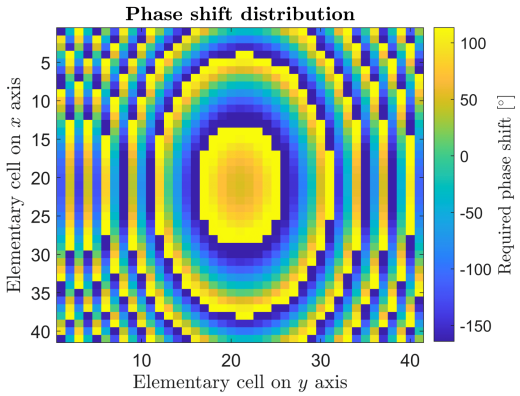

(a) Required phase distribution.

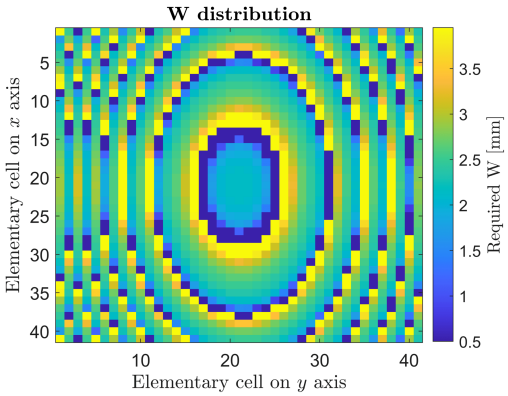

(b) Required W distribution.

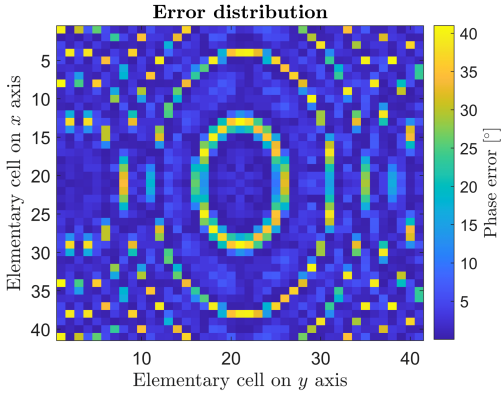

(c) Obtained phase error.

Figure 4.7: Obtained distributions for the designed conformal square patch $R = 20\lambda$, 41×41 RA,

The designed structure is shown in Figure 4.8.

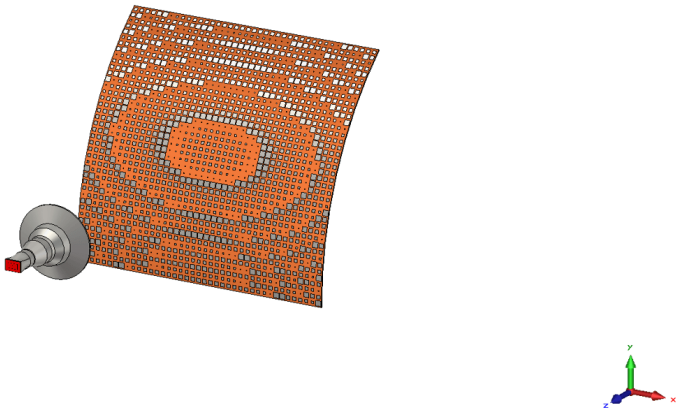

Figure 4.8: Designed conformal square patches $R = 20\lambda$, 41×41 RA,

By using the *CST Microwave Studio* software, a full-wave simulation of the structure has been performed, and the resulting radiation patterns are depicted in Figures 4.9 and 4.10.

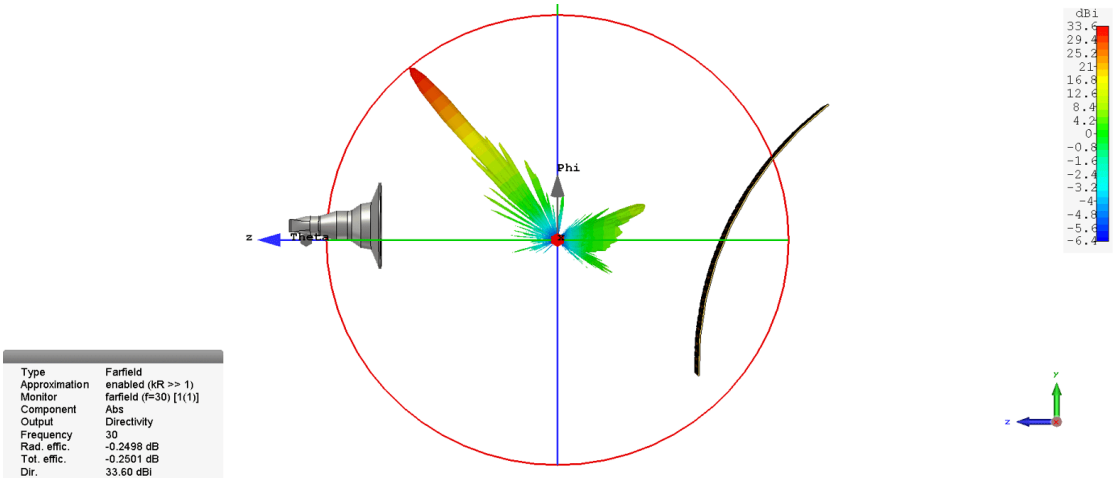

Figure 4.9: 3D radiation pattern at 30 GHz for the conformal square patches 41×41 RA,

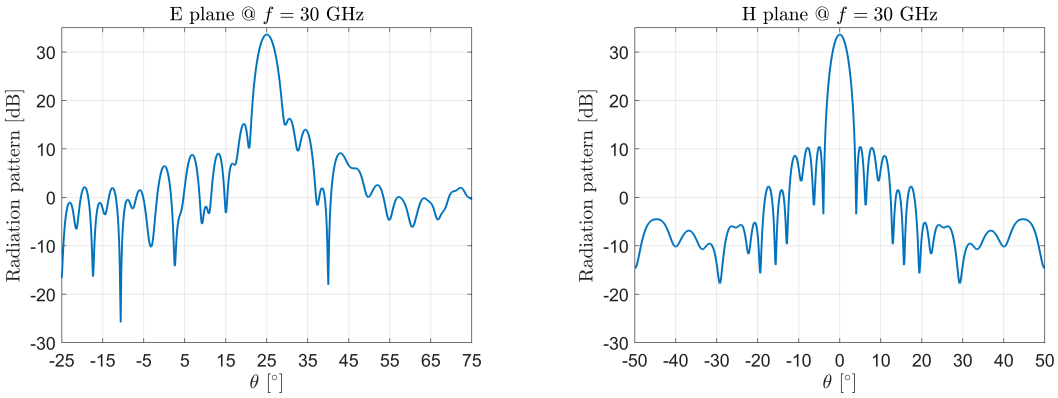

(a) E-plane of the radiation pattern.

(b) H-plane of the radiation pattern.

Figure 4.10: Radiation pattern cuts at 30 GHz for the conformal square patches $R = 20\lambda$, 41×41 RA,

From the E and H planes it is possible to see that the maximum gain is approximately 33.6 dB and the SLL is around -17.4 dB. As can be seen from Figure 4.10, by using a conformal configuration with a relatively small radius of curvature (i.e. a very steep curvature of the surface) the maximum gain increases but the sidelobe level increases too, as we expected from the analysis shown in Chapter 2.

4.1.3 Feed distancing

The purpose of this Section is to increase the focal distance f/D from 10 to 40 in order to evaluate the performance of the structure in a condition in which the feed is positioned far away from the re-radiating elements, emulating the far field condition.
Using the square patch unit cell shown before, a 43×43 elements RA has been designed with the following specifications:

- Working band: $29 - 31$ GHz (the design has been done at the central frequency of 30 GHz)
- Cell size: $\approx \frac{\lambda}{2} = 4.5$ mm
- Number of elements in the x direction: $N_x = 43$
- Number of elements in the y direction: $N_y = 43$

- Aperture $D = 193.5$ mm
- Beam coordinates: $\theta_b = 25°$ and $\phi_b = 0°$
- Feed coordinates: $f/D = 10 \rightarrow 40$, $\theta_f = 25°$
- Radius of curvature: $R = 18\lambda$

(for the coordinate systems refer to Section 2.6.3.1).

In this case, a slightly larger (43×43) with respect to the previous ones (41×41) CRA has been designed, with a curvature radius of 18λ, slightly smaller with respect to the previous one, which means an increased curvature of the surface. The phase distributions obtained for all the focal distances are reported in Figures 4.11 and 4.12.

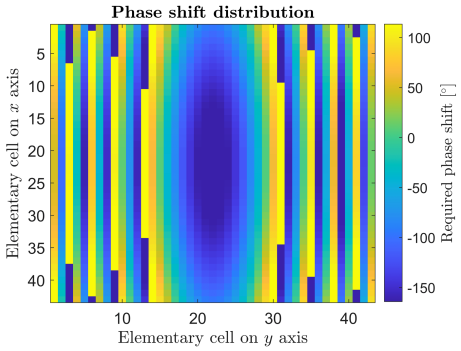

(a) Required phase distribution with $f/D = 10$.

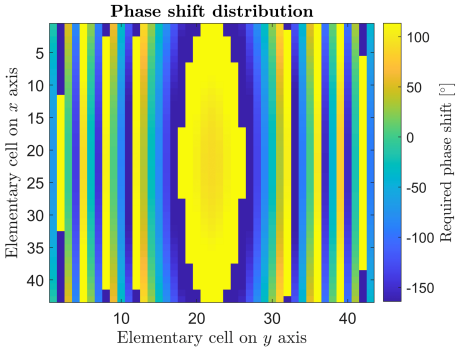

(b) Required phase distribution with $f/D = 15$.

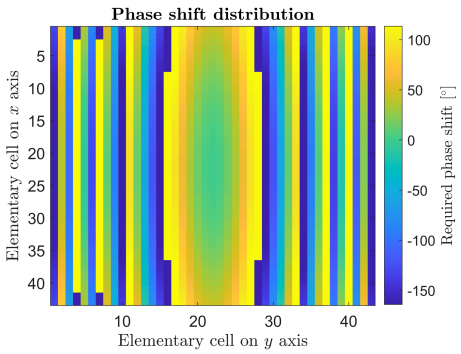

(c) Required phase distribution with $f/D = 20$.

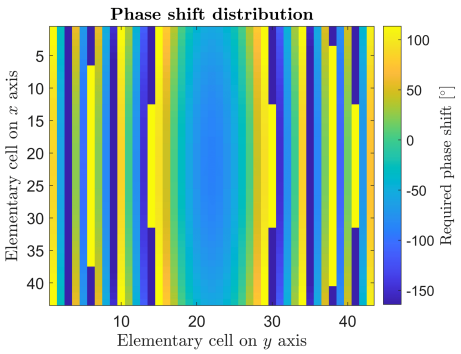

(d) Required phase distribution with $f/D = 25$.

Figure 4.11: Obtained phase distributions for the designed conformal square patch $R = 18\lambda$, 43×43 RA, increasing f/D from 10 to 25.

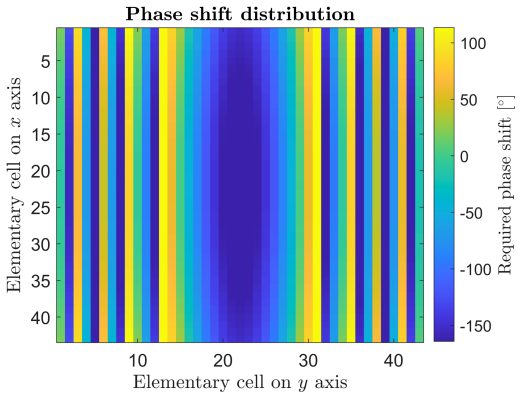

(a) Required phase distribution with $f/D = 30$.

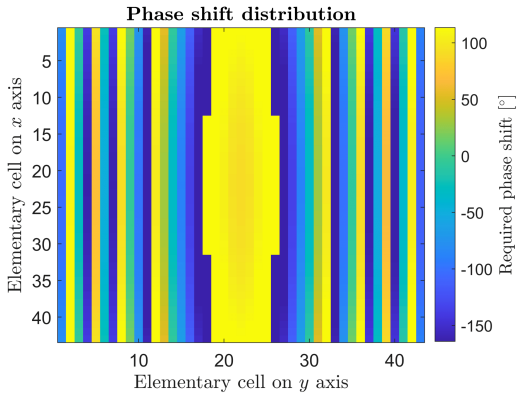

(b) Required phase distribution with $f/D = 35$.

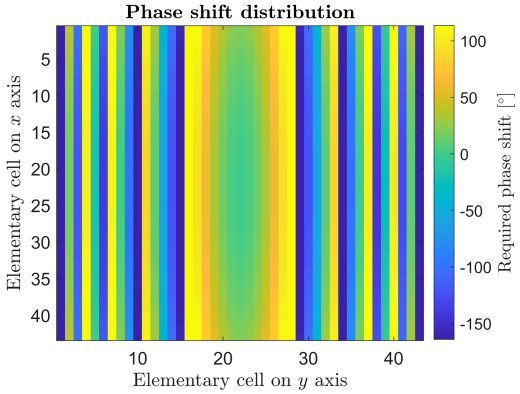

(c) Required phase distribution with $f/D = 40$.

Figure 4.12: Obtained phase distributions for the designed conformal square patch $R = 18\lambda$, 43×43 RA, increasing f/D from 30 to 40.

As can be seen from Figures 4.11 and 4.12, when the distance between the feed and the surface increases more and more, the required phase distribution tends to be the one required from a plane wave, i.e. with constant phase vertical lines, as will be shown in the following.

As an example, the configurations with $f/D = 10$, 25 and 40 are then analyzed at this point.

4.1.3.1 Configuration with $f/D = 10$

Considering $f/D = 10$ as the focal distance, the designed structure is shown in Figure 4.13.

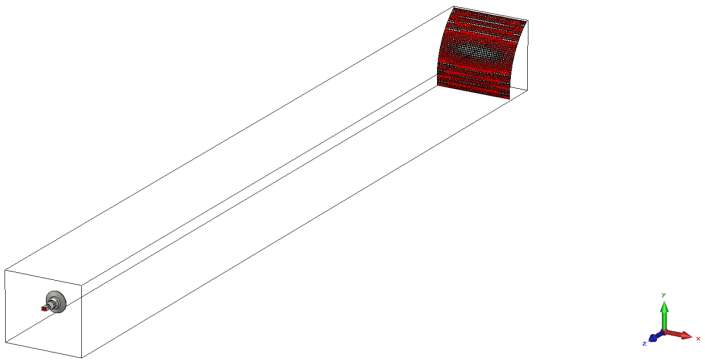

Figure 4.13: Designed conformal square patches RA with $f/D = 10$.

By using the *CST Microwave Studio* software, a full-wave simulation of the structure has been performed, and the resulting radiation patterns are depicted in Figures 4.14 and 4.15.

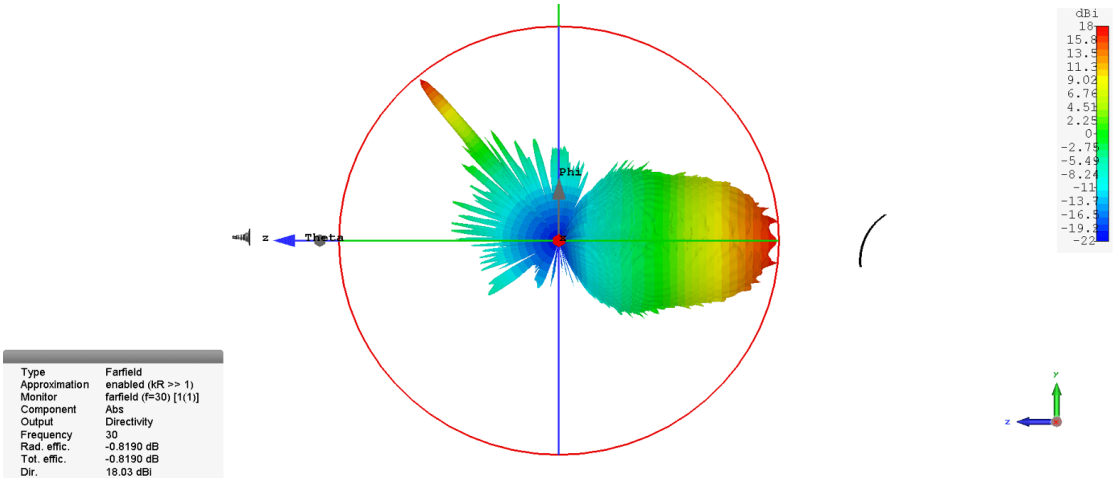

Figure 4.14: 3D radiation pattern at 30 GHz for the conformal square patches RA with $f/D = 10$.

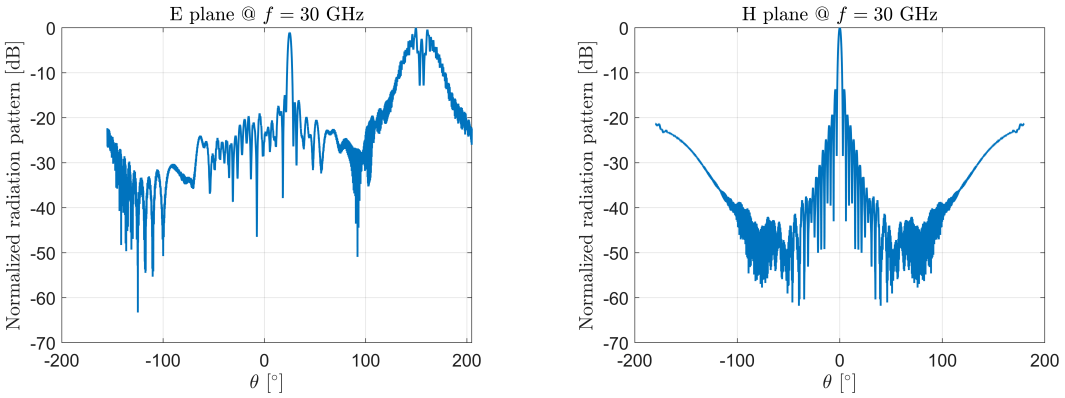

(a) E-plane of the radiation pattern.

(b) H-plane of the radiation pattern.

Figure 4.15: Radiation pattern cuts at 30 GHz for the conformal square patches with $f/D = 10$.

As can be seen from Figure 4.15, using a feed far away from the surface produces an higher back-lobe, where most of the energy is lost. This is because the contribution of the illumination system is predominant with respect to the re-radiated field from the RA, due to the high focal distance.

4.1.3.2 Configuration with $f/D = 25$

Considering $f/D = 25$ as the focal distance, the designed structure is shown in Figure 4.16.

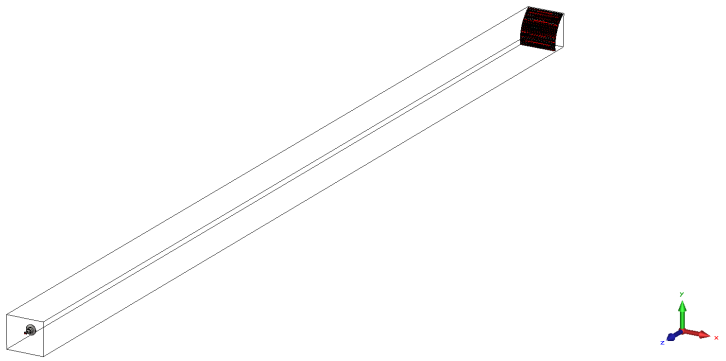

Figure 4.16: Designed conformal square patches RA with $f/D = 25$.

By using the *CST Microwave Studio* software, a full-wave simulation of the

structure has been performed, and the resulting radiation patterns are depicted in Figures 4.17 and 4.18.

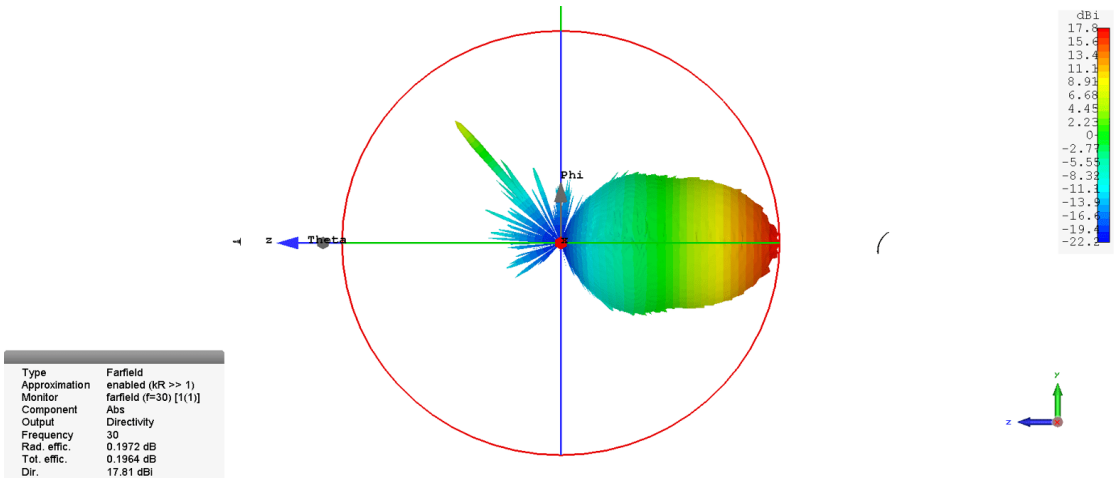

Figure 4.17: 3D radiation pattern at 30 GHz for the conformal square patches RA with $f/D = 25$.

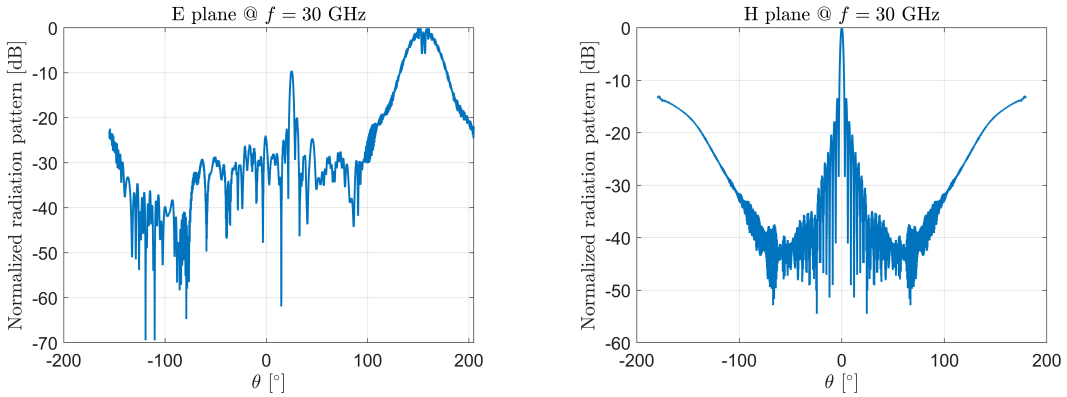

(a) E-plane of the radiation pattern.

(b) H-plane of the radiation pattern.

Figure 4.18: Radiation pattern cuts at 30 GHz for the conformal square patches with $f/D = 25$.

As can be seen from Figure 4.18, using a feed further away from the surface, with respect to the $f/D = 10$ configuration, produces an higher back-lobe, where most of the energy is concentrated.

4.1.3.3 Configuration with $f/D = 40$

Considering now $f/D = 40$, i.e. a very large value of the focal distance, the designed structure is shown in Figure 4.19.

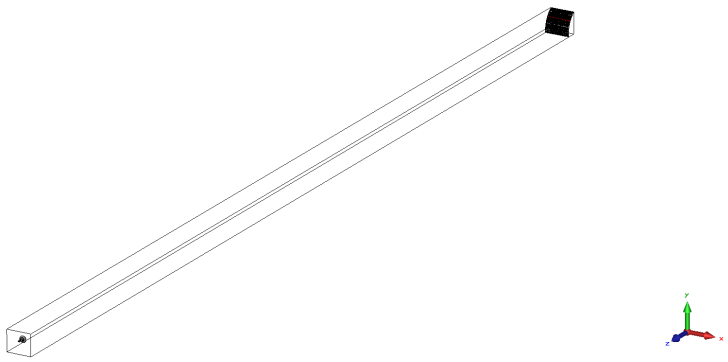

Figure 4.19: Designed conformal square patches RA with $f/D = 40$.

By using the *CST Microwave Studio* software, a full-wave simulation of the structure has been performed, and the resulting radiation patterns are depicted in Figures 4.20 and 4.21.

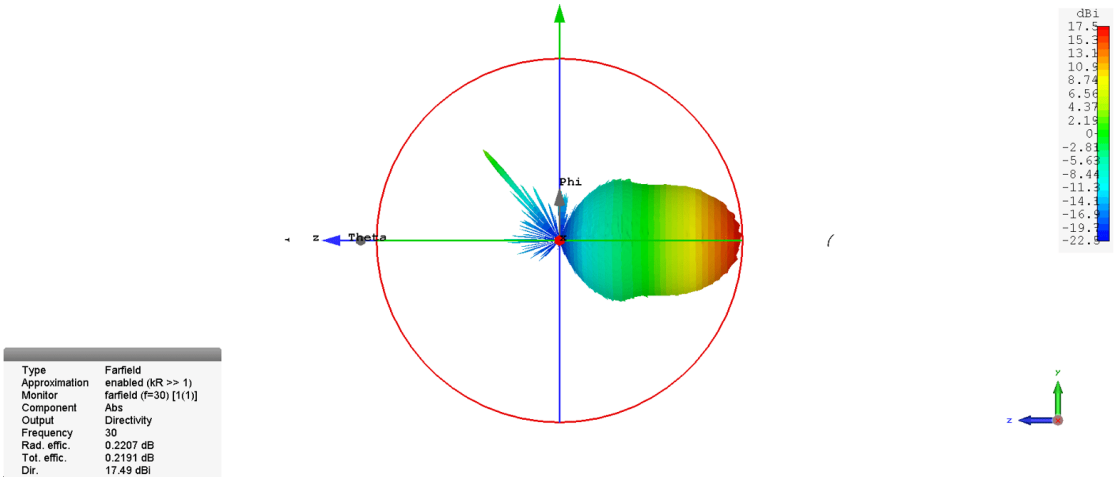

Figure 4.20: 3D radiation pattern at 30 GHz for the conformal square patches RA with $f/D = 40$.

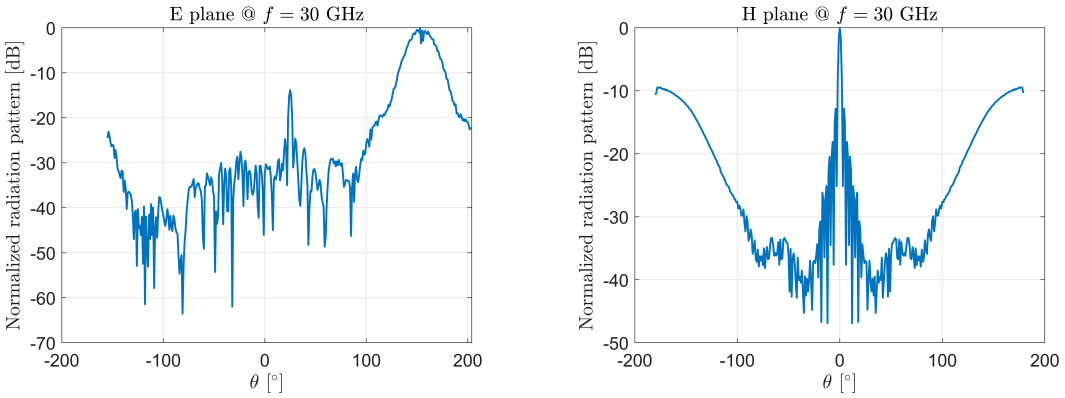

(a) E-plane of the radiation pattern.

(b) H-plane of the radiation pattern.

Figure 4.21: Radiation pattern cuts at 30 GHz for the conformal square patches with $f/D = 40$.

As can be seen from Figure 4.21, using a feed far away from the surface produces an higher back-lobe, where most of the energy is lost. In this case the main lobe contains much less energy compared to the $f/D = 10$ case and this is obviously due to the increased feed-surface distance which implies less efficiency and the predominant contribution is, even more so, the illumination system one.

4.1.3.4 Configuration with $f/D = 15$ and larger aperture

Considering now $f/D = 15$, the goal here is to study the radiation performance of the antenna, by increasing its aperture. The main advantage is that, using a larger antenna, the spillover efficiency will increase, reducing consequently the back-lobe contribution. The designed structure is shown in Figure 4.22. The antenna aperture has been increased by 2.5 times with respect to the previous cases, that is from $D_{old} = 193.5$ mm to $D = 2.5 \cdot D_{old}$. In order to speed up the simulation process and, after having verified beforehand the low dependency of performance on the curvature radius, the larger aperture antenna has been designed by using a planar structure, while the smaller aperture one is still conformal, as in the previous cases.

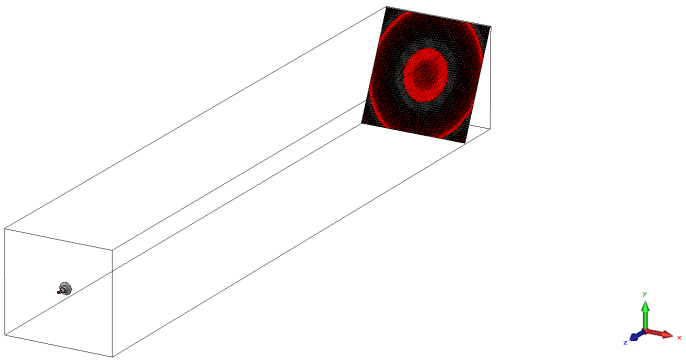

Figure 4.22: Designed planar square patches RA with $f/D = 15$ and $D = 2.5 \cdot D_{old}$.

By using the *CST Microwave Studio* software, a full-wave simulation of the structure has been performed, and the resulting radiation patterns are depicted in Figures 4.23 and 4.24.

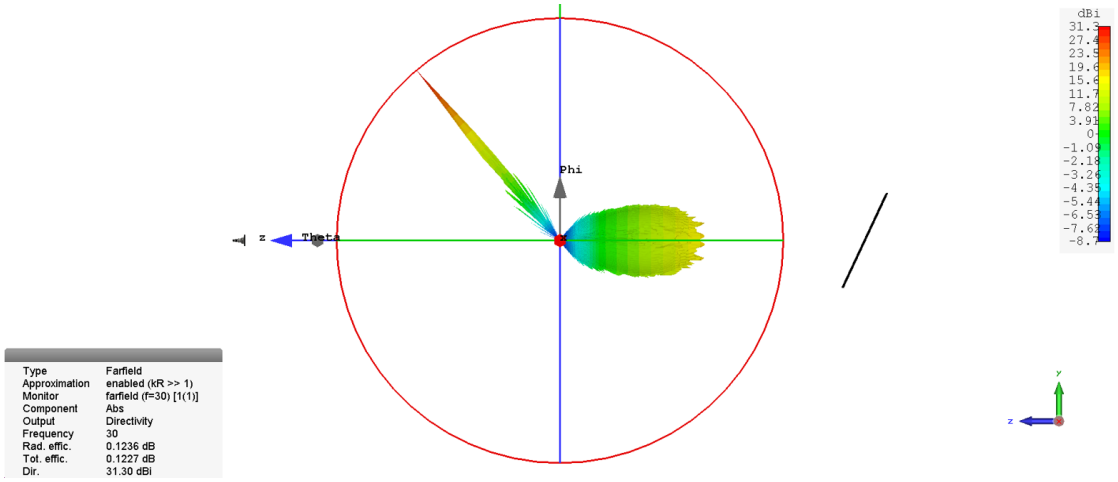

Figure 4.23: 3D radiation pattern at 30 GHz for the square patches RA with $f/D = 15$ and $D = 2.5 \cdot D_{old}$.

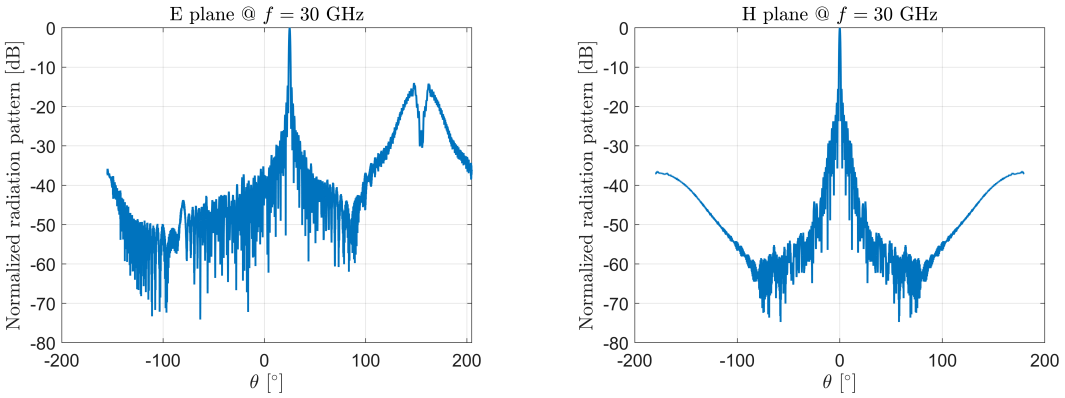

(a) E-plane of the radiation pattern. **(b)** H-plane of the radiation pattern.

Figure 4.24: Radiation pattern cuts at 30 GHz for the square patches RA with $f/D = 15$ and $D = 2.5 \cdot D_{old}$.

At this point, it is meaningful to compare the results obtained using the two apertures, that are D_{old} and $D = 2.5 \cdot D_{old}$, at fixed $f/D = 15$. The results are depicted in Figure 4.25.

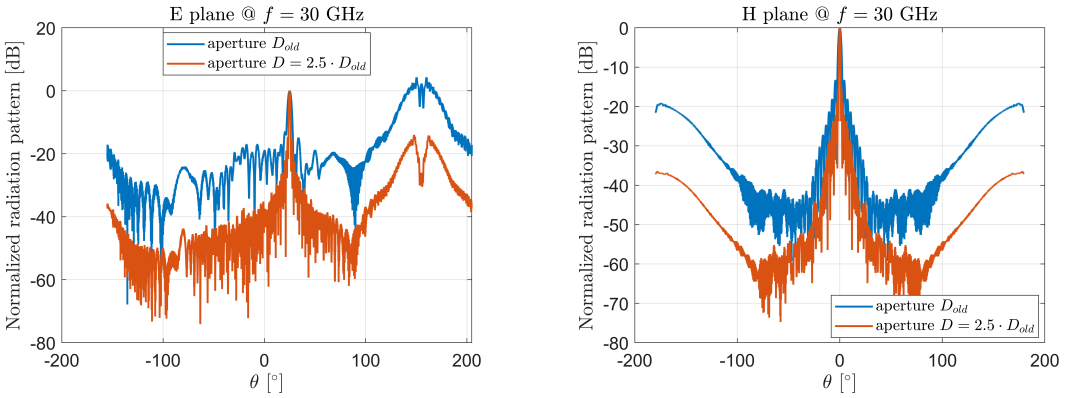

(a) E-plane of the radiation pattern. **(b)** H-plane of the radiation pattern.

Figure 4.25: Radiation pattern cuts at 30 GHz for the two square patches RAs with $f/D = 15$, comparing the two different antenna apertures.

As can be seen from Figure 4.25, using a larger aperture antenna produces a lower back-lobe with respect to the smaller aperture antenna configuration; as already mentioned, this can be explained by the increase of the spillover efficiency

thanks to the larger antenna surface.

4.2 Design of SES using incident plane wave

From the feed distancing process previously analyzed, some simulations with an incident plane wave are now analyzed in order to simulate a field source at infinite distance with respect to the surface. Both square patches and the innovative unit cell are employed in order to compare their performance.

4.2.1 Planar case phase distribution

In this part, the required phase for each patch element is evaluated in the case of an incident plane wave on the antenna surface.

In order to get a beam in a certain direction, the phase distribution for a planar reflectarray antenna can be evaluated as

$$\phi(x_i, y_i) = -k_0 \sin\theta_b \cos\phi_b \, x_i - k_0 \sin\theta_b \sin\phi_b \, y_i \tag{4.1}$$

as already explained in Section 2.6.2.1.

The reflected field can be written as the incident field plus the phase shift introduced by each element, that is

$$\phi(x_i, y_i) = -k_0 \, d_i + \phi_R(x_i, y_i) \tag{4.2}$$

being $\phi_R(x_i, y_i)$ the required phase of each element.

When the field source is at infinity, i.e. a far-field plane wave source, it is possible to reduce the term $k_0 d_i$ to

$$k_0 d_i = k_0 (x_i \sin\theta_I \cos\phi_I + y_i \sin\theta_I \sin\phi_I) \tag{4.3}$$

being (θ_I, ϕ_I) the incident plane wave direction for which it is desired to deflect the field to (θ_b, ϕ_b) [53], using the reference system of Section 2.6.3.1 with $\theta_I = \theta_f$ and $\phi_I = \phi_f$.

It is possible to evaluate the required phase shift for each element by solving 4.2

for $\phi_R(x_i, y_i)$:

$$\phi_R(x_i, y_i) = k_0\{x_i[\sin\theta_I \cos\phi_I + \sin\theta_b \cos\phi_b] + y_i[\sin\theta_I \sin\phi_I + \sin\theta_b \sin\phi_b]\} \quad (4.4)$$

As an example, the required phase distribution has been evaluated using *Matlab*, for a normal incidence plane wave ($\theta_I = 0°, \phi_I = 0°$) and a 30° tilted reflected pencil beam ($\theta_b = 30°, \phi_b = 0°$) SES. The surface is a 24×24 elements planar square patch SES and the required phase distribution is shown in Figure 4.26, at frequency $f = 30$ GHz and 0.5λ cell size.

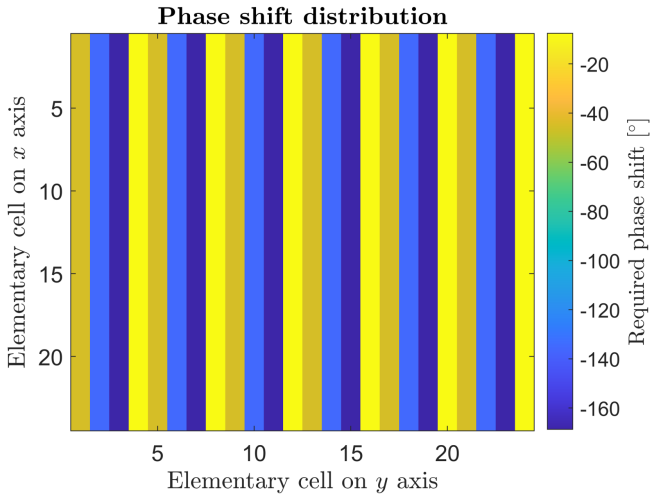

Figure 4.26: Required phase distribution for a square patch planar 24×24 SES with incident plane wave.

4.2.2 Planar SES square patch and innovative unit cell comparison

4.2.2.1 Square patch SES with 24×24 elements

Using the square patch unit cell, a 24×24 elements SES has been designed, with the following specifications:

- Working band: $29 - 31$ GHz (the design has been done at the central frequency of 30 GHz)
- Cell size: $\frac{\lambda}{2} = 5$ mm
- Number of elements in the x direction: $N_x = 24$
- Number of elements in the y direction: $N_y = 24$
- Aperture $D = 120$ mm
- Beam coordinates: $\theta_b = 30°$ and $\phi_b = 0°$
- Direction of arrival of the plane wave: $\theta_I = 0°$ and $\phi_I = 0°$

(for the coordinate systems refer to Section 2.6.3.1).
The required phase of each re-radiating element (evaluated with the formula in Section 4.2.1), along with the required W distribution (evaluated according to the already mentioned square patch unit cell with the same specification of the innovative unit cell ones, e.g. thickness of 1.6 mm and so on) and the associated error (due to the phase range that is less than 360°) have been evaluated using *Matlab* and depicted in Figure 4.27.

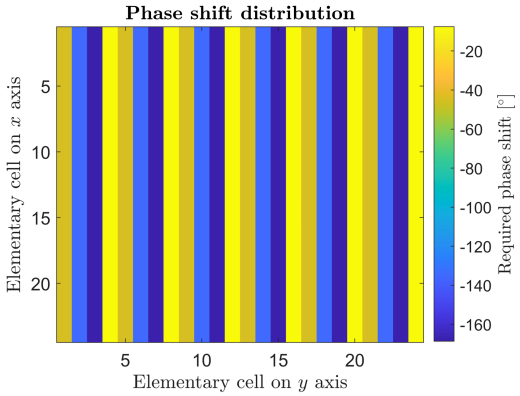

(a) Required phase distribution.

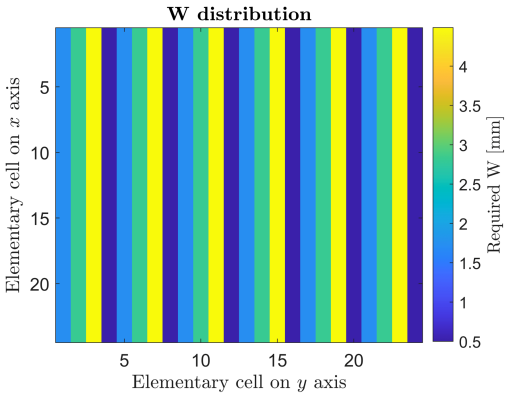

(b) Required W distribution.

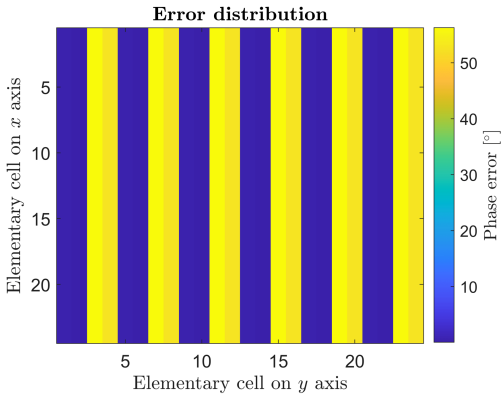

(c) Obtained phase error.

Figure 4.27: Obtained distributions for the designed planar square patch 24×24 SES.

The designed structure is shown in Figure 4.28.

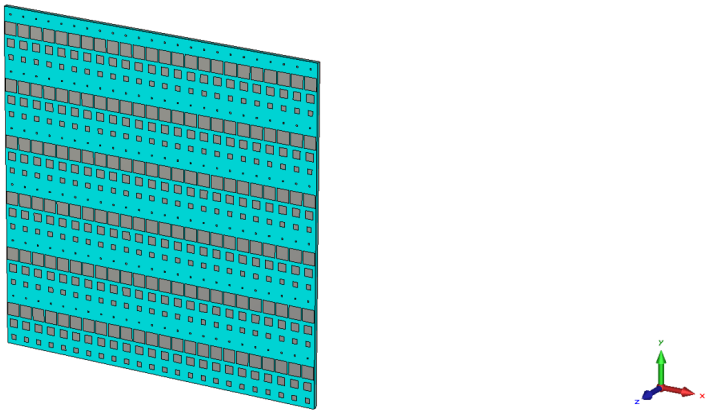

Figure 4.28: Designed planar square patches 24×24 SES.

By using the *CST Microwave Studio* software, a full-wave simulation of the structure has been performed, and the resulting radiation patterns at 29, 30 and 31 GHz are depicted in Figures 4.29 and 4.30.

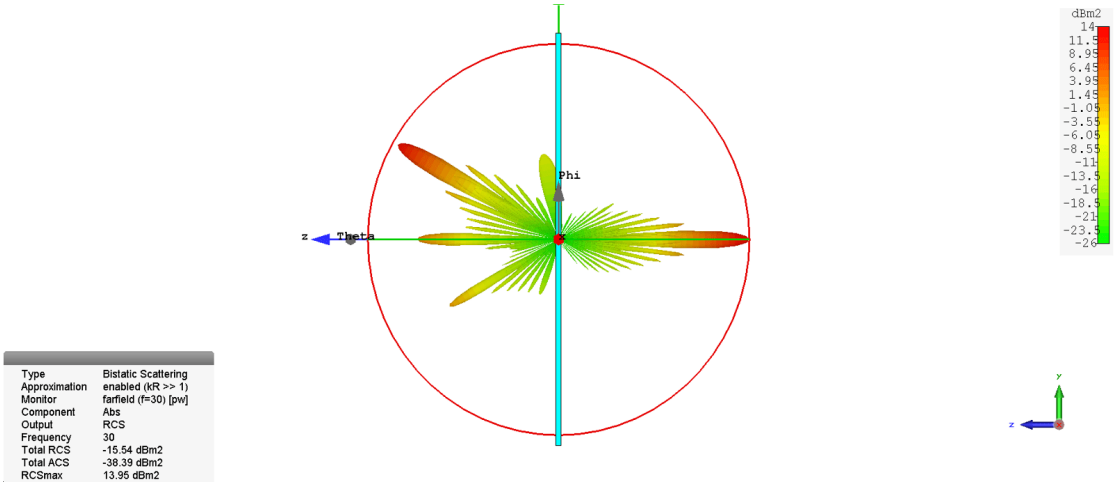

Figure 4.29: 3D radiation pattern at 30 GHz for the planar square patches 24×24 SES.

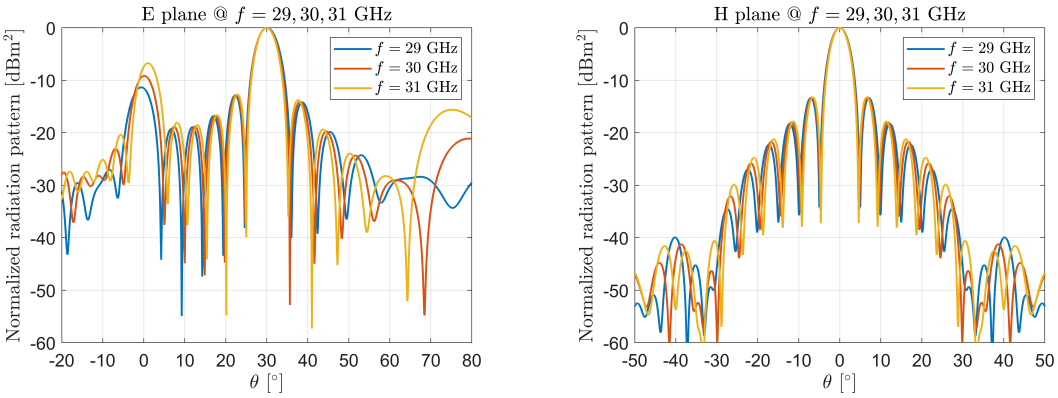

(a) E-plane of the radiation pattern.

(b) H-plane of the radiation pattern.

Figure 4.30: Radiation pattern cuts at 29, 30 and 31 GHz for the planar square patches 24 × 24 SES.

The RCS variation in the working frequency band is shown in Figure 4.31.

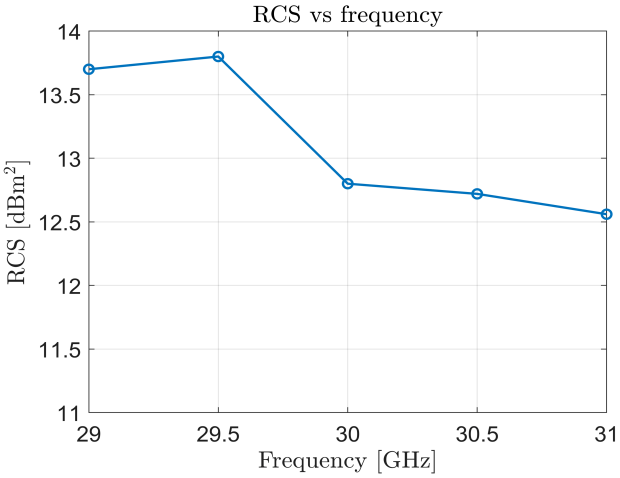

Figure 4.31: RCS versus frequency for the planar square patch 24 × 24 SES.

From the RCS versus frequency plot, depicted in Figure 4.31, it is possible to see that the RCS value is around 12.8 dBm^2 at the design frequency and, from the E and H plane plots shown in Figure 4.30, one can see that the SLL is about -9 dBm^2, at the design frequency.

4.2.2.2 Innovative unit cell SES with 24×24 elements

Using the unit cell described in Section 3.3, a 24×24 elements planar SES has been designed, with the following specifications:

- Working band: $29 - 31$ GHz (the design has been done at the central frequency of 30 GHz)
- Cell size: $\frac{\lambda}{2} = 5$ mm
- Number of elements in the x direction: $N_x = 24$
- Number of elements in the y direction: $N_y = 24$
- Aperture $D = 120$ mm
- Beam coordinates: $\theta_b = 30°$ and $\phi_b = 0°$
- Direction of arrival of the plane wave: $\theta_I = 0°$ and $\phi_I = 0°$

(for the coordinate systems refer to Section 2.6.3.1).

The required phase of each re-radiating element (evaluated with the formula in Section 4.2.1), along with the required W_{side} distribution (evaluated according to the S-curve of Figure 3.39 and referred to simply as W) and the associated error have been evaluated using *Matlab* and depicted in Figure 4.32.

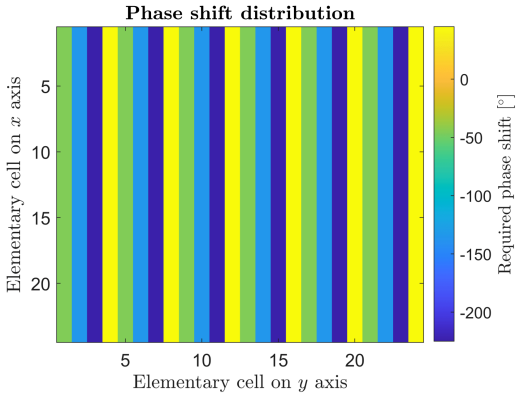

(a) Required phase distribution.

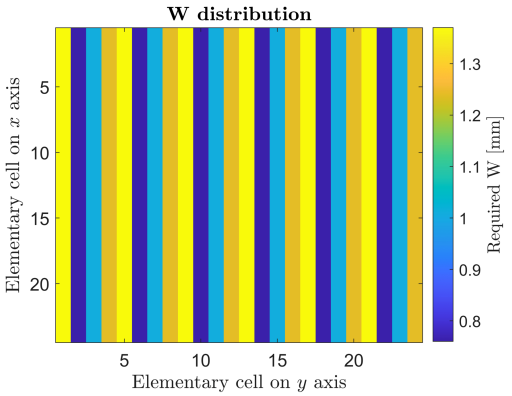

(b) Required W distribution.

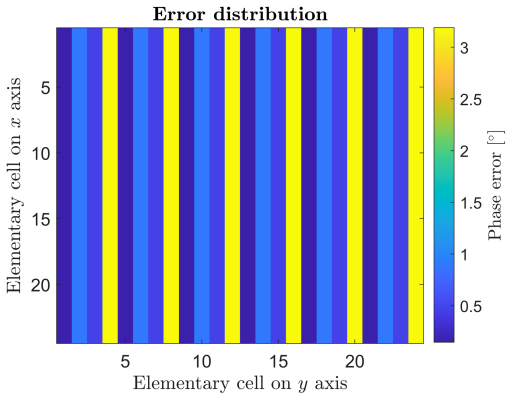

(c) Obtained phase error.

Figure 4.32: Obtained distributions for the designed planar 24×24 SES, using the innovative unit cell.

The designed structure is shown in Figure 4.33.

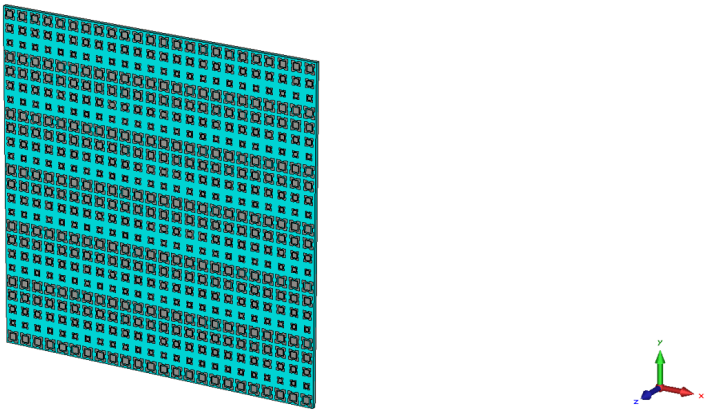

Figure 4.33: Designed planar innovative unit cell 24 × 24 SES.

By using the *CST Microwave Studio* software, a full-wave simulation of the structure has been performed, and the resulting radiation patterns at 29, 30 and 31 GHz are depicted in Figures 4.34 and 4.35.

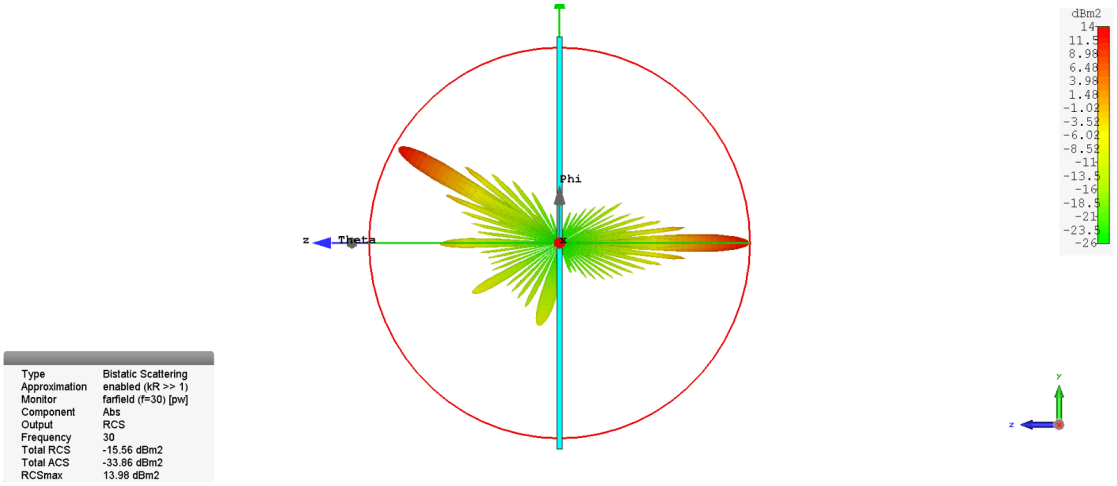

Figure 4.34: 3D radiation pattern at 30 GHz for the planar innovative unit cell 24 × 24 SES.

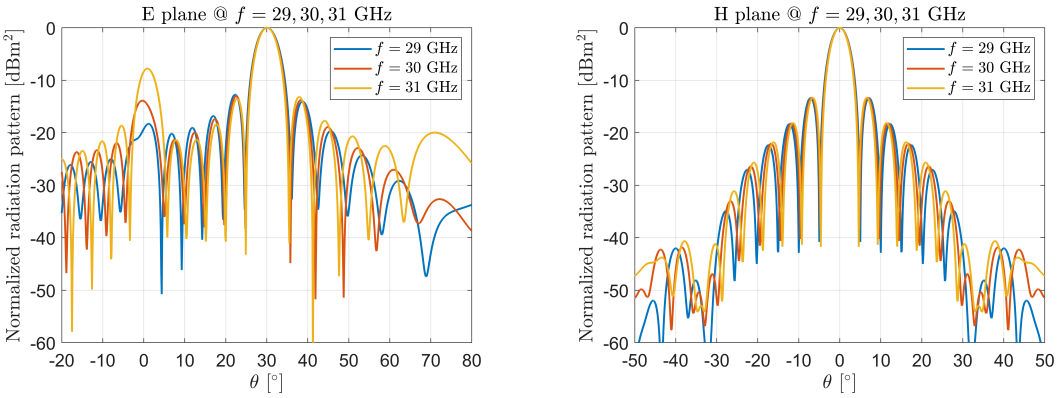

(a) E-plane of the radiation pattern.

(b) H-plane of the radiation pattern.

Figure 4.35: Radiation pattern cuts at 29, 30 and 31 GHz for the planar innovative unit cell 24 × 24 SES.

The RCS variation in the working frequency band is shown in Figure 4.36.

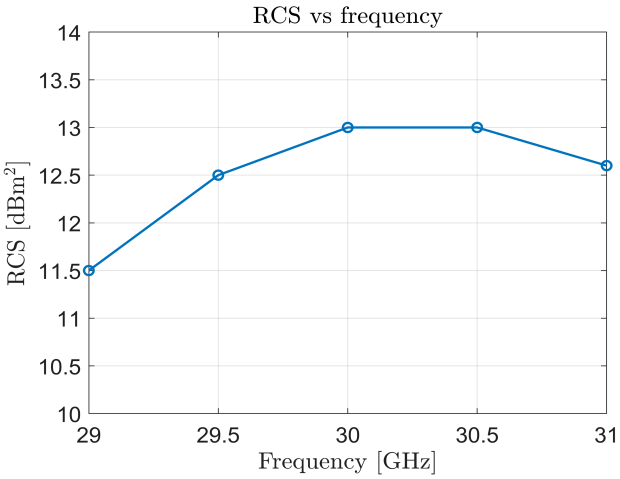

Figure 4.36: RCS versus frequency for the planar innovative unit cell 24 × 24 SES.

From the RCS versus frequency plot, depicted in Figure 4.36, it is possible to see that the RCS value is around 13 dBm^2 at the design frequency and, from the E and H plane plots shown in Figure 4.35, one can see that the SLL is about -13 dBm^2, at the design frequency.

4.2.2.3 Comparison between square patch and innovative unit cell for different incidence angles

In this part the comparison between the square patch and the innovative unit cell results will be carried out. Up to now, the S-curve that has been used for both the unit cells is the normal incidence one. Now, the incidence angle of the impinging plane wave (θ_I) is varied from 0° to 10°, 20° and 30°, while the beam angle (θ_b) is kept at 30° (it is set to 40° when the incidence angle is 30° in order to avoid specular reflection). By doing this, the appropriate S-curve for both unit cells will be considered according to the angle of incidence. For example, if the latter is set to 30°, then the S-curve obtained for an incidence angle of 30° is used. In Section 3.3.2 this analysis was explained for the innovative unit cell and it has been now performed also for the square patch unit cell.
The obtained radiation patterns comparisons for the different angles of incidence are now presented in Figures 4.37 and 4.38.

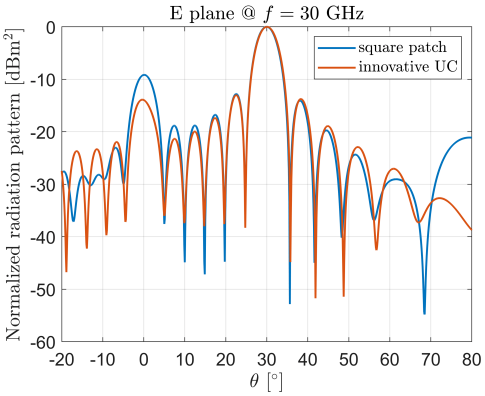

(a) E-plane of the radiation pattern, $\theta_I = 0°$.

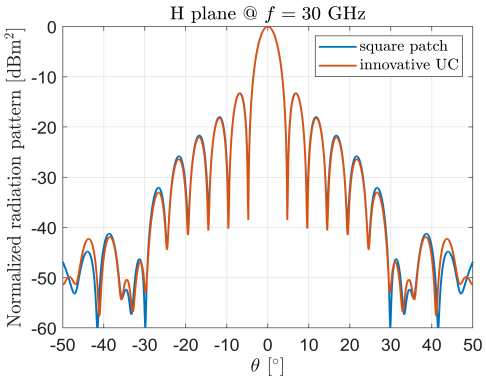

(b) H-plane of the radiation pattern, $\theta_I = 0°$.

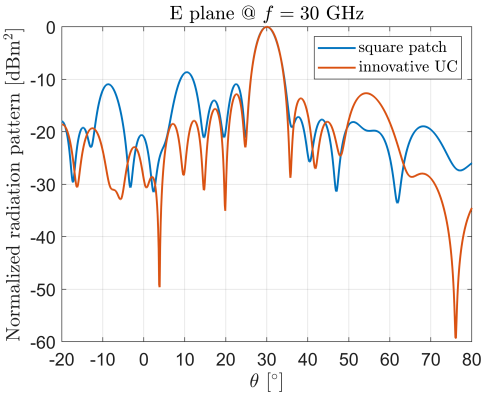

(c) E-plane of the radiation pattern, $\theta_I = 10°$.

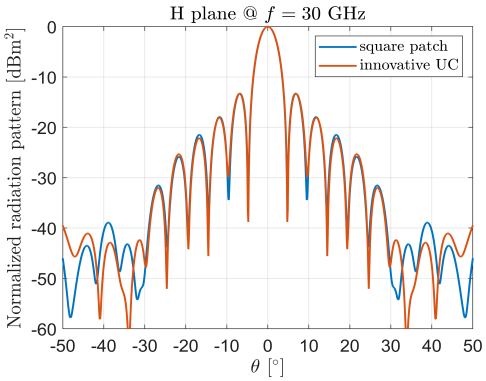

(d) H-plane of the radiation pattern, $\theta_I = 10°$.

Figure 4.37: Comparison of the radiation pattern cuts with $\theta_I = 0°$ and 10° at 30 GHz for the square patch and innovative unit cell 24 × 24 SES.

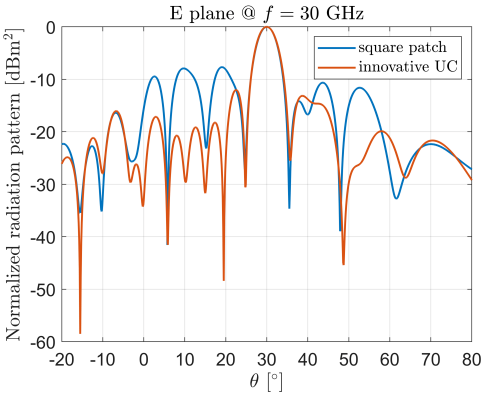

(a) E-plane of the radiation pattern, $\theta_I = 20°$.

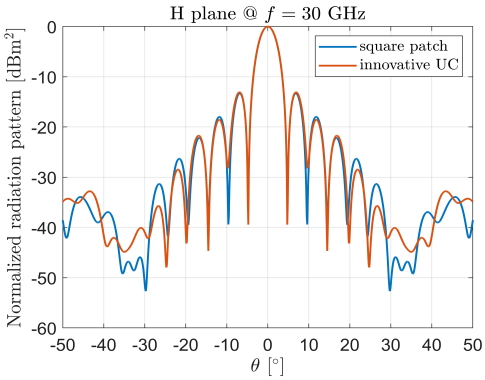

(b) H-plane of the radiation pattern, $\theta_I = 20°$.

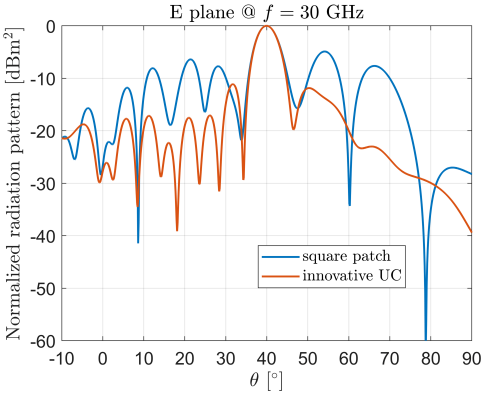

(c) E-plane of the radiation pattern, $\theta_I = 30°$.

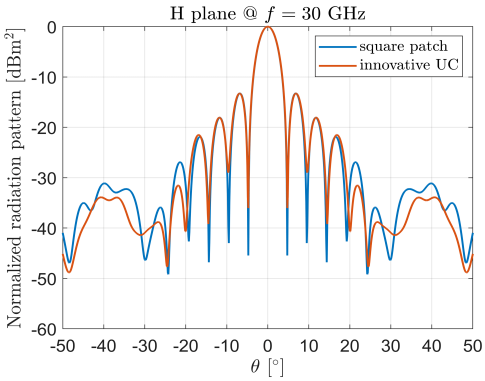

(d) H-plane of the radiation pattern, $\theta_I = 30°$.

Figure 4.38: Comparison of the radiation pattern cuts with $\theta_I = 20°$ and $30°$ at 30 GHz for the square patch and innovative unit cell 24×24 SES.

The RCS vs frequency comparisons for the different angles of incidence are presented in Figure 4.39.

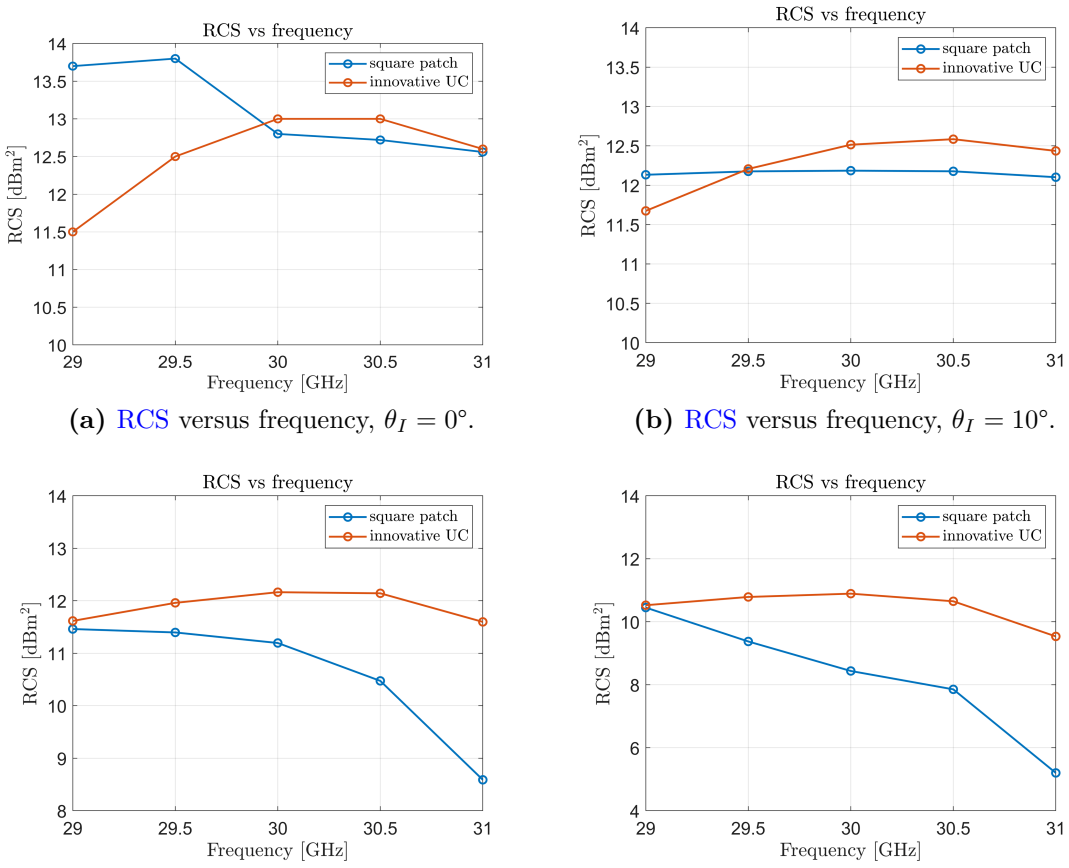

(a) RCS versus frequency, $\theta_I = 0°$.

(b) RCS versus frequency, $\theta_I = 10°$.

(c) RCS versus frequency, $\theta_I = 20°$.

(d) RCS versus frequency, $\theta_I = 30°$.

Figure 4.39: Comparison of the RCS variation with $\theta_I = 0°$, 10°, 20° and 30° in the frequency band for the square patch and innovative unit cell 24 × 24 SES.

As can be seen from the radiation patterns and the RCS comparison plots, starting from 0°, the behavior of the two unit cell is quite similar: the innovative unit cell provides little improvements with respect to the square patch one at the design frequency. By increasing the incidence angle, the innovative unit cell becomes increasingly more and more efficient with respect to the square patch configuration. By looking at Figures 4.38c and 4.38d, referring to the 30° case, one can observe a great performance improvement thanks to the use of the innovative unit cell.

Considered unit cell	$\theta_I = 0°$	$\theta_I = 10°$	$\theta_I = 20°$	$\theta_I = 30°$
Square patch	12.7	12.1	11.1	8.2
Innovative UC	13	12.5	12.1	10.9

Table 4.1: RCS [dBm^2] comparison at $f = 30$ GHz for different angles of incidence.

From Table 4.1 one can observe that the innovative unit cell provides an higher RCS value at $f = 30$ GHz with respect to the square patch unit cell at all the considered incidence angles.

4.2.3 Conformal case phase distribution

Starting from the planar case formula, shown in Equation 4.4, it is possible to arrange it for the conformal case, by adding the additional z coordinate, similarly to what has been already done in Section 2.6.2.2.

In order to get a beam in a certain direction, the phase distribution for a conformal reflectarray, with incident plane wave, can be evaluated for each element as

$$\begin{aligned}\phi_R(x_i, y_i) = k_0\{&x_i[\sin\theta_I\cos\phi_I + \sin\theta_b\cos\phi_b] + y_i[\sin\theta_I\sin\phi_I + \sin\theta_b\sin\phi_b] \\ &- z_i[\cos\theta_b + \cos\theta_I]\}\end{aligned} \tag{4.5}$$

being (θ_I, ϕ_I) the incident plane wave direction for which it is desired to deflect the field to (θ_b, ϕ_b), using the reference system of Section 2.6.3.1 with $\theta_I = \theta_f$ and $\phi_I = \phi_f$.

As an example, the required phase distribution has been evaluated using *Matlab*, for a normal incidence plane wave ($\theta_I = 0°, \phi_I = 0°$) and a 30° tilted reflected pencil beam ($\theta_b = 30°, \phi_b = 0°$) SES. The surface is a 24×24 elements conformal square patch SES with radius of curvature equal to 13λ; the required phase distribution is shown in Figure 4.40, at frequency $f = 30$ GHz and 0.5λ cell size.

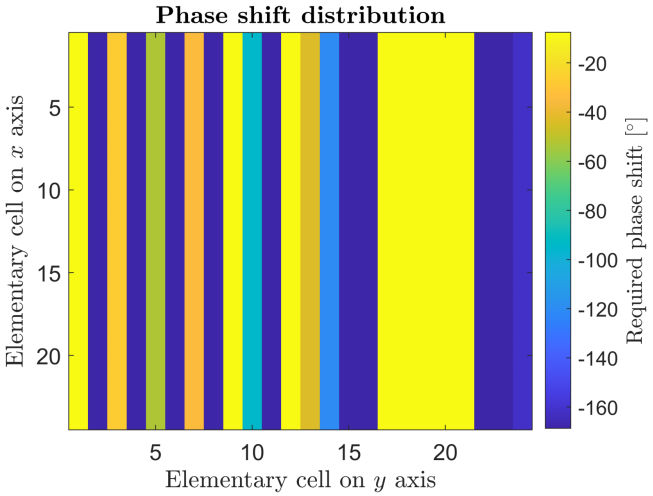

Figure 4.40: Required phase distribution for a square patch conformal 24×24 SES with incident plane wave.

4.2.4 Conformal SES square patch and innovative unit cell comparison

4.2.4.1 Square patch SES with 24×24 elements

Using the square patch unit cell, a 24×24 elements CRA has been designed, with the following specifications:

- Working band: $29 - 31$ GHz (the design has been done at the central frequency of 30 GHz)
- Cell size: $\frac{\lambda}{2} = 5$ mm
- Number of elements in the x direction: $N_x = 24$
- Number of elements in the y direction: $N_y = 24$
- Aperture $D = 120$ mm
- Radius of curvature: $R = 13\lambda$
- Beam coordinates: $\theta_b = 30°$ and $\phi_b = 0°$
- Direction of arrival of the plane wave: $\theta_I = 0°$ and $\phi_I = 0°$

(for the coordinate systems refer to Section 2.6.3.1).

The required phase of each re-radiating element (evaluated with the formula in Section 4.2.3), along with the required W distribution and the associated error, have been evaluated using *Matlab* and depicted in Figure 4.41.

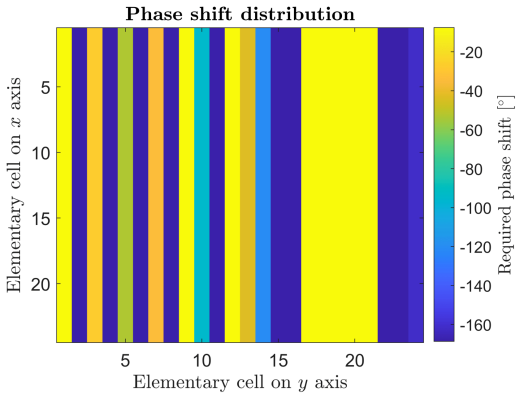

(a) Required phase distribution.

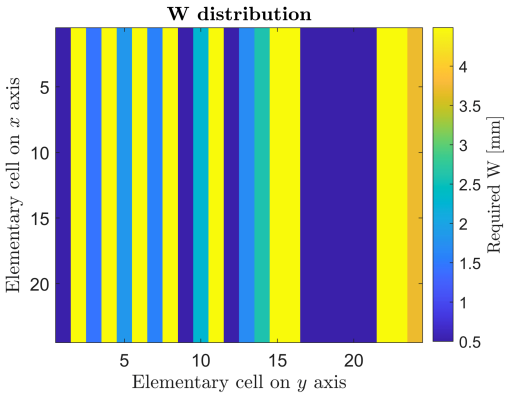

(b) Required W distribution.

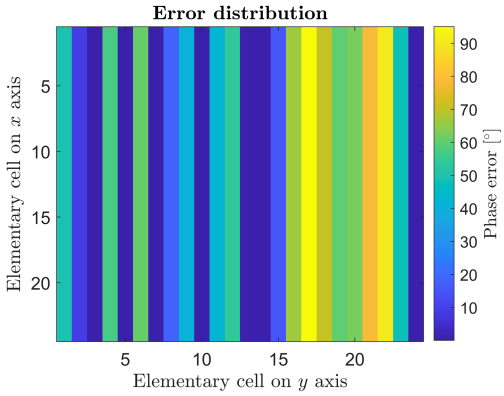

(c) Obtained phase error.

Figure 4.41: Obtained distributions for the designed conformal square patch 24×24 SES.

The designed structure is shown in Figure 4.42.

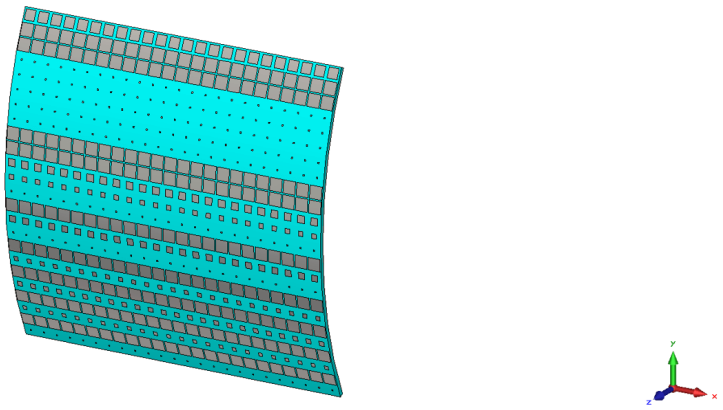

Figure 4.42: Designed conformal square patches 24 × 24 SES.

By using the *CST Microwave Studio* software, a full-wave simulation of the structure has been performed, and the resulting radiation patterns at 29, 30 and 31 GHz are depicted in Figures 4.43 and 4.44.

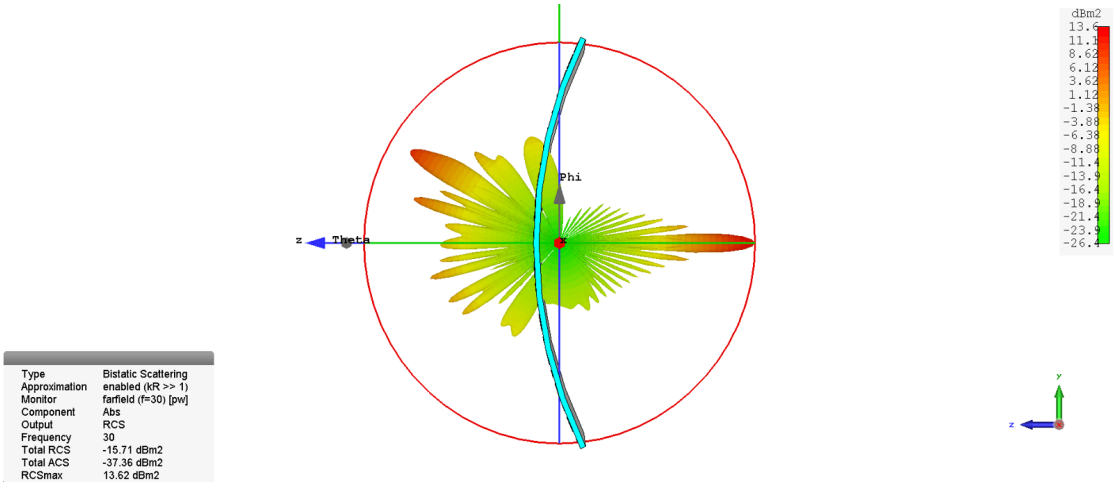

Figure 4.43: 3D radiation pattern at 30 GHz for the conformal square patches 24 × 24 SES.

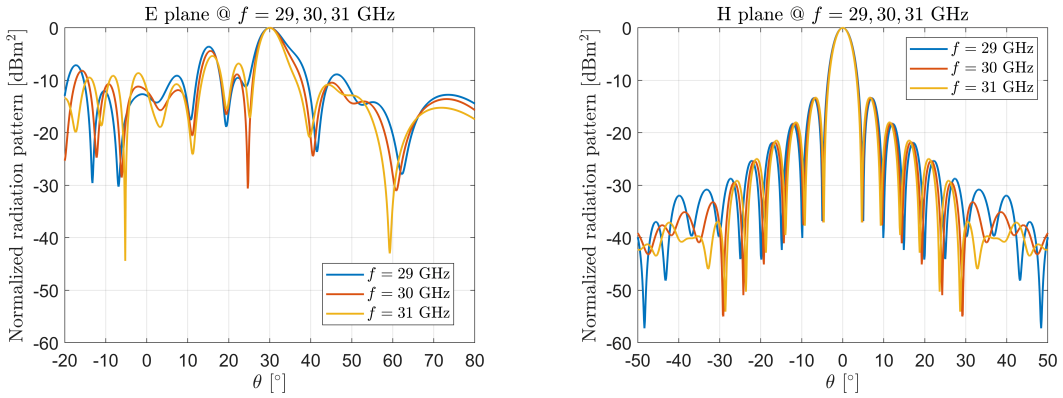

(a) E-plane of the radiation pattern.

(b) H-plane of the radiation pattern.

Figure 4.44: Radiation pattern cuts at 29, 30 and 31 GHz for the conformal square patches 24 × 24 SES.

The RCS variation in the working frequency band is shown in Figure 4.45.

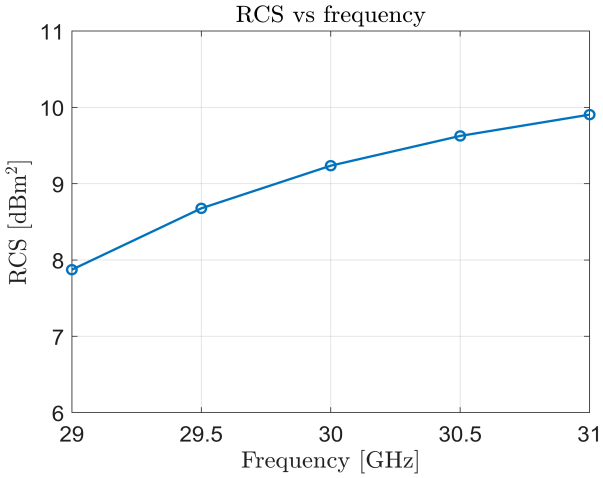

Figure 4.45: RCS versus frequency for the conformal square patch 24 × 24 SES.

From the RCS versus frequency plot, depicted in Figure 4.45, it is possible to see that the RCS value is around 9.2 dBm^2 at the design frequency and, from the E and H plane plots shown in Figure 4.44, one can see that the SLL is about -4 dBm^2, at the design frequency. Due to relatively small radius of curvature of the surface, it is possible to observe a degradation in performance with respect to the planar case of Section 4.2.2.1: this is predictable due to the different surface geometry.

4.2.4.2 Innovative unit cell SES with 24×24 elements

Using the innovative unit cell, a 24×24 elements conformal SES has been designed, with the following specifications:

- Working band: $29 - 31$ GHz (the design has been done at the central frequency of 30 GHz)
- Cell size: $\frac{\lambda}{2} = 5$ mm
- Number of elements in the x direction: $N_x = 24$
- Number of elements in the y direction: $N_y = 24$
- Aperture $D = 120$ mm
- Radius of curvature: $R = 13\lambda$
- Beam coordinates: $\theta_b = 30°$ and $\phi_b = 0°$
- Direction of arrival of the plane wave: $\theta_I = 0°$ and $\phi_I = 0°$

(for the coordinate systems refer to Section 2.6.3.1).

The required phase of each re-radiating element (evaluated with the formula in Section 4.2.3), along with the required W distribution and the associated error have been evaluated using *Matlab* and depicted in Figure 4.46.

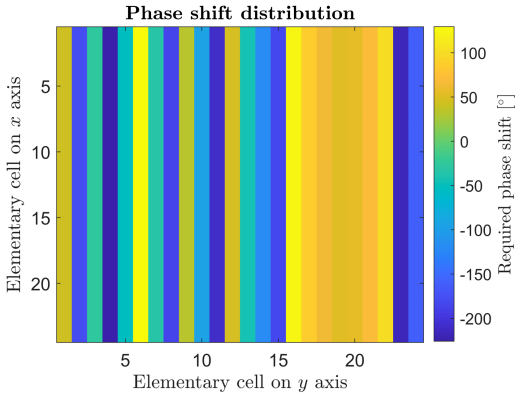

(a) Required phase distribution.

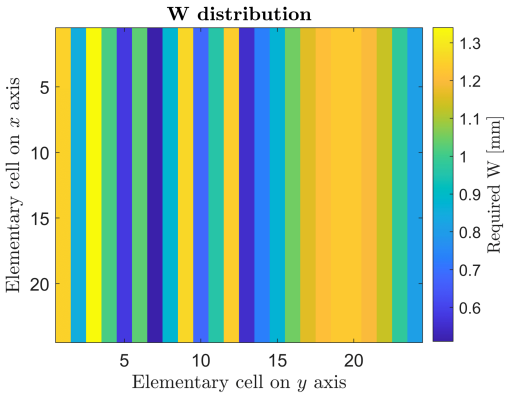

(b) Required W distribution.

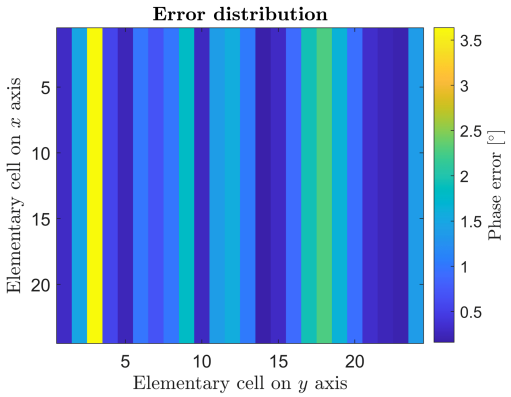

(c) Obtained phase error.

Figure 4.46: Obtained distributions for the designed conformal 24×24 SES, using the innovative unit cell.

The designed structure is shown in Figure 4.47.

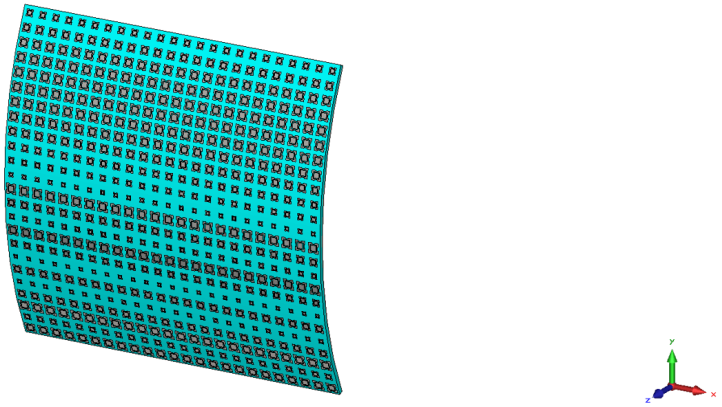

Figure 4.47: Designed conformal innovative unit cell 24 × 24 SES.

By using the *CST Microwave Studio* software, a full-wave simulation of the structure has been performed, and the resulting radiation patterns at 29, 30 and 31 GHz are depicted in Figures 4.48 and 4.49.

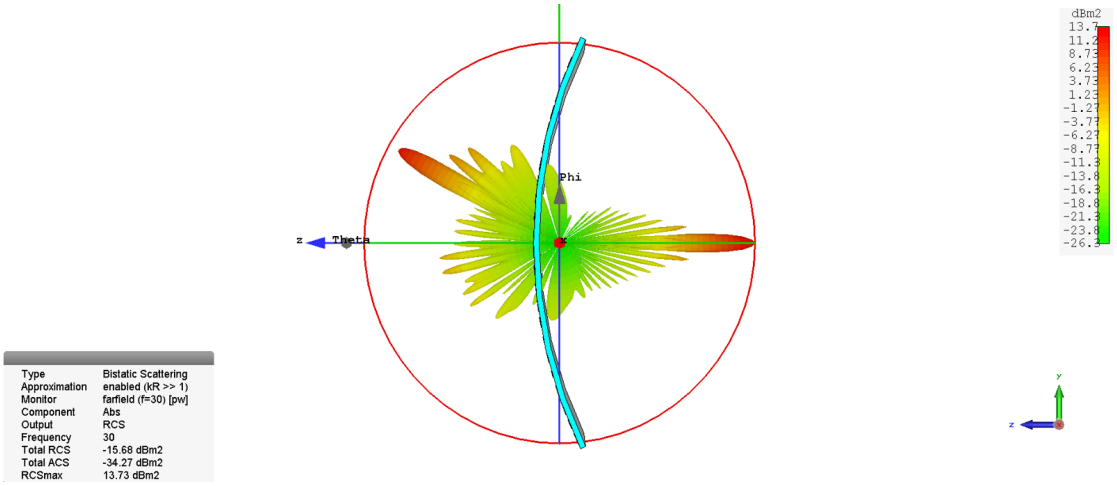

Figure 4.48: 3D radiation pattern at 30 GHz for the conformal innovative unit cell 24 × 24 SES.

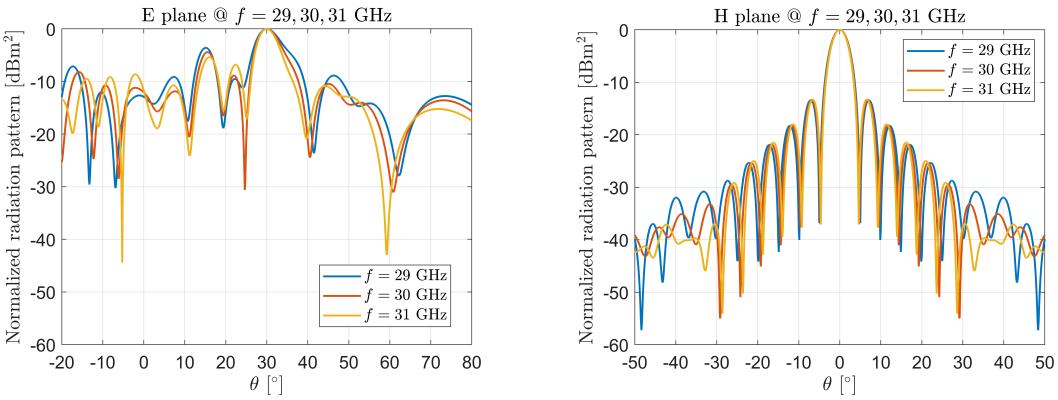

(a) E-plane of the radiation pattern.

(b) H-plane of the radiation pattern.

Figure 4.49: Radiation pattern cuts at 29, 30 and 31 GHz for the conformal innovative unit cell 24 × 24 SES.

The RCS variation in the working frequency band is shown in Figure 4.50.

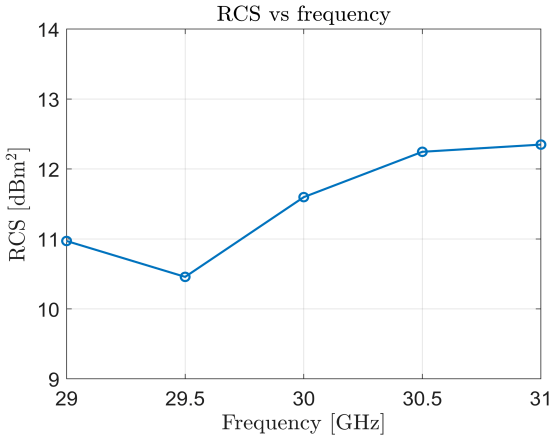

Figure 4.50: RCS versus frequency for the conformal innovative unit cell 24 × 24 SES.

From the RCS versus frequency plot, depicted in Figure 4.50, it is possible to see that the RCS value is around 11.6 dBm^2 at the design frequency and, from the E and H plane plots shown in Figure 4.49, one can see that the SLL is about -9 dBm^2, at the design frequency. Beside the degradation in performance with respect to the planar case mentioned in Section 4.2.2.2, a comparison with the square patch configuration has been done and the results are presented in the next Section.

4.2.4.3 Comparison between square patch and innovative unit cell for normal incidence

In this part the comparison between the square patch and the innovative unit cell CRAs results will be carried out for the normal incidence case.
The obtained comparison results for normal incidence are now presented in Figures 4.51 and 4.52, where the RCS and radiation patterns comparisons are depicted, respectively.

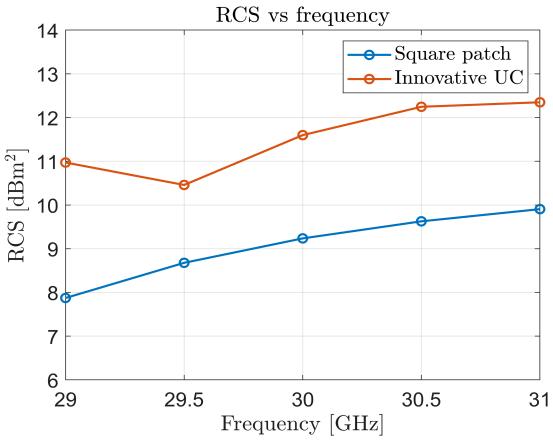

Figure 4.51: RCS versus frequency, comparison between the conformal square patch and innovative unit cell 24 × 24 CRA

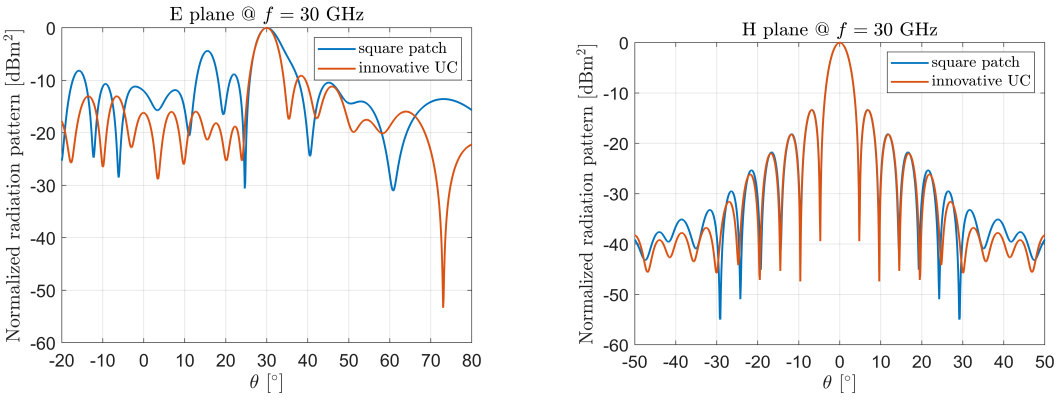

(a) E-plane of the radiation pattern, $\theta_I = 0°$. **(b)** H-plane of the radiation pattern, $\theta_I = 0°$.

Figure 4.52: Comparison of the radiation pattern cuts with $\theta_I = 0°$ at 30 GHz for the square patch and innovative unit cell 24 × 24 CRA

From the RCS and radiation pattern comparison plots, it is possible to observe an improvement in the performance of the innovative unit cell CRA with respect to the square patch one, e.g. the higher RCS value at all the frequencies in the working band and also in the SLL. In particular, looking at Table 4.2, the innovative unit cell configuration gives an almost 3 dBm^2 higher RCS value with respect to the square patch one at the design frequency.

Considered unit cell	RCS [dBm^2]	SLL [dBm^2]
Square patch	9.1	-4.4
Innovative UC	11.6	-9.1

Table 4.2: Performance comparison of the SESs at $f = 30$ GHz.

Once this is established, from now on, the square patch unit cell will no more be compared to the innovative one; further improvements will be developed for the latter in order to enhance, even more, its capabilities.

4.2.5 Innovative unit cell surface design improvements

By using the same configuration of Section 4.2.4.2, other methods have been employed for the SES design, exploiting more sophisticated techniques for calculating the phase of the various elements on the surface. Up to now, the normal incidence S-curve has been used for the design of the conformal SES, but it is not the most suitable method for this use. In the following, a brief description of two different methods will be given, along with the obtained results for all the plane wave incidence angles; a final comparison is then presented, in order to highlight pros and cons of each method.

4.2.5.1 Use of appropriate AOI S-curve for each patch element

This method (called for brevity *opt. AOI*) involves using the most appropriate unit cell S-curve (refer to Section 3.3.2) based on the angle formed between each cell and the incident plane wave; it is similar to what has been done for the planar case, but here the incidence angle is not unique for the entire surface, but it is different for each cell. Actually, due to the plane wave incidence, the angle will be the same for each cell *column* of the surface, as shown in the following.

As an example, the angle of incidence distribution for the entire surface is depicted in Figure 4.53, with plane wave incidence coordinates equal to $\theta_I = 10°$, $\phi_I = 0°$ and beam coordinates $\theta_b = 30°$, $\phi_b = 0°$.

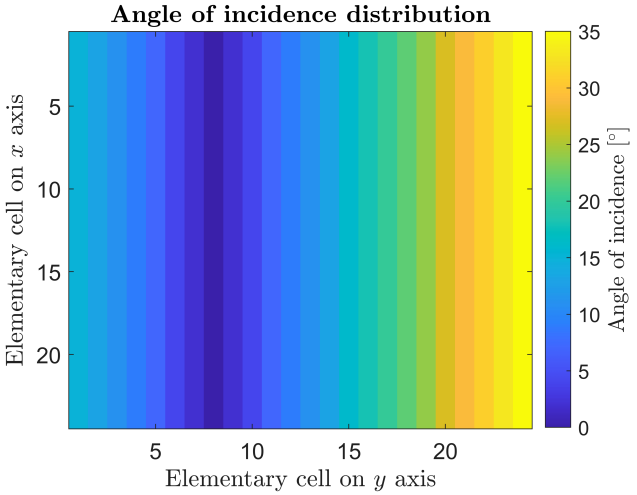

Figure 4.53: Angle of incidence distribution for a 24×24 SES, $\theta_I = 10°$.

For the sake of simplicity, the comparison between this method and the normal incidence one, are now presented, for each incidence angle.

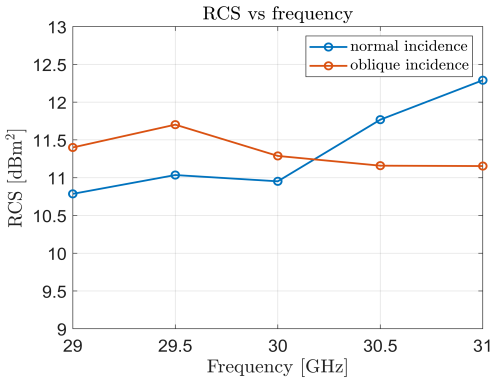

(a) RCS versus frequency, $\theta_I = 10°$.

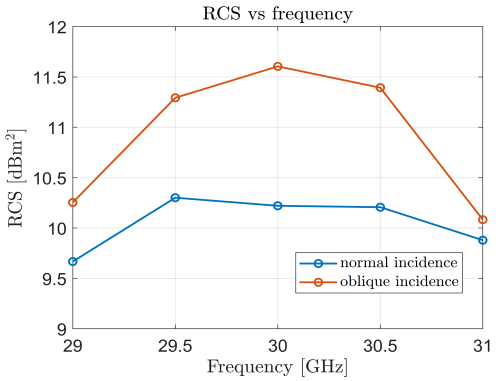

(b) RCS versus frequency, $\theta_I = 20°$.

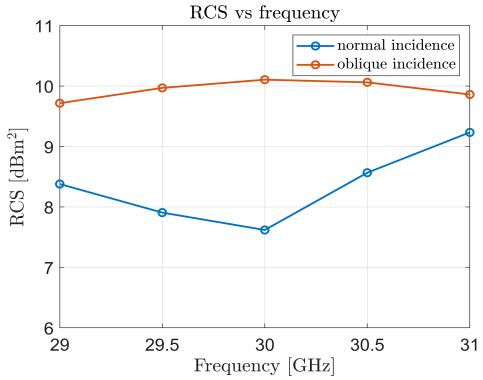

(c) RCS versus frequency, $\theta_I = 30°$.

Figure 4.54: Comparison of the RCS variation with $\theta_I = 10°$, 20° and 30° in the frequency band for the innovative unit cell normal incidence and *opt. AOI* method SESs.

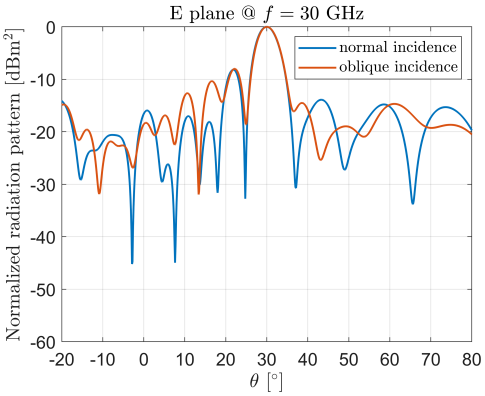

(a) E-plane of the radiation pattern, $\theta_I = 10°$.

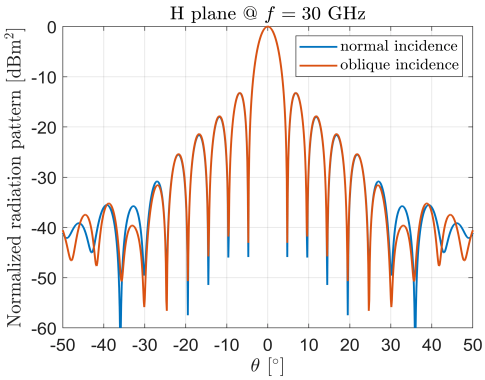

(b) H-plane of the radiation pattern, $\theta_I = 10°$.

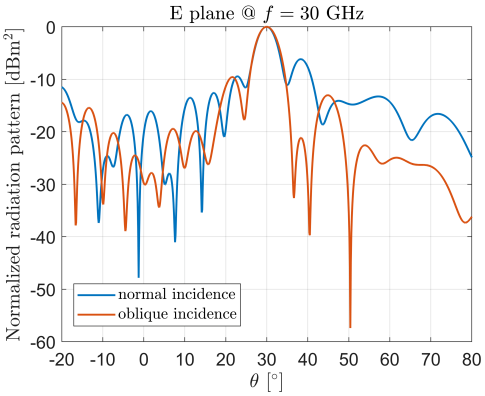

(c) E-plane of the radiation pattern, $\theta_I = 20°$.

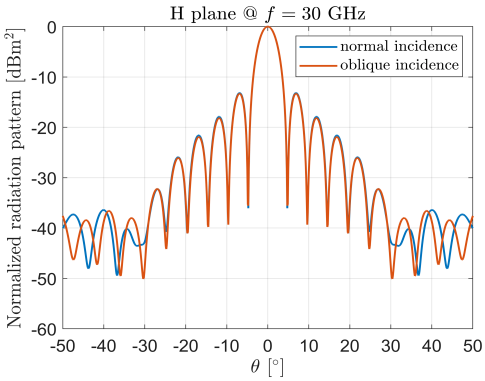

(d) H-plane of the radiation pattern, $\theta_I = 20°$.

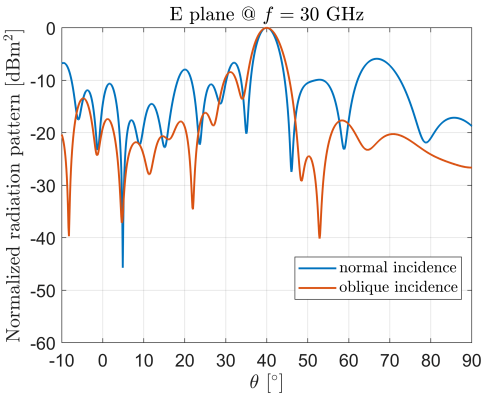

(e) E-plane of the radiation pattern, $\theta_I = 30°$.

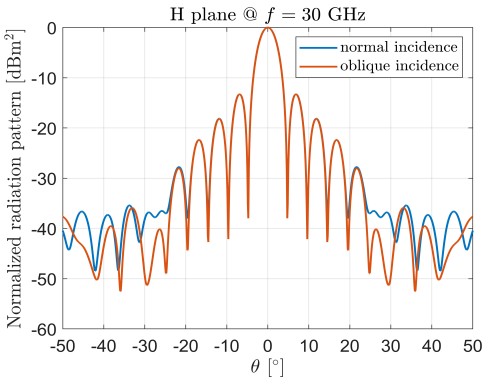

(f) H-plane of the radiation pattern, $\theta_I = 30°$.

Figure 4.55: Comparison of the radiation pattern cuts with $\theta_I = 10°$, 20° and 30° at 30 GHz for the innovative unit cell normal incidence and *opt. AOI* method SESs.

From the plots in Figures 4.54 and 4.55, it is possible to observe the increase in the maximum RCS value (at the design frequency) and, also, the improved SLL using the new technique with respect to the normal incidence one.

4.2.5.2 Use of a single AOI S-curve for each patch element

Another method, called for brevity *opt. 1 AOI*, is similar to what has been done for the planar case: a single AOI S-curve is used for the design of the entire SES. For example, if the plane wave incidence angle is set to 10°, then the 10° S-curve is used for the patch elements design of the entire surface.

A comparison of the RCS versus frequency behavior for the normal incidence, *opt. AOI* and *opt. 1 AOI* method is depicted in Figure 4.56.

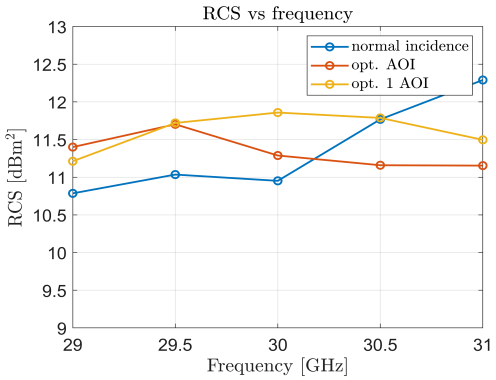

(a) RCS versus frequency, $\theta_I = 10°$.

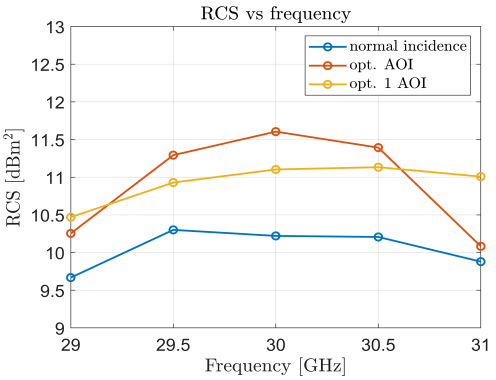

(b) RCS versus frequency, $\theta_I = 20°$.

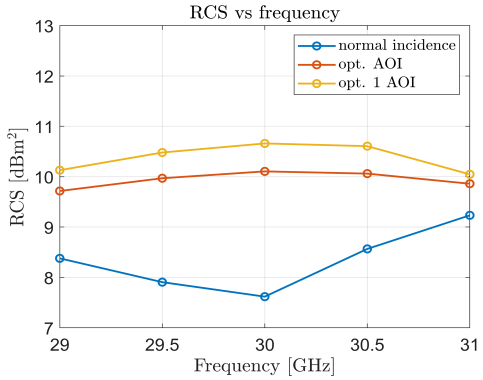

(c) RCS versus frequency, $\theta_I = 30°$.

Figure 4.56: Comparison of the RCS variation with $\theta_I = 10°$, 20° and 30° in the frequency band for the innovative unit cell normal incidence, *opt. AOI* and *opt. 1 AOI* method SESs.

As can be seen from the RCS comparison, the *opt. AOI* method allows to get an higher RCS value at $\theta_I = 20°$, but its variation in the frequency band is quite large. The *opt. 1 AOI* method, instead, reaches a lower RCS value at the central frequency at an incidence angle of 20°, but in all the other cases produces a flatter RCS variation and reaches higher RCS value at 30 GHz.

Since the improved performance of the *opt. AOI* method have been already demonstrated with respect to the normal incidence case, a comparison between this new method and the *opt. AOI* one is now presented, for each incidence angle.

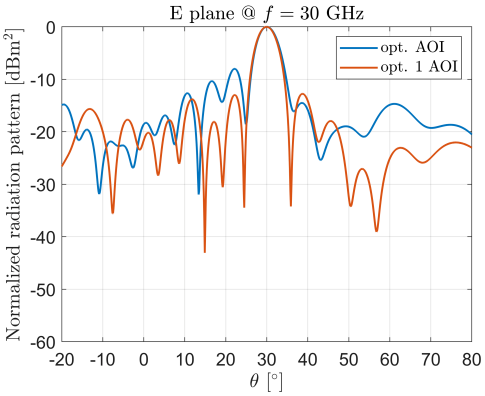

(a) E-plane of the radiation pattern, $\theta_I = 10°$.

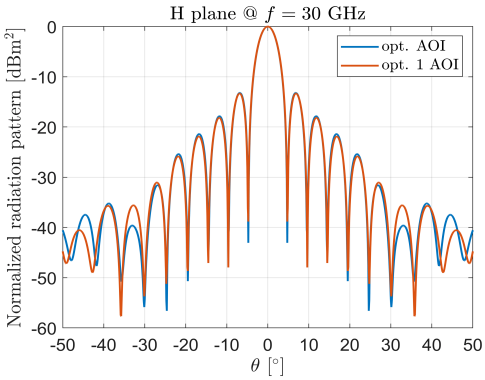

(b) H-plane of the radiation pattern, $\theta_I = 10°$.

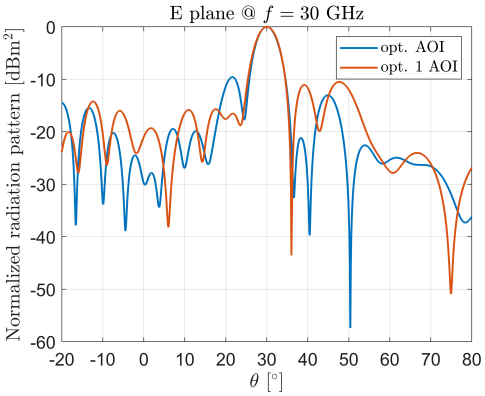

(c) E-plane of the radiation pattern, $\theta_I = 20°$.

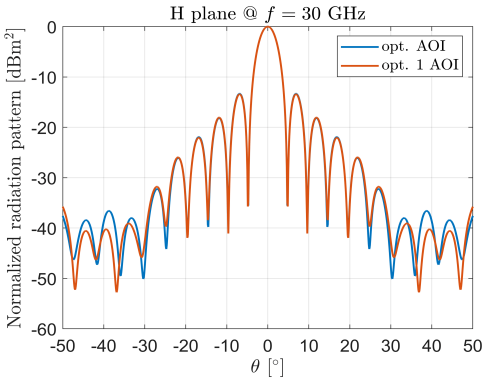

(d) H-plane of the radiation pattern, $\theta_I = 20°$.

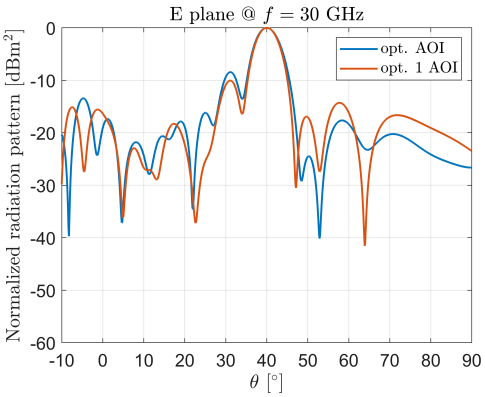

(e) E-plane of the radiation pattern, $\theta_I = 30°$.

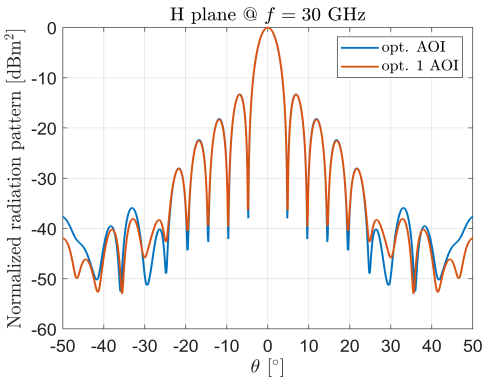

(f) H-plane of the radiation pattern, $\theta_I = 30°$.

Figure 4.57: Comparison of the radiation pattern cuts with $\theta_I = 10°$, 20° and 30° at 30 GHz for the innovative unit cell *opt. AOI* and *opt. 1 AOI* method SESs.

By looking at Figure 4.57, it is possible to observe the behavior of the two

methods from the radiation patterns point of view. It may seems to be counter-intuitive that the *opt. AOI* method provides worse capabilities than this new one. The latter, in fact, evaluates the patch size distribution according to a single S-curve, that depends on the plane wave incidence angle, but fixed for each cell. Since the surface is conformal, one may expect that evaluating the appropriate patch size using a different S-curve for each single cell, i.e. using the *opt. AOI* method, could be more "precise" than this new one. However, this is not true and a reason is the behavior of the AOI curves shown in Section 3.3.2 which are not as smooth as required, especially for higher AOI. This, in fact, deteriorates the performance of the designed SES and allows the *opt. 1 AOI* method to be more efficient, thanks to the use of a single S-curve for all the elements.

4.2.6 Innovative unit cell surface practical designs

In this part, some practical designs have been carried out for the smart electromagnetic surface realization. As already mentioned at the beginning of this Chapter, the goal of this work is to design a SES that can be employed and integrated in the urban environment, for example on public lighting poles and, consequently, a curved shape is necessary. This is why, starting from a planar configuration, several conformal designs will be presented, along with an analysis of their performance.

4.2.6.1 Planar 68×36 elements

Starting from the planar case, the innovative unit cell has been used to design a 68×36 elements planar SES, with the following specifications:

- Working band: $29 - 31$ GHz (the design has been done at the central frequency of 30 GHz)
- Cell size: $\frac{\lambda}{2} = 5$ mm
- Number of elements in the x direction: $N_x = 68$
- Number of elements in the y direction: $N_y = 36$
- Aperture along x direction: $D_x = 340$ mm

- Aperture along y direction: $D_y = 180$ mm
- Beam coordinates: $\theta_b = 30°$ and $\phi_b = 0°$
- Direction of arrival of the plane wave: $\theta_I = 15°$ and $\phi_I = 0°$

(for the coordinate systems refer to Section 2.6.3.1).

The required phase of each re-radiating element, along with the required W distribution and the associated error have been evaluated using *Matlab* and depicted in Figure 4.58. The design has been done by using the proper S-curve, according to the angle of incidence of the impinging plane wave, which is 15° in this case.

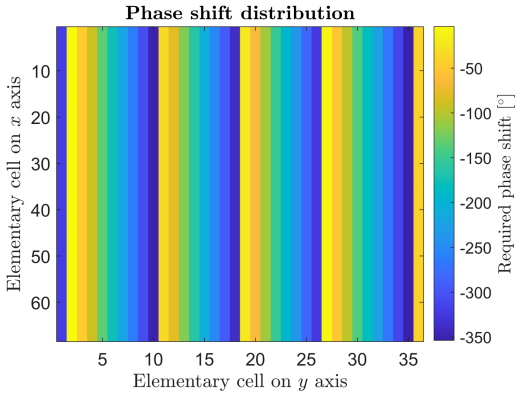

(a) Required phase distribution.

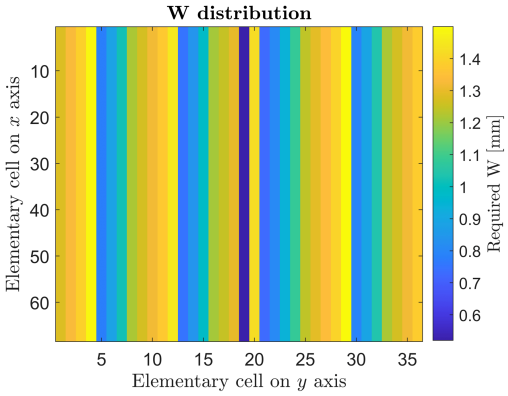

(b) Required W distribution.

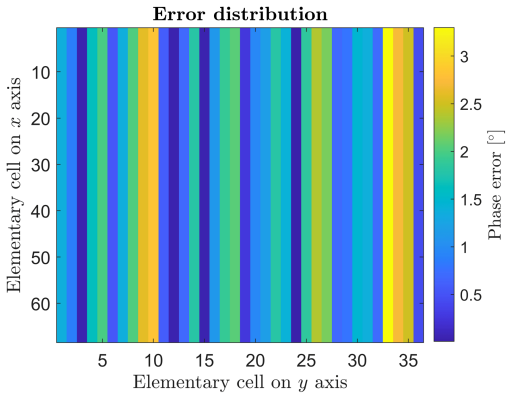

(c) Obtained phase error.

Figure 4.58: Obtained distributions for the designed planar 68×36 SES, using the innovative unit cell.

The designed structure is shown in Figure 4.59.

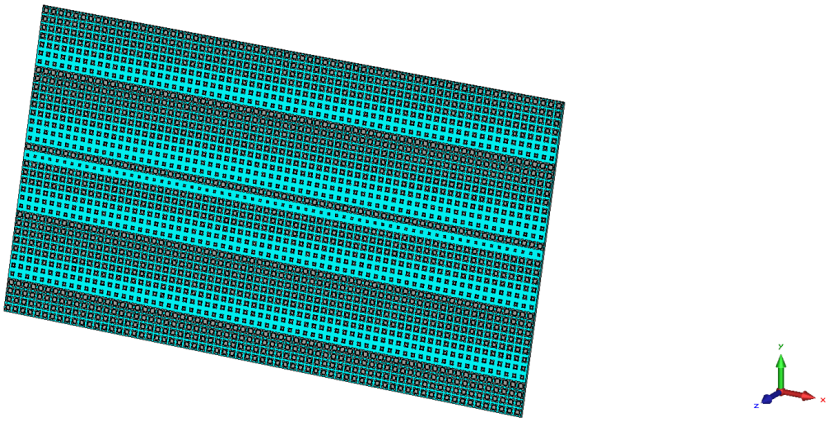

Figure 4.59: Designed planar innovative unit cell 68 × 36 SES.

By using the *CST Microwave Studio* software, a full-wave simulation of the structure has been performed, and the resulting radiation patterns at 29, 30 and 31 GHz are depicted in Figures 4.60 and 4.61.

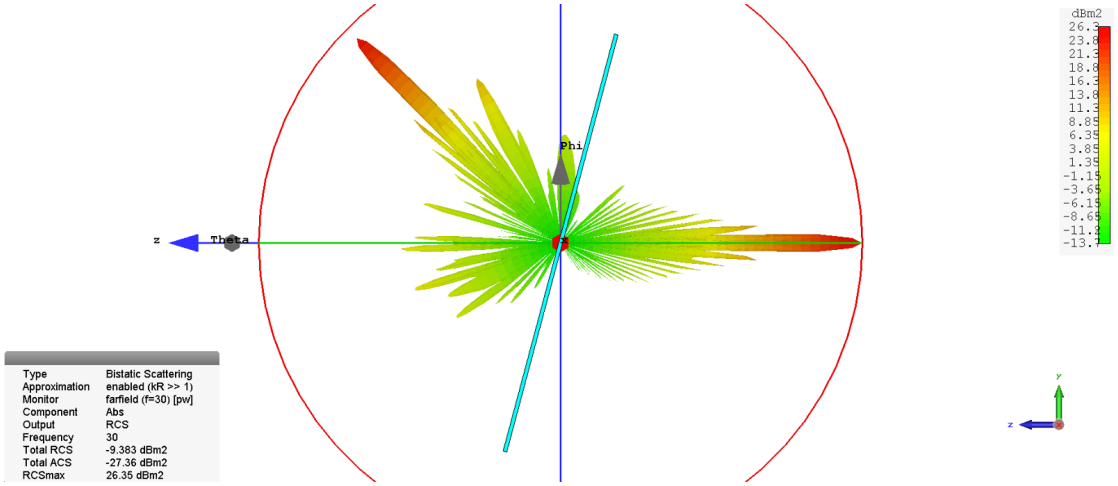

Figure 4.60: 3D radiation pattern at 30 GHz for the planar innovative unit cell 68 × 36 SES.

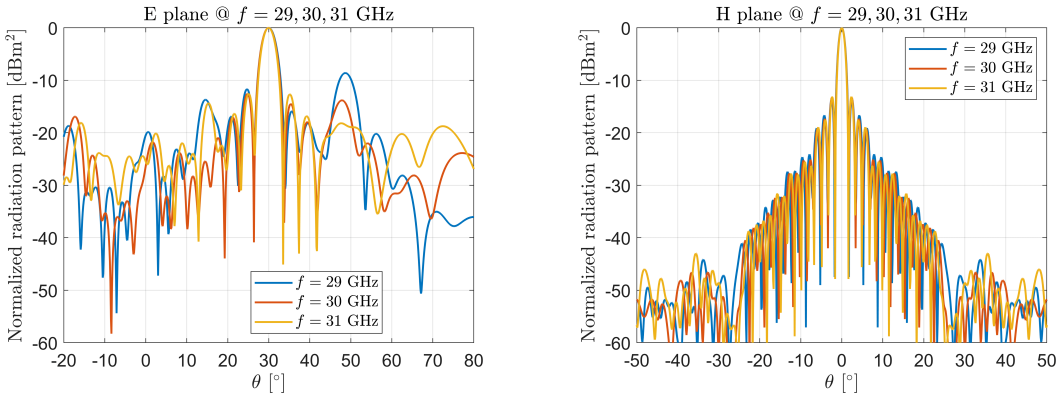

(a) E-plane of the radiation pattern.

(b) H-plane of the radiation pattern.

Figure 4.61: Radiation pattern cuts at 29, 30 and 31 GHz for the planar innovative unit cell 68 × 36 SES.

The RCS variation in the working frequency band is shown in Figure 4.62.

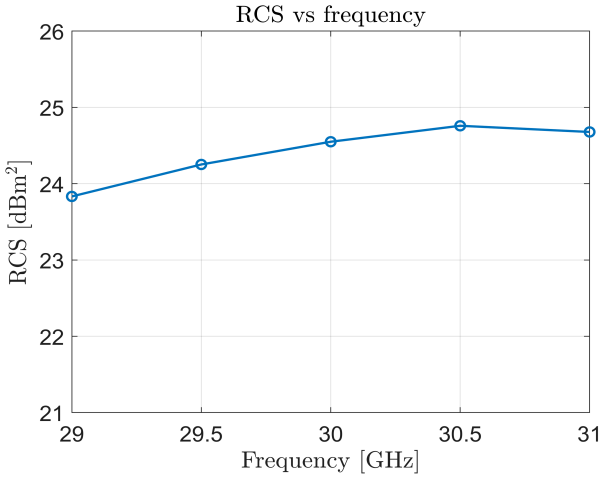

Figure 4.62: RCS versus frequency for the planar innovative unit cell 68 × 36 SES.

From the RCS versus frequency plot, depicted in Figure 4.62, it is possible to see that the RCS value is around 24.5 dBm^2 at the design frequency and, from the E and H plane plots shown in Figure 4.61, one can see that the SLL is about -12 dBm^2, at the design frequency. By comparing these results with the planar 24 × 24 configuration in Section 4.2.2.2, it is possible to observe the substantial increase in

the maximum RCS value due to the larger aperture of this last surface.

4.2.6.2 Conformal 68×60 elements

For the conformal configuration, some techniques were previously mentioned in the last designs. At this stage, only the best method among them will be presented, that is the one that provides better performance. In this case the best method is the so called *opt. 1 AOI*, which involves using a single angle of incidence S-curve for the entire surface.

Using the innovative unit cell, a 68×60 elements conformal SES has been designed, with the following specifications:

- Working band: $29-31$ GHz (the design has been done at the central frequency of 30 GHz)
- Cell size: $\frac{\lambda}{2} = 5$ mm
- Number of elements in the x direction: $N_x = 68$
- Number of elements in the y direction: $N_y = 60$
- Aperture along x direction: $D_x = 340$ mm
- Aperture along y direction: $D_y = 300$ mm
- Radius of curvature: $R = 17.6\lambda$
- Beam coordinates: $\theta_b = 30°$ and $\phi_b = 0°$
- Direction of arrival of the plane wave: $\theta_I = 15°$ and $\phi_I = 0°$

(for the coordinate systems refer to Section 2.6.3.1).

The curvature radius of 17.6λ has been selected based on the typical dimensions of the public lighting poles.

The required phase of each re-radiating element, along with the required W distribution and the associated error have been evaluated using *Matlab* and depicted in Figure 4.63.

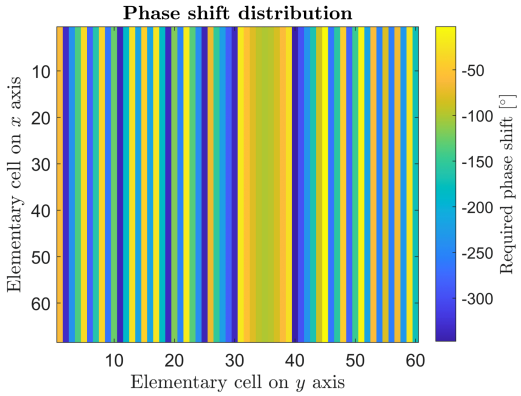

(a) Required phase distribution.

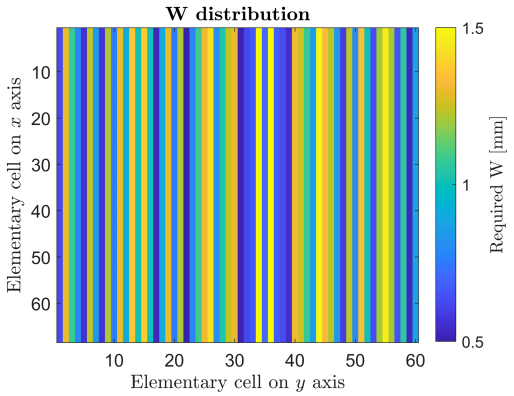

(b) Required W distribution.

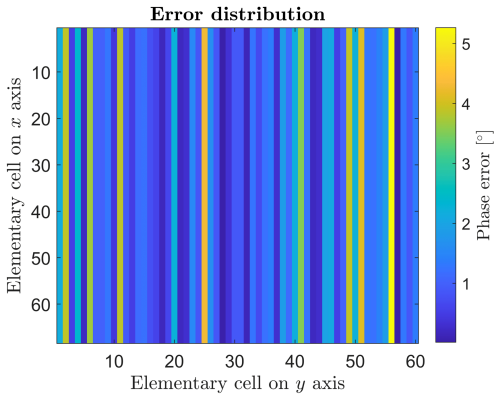

(c) Obtained phase error.

Figure 4.63: Obtained distributions for the designed conformal 68×60 SES, using the innovative unit cell.

The designed structure is shown in Figure 4.64.

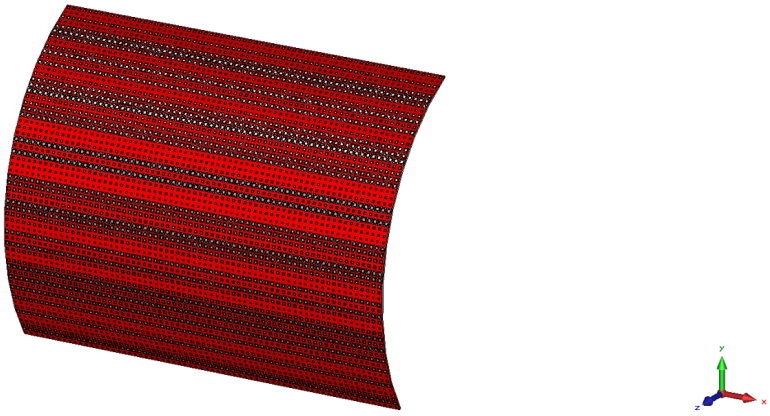

Figure 4.64: Designed conformal innovative unit cell 68 × 60 SES.

By using the *CST Microwave Studio* software, a full-wave simulation of the structure has been performed, and the resulting radiation patterns at 29, 30 and 31 GHz are depicted in Figures 4.65 and 4.66.

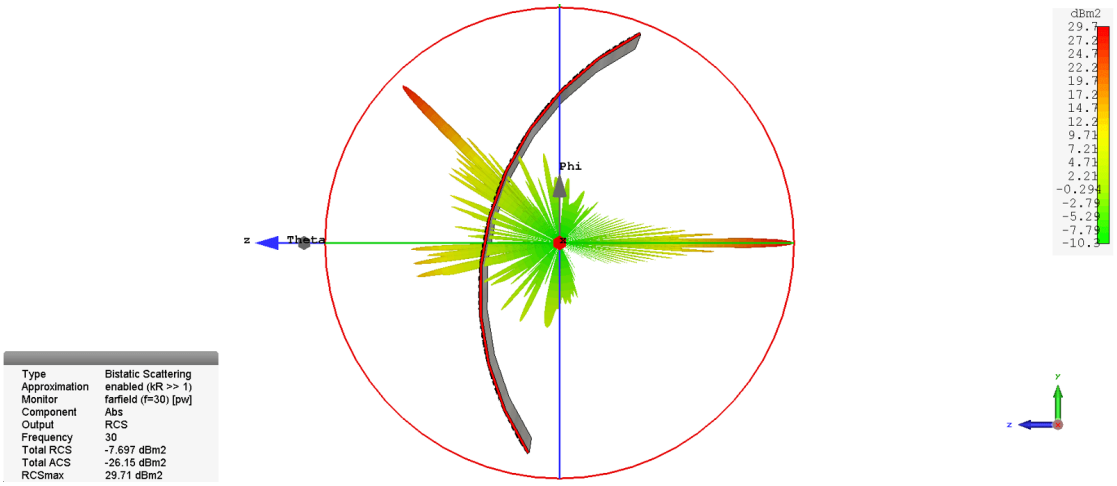

Figure 4.65: 3D radiation pattern at 30 GHz for the conformal innovative unit cell 68 × 60 SES.

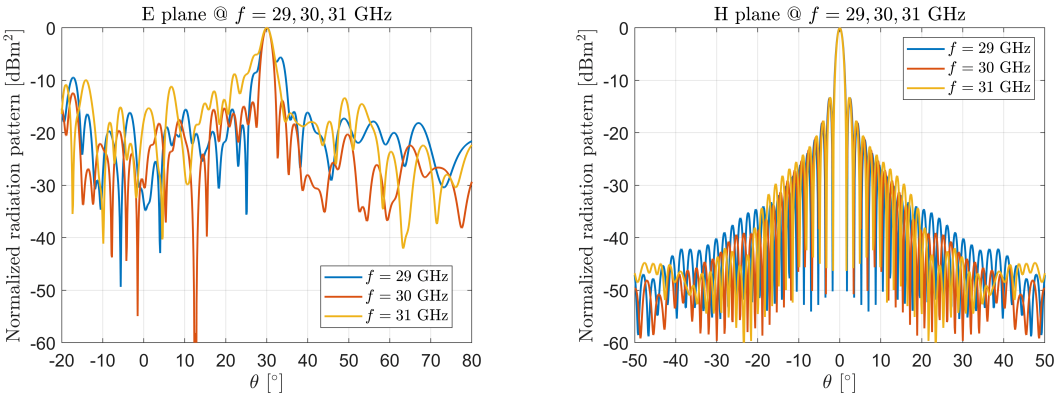

(a) E-plane of the radiation pattern.

(b) H-plane of the radiation pattern.

Figure 4.66: Radiation pattern cuts at 29, 30 and 31 GHz for the conformal innovative unit cell 68 × 60 SES.

The RCS variation in the working frequency band is shown in Figure 4.67.

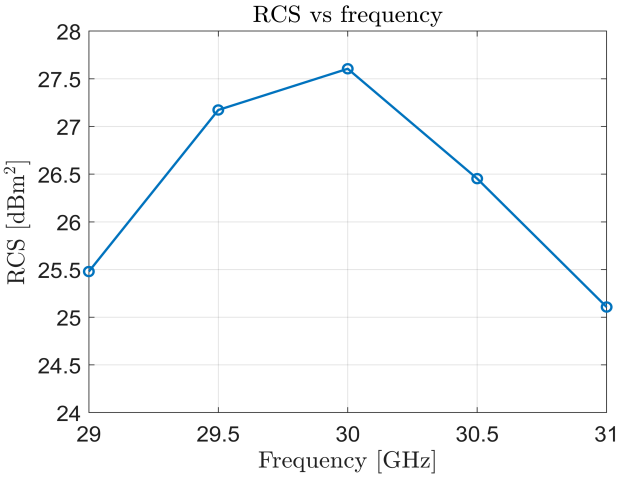

Figure 4.67: RCS versus frequency for the conformal innovative unit cell 68 × 60 SES.

From the RCS versus frequency plot, depicted in Figure 4.67, it is possible to see that the RCS value is approximately 27.6 dBm^2 at the design frequency. Moreover, from the E and H plane plots shown in Figure 4.66, it can be observed that the SLL is about -14 dBm^2, at the design frequency. Intuitively, one would expect the latter to be worse compared to the planar case, but here it is better: this improvement is

attributed to the increased antenna aperture in this conformal configuration.

An RCS comparison plot with the normal incidence method is illustrated in Figure 4.68. It is noticeable that there is an increase of approximately 1 dBm^2 at the central frequency using the optimized method, with respect to the normal incidence one. The latter, however, provides a flatter response within the frequency band and, therefore, a wider bandwidth.

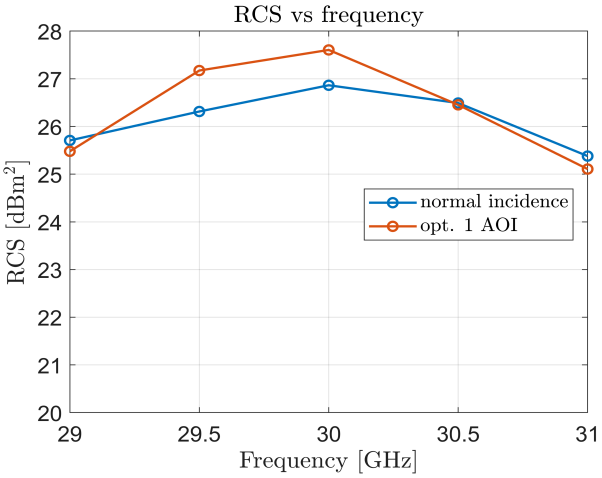

Figure 4.68: RCS versus frequency, comparison between the normal incidence and *opt. 1 AOI* method for the conformal innovative unit cell 68 × 60 SES.

4.3 Application of the double parameter technique

Using an incident plane wave as the electromagnetic field source, the Double Parameter technique mentioned in Section 3.3.4 is now exploited for the design of some CRAs. In particular, the 68 × 60 CRA in Section 4.2.6.2 is designed using the *Minimization* and *Compensation* techniques and a comparison between all the methods will be presented at the end.

4.3.1 Minimization technique 30-31 GHz

Utilizing this technique, the second parameter value is selected in a manner that minimizes the difference phase surface values. In other words, the simulated phase

at the first frequency exhibits minimal variation compared to that at the second frequency.

Using the same parameters of the 68×60 elements CRA, the resulting distribution plots are now explained and presented in Figure 4.69:

- *Required phase distribution at 30 GHz*: it is the distribution of the phase values required for each surface element evaluated at 30 GHz;

- *Required W_{side} distribution:* it is the distribution of the first parameter values for each surface element;

- *Required $W_{central}$ distribution:* it is the distribution of the second parameter values for each surface element;

- *W_{side} error distribution:* the error associated with the search for the second parameter based on minimizing frequency variation, rather than finding the closest phase value to the required one;

- *Frequency variation phase distribution*: it is the distribution of the actual phase values variation from 30 to 31 GHz with the selected parameters (the goal is to minimize it);

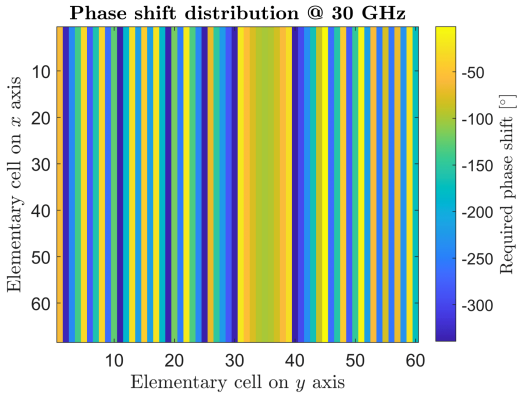

(a) Required phase distribution at 30 GHz.

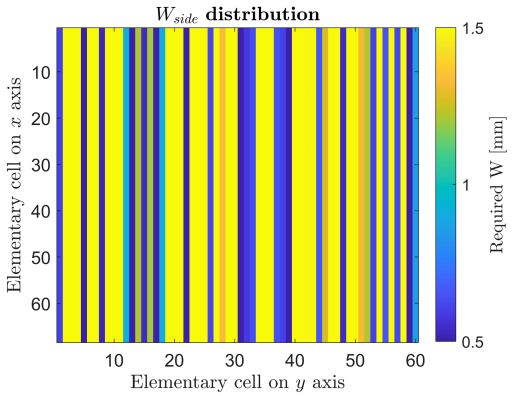

(b) Required W_{side} distribution.

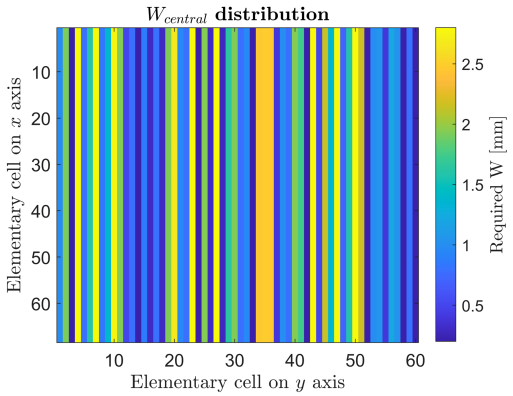

(c) Required $W_{central}$ distribution.

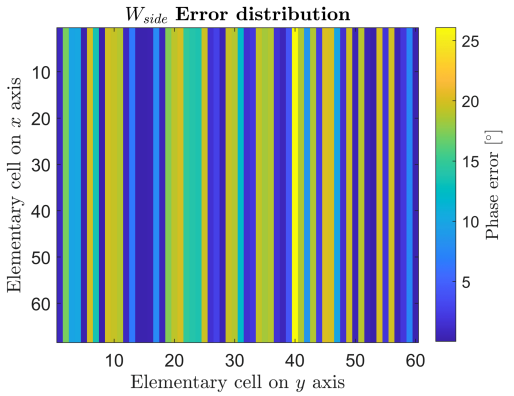

(d) W_{side} error distribution.

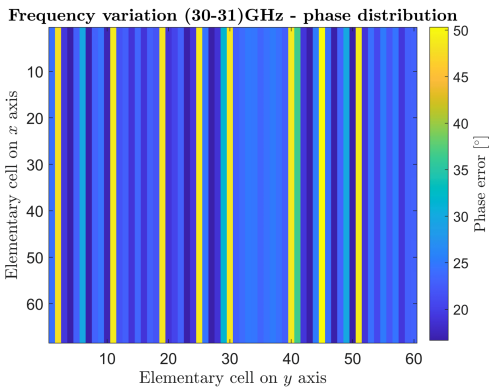

(e) Frequency variation phase distribution.

Figure 4.69: Obtained distributions for the designed conformal 68×60 SES, using the innovative unit cell and double parameter *Minimization* technique.

The designed structure is shown in Figure 4.70.

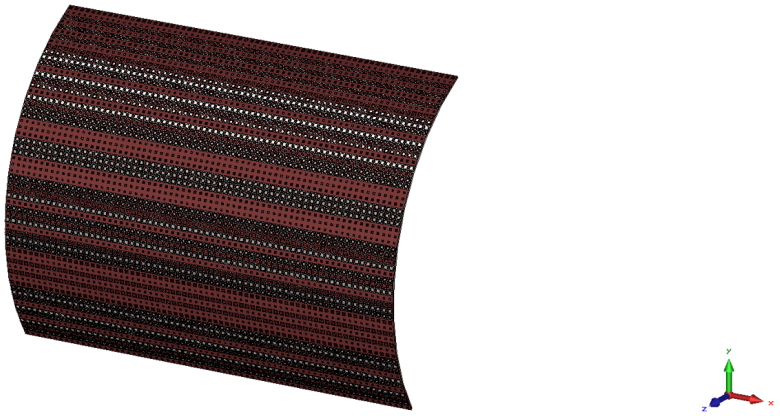

Figure 4.70: Designed conformal innovative unit cell 68 × 60 SES.

By using the *CST Microwave Studio* software, a full-wave simulation of the structure has been performed, and the resulting radiation patterns at 29, 30 and 31 GHz are depicted in Figures 4.71 and 4.72.

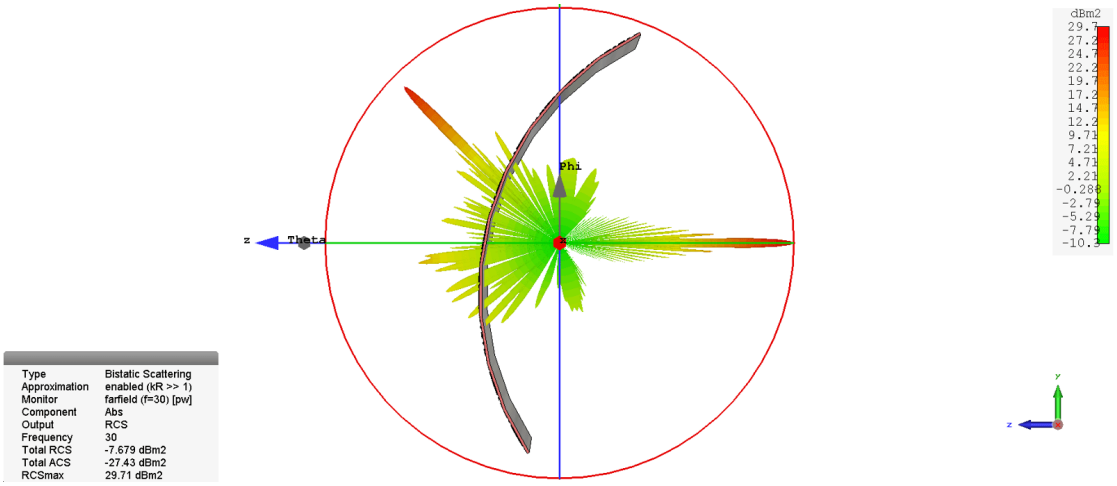

Figure 4.71: 3D radiation pattern at 30 GHz for the conformal innovative unit cell 68 × 60 SES.

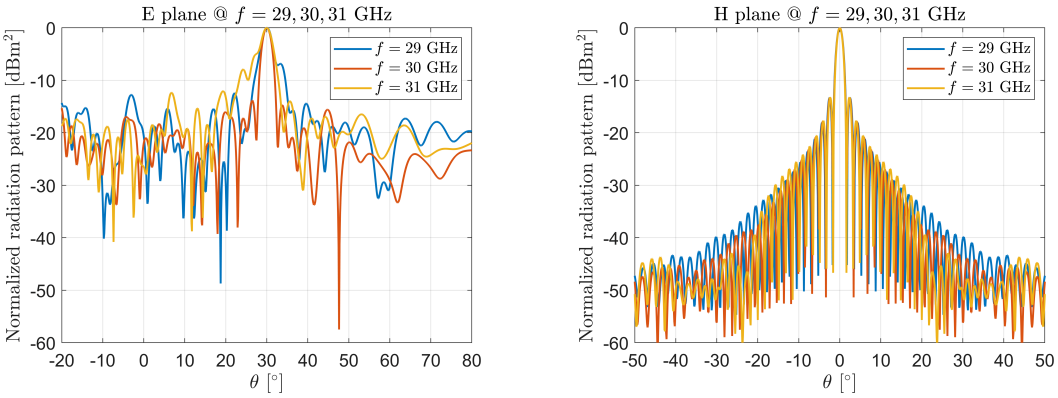

(a) E-plane of the radiation pattern.

(b) H-plane of the radiation pattern.

Figure 4.72: Radiation pattern cuts at 29, 30 and 31 GHz for the conformal innovative unit cell 68 × 60 SES.

The RCS variation in the working frequency band is shown in Figure 4.73.

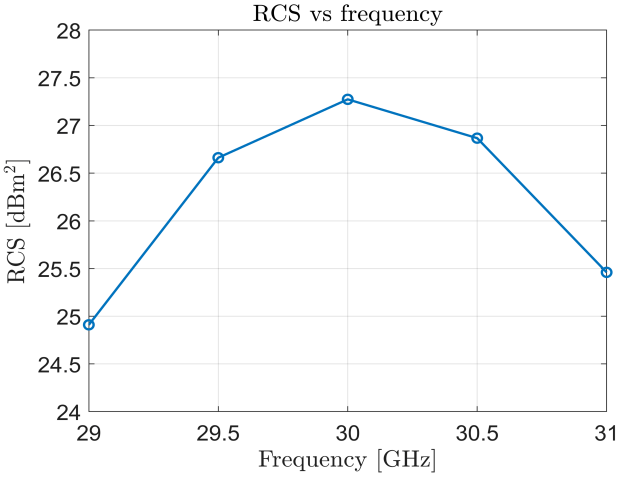

Figure 4.73: RCS versus frequency for the conformal innovative unit cell 68 × 60 SES.

From the RCS versus frequency plot, depicted in Figure 4.73, it is possible to see that the RCS value is approximately 27.3 dBm^2 at the design frequency. Moreover, from the E and H plane plots shown in Figure 4.72, it can be observed that the SLL is about -14 dBm^2, at the design frequency.

An RCS comparison plot with the normal incidence and the *opt. 1 AOI* method

is illustrated in Figure 4.74.

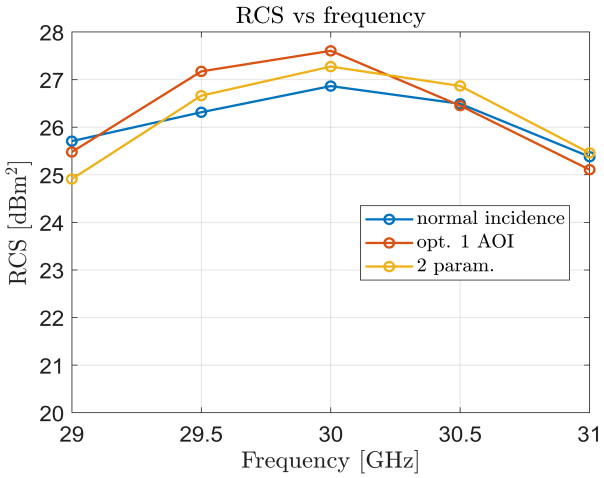

Figure 4.74: RCS versus frequency, comparison between the normal incidence, *opt. 1 AOI* and double parameter *Minimization* method for the conformal innovative unit cell 68 × 60 SES.

Using this new technique, the maximum RCS value is slightly lower with respect to the *opt. 1 AOI* method, while a flatter frequency behavior is achieved, providing a good compromise between the maximum RCS and the bandwidth. The normal incidence method, however, is a sub-optimal design with respect to the other ones and so high performance is not achieved at the design frequency. However, the response is flatter within the frequency interval, so the bandwidth will be greater.

4.3.2 Compensation technique 30-31 GHz

The second parameter value is chosen in such a way that the difference phase surface, between the 30 and 31 GHz surfaces, has the nearest value with respect to the required phase variation from one frequency to the other one.

As for the *Minimization* technique, all the plots and simulations have been also carried out for this *Compensation* technique design. For conciseness, the comparison between the two is directly shown at this point in Figures 4.75 and 4.76.

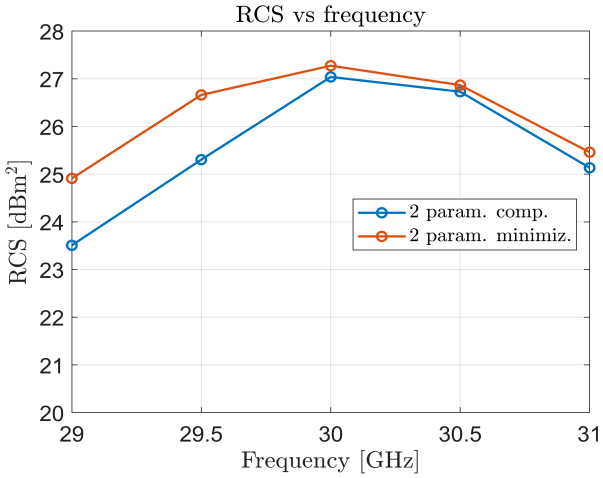

Figure 4.75: RCS versus frequency, comparison between the *Minimization* and *Compensation* method for the conformal innovative unit cell 68×60 SES.

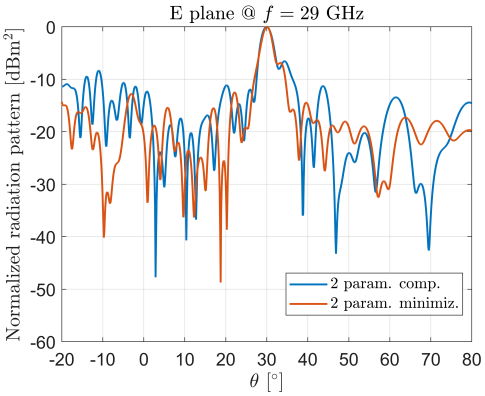

(a) E-plane of the radiation pattern, $f = 29$ GHz.

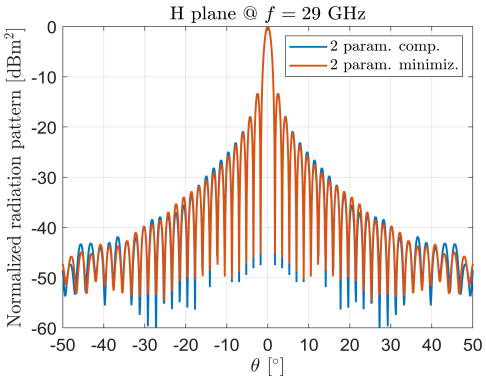

(b) H-plane of the radiation pattern, $f = 29$ GHz.

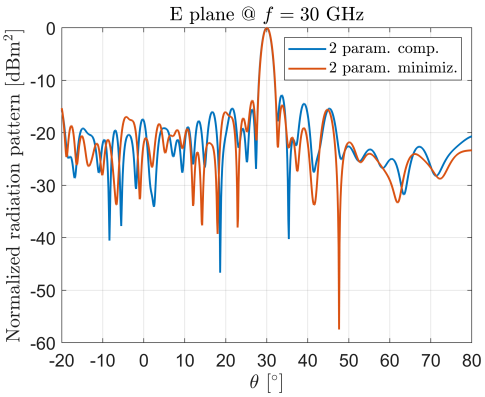

(c) E-plane of the radiation pattern, $f = 30$ GHz.

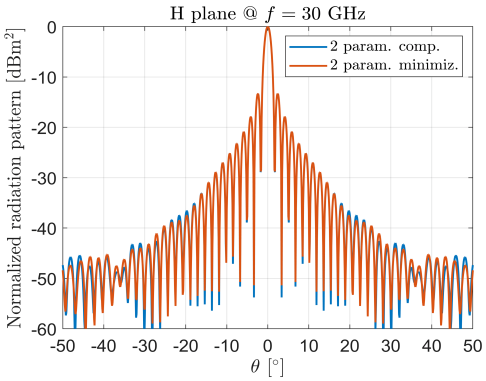

(d) H-plane of the radiation pattern, $f = 30$ GHz.

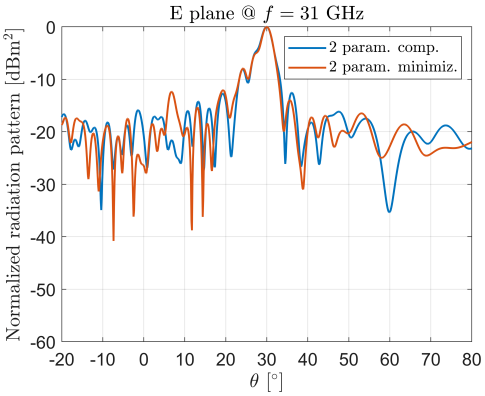

(e) E-plane of the radiation pattern, $f = 31$ GHz.

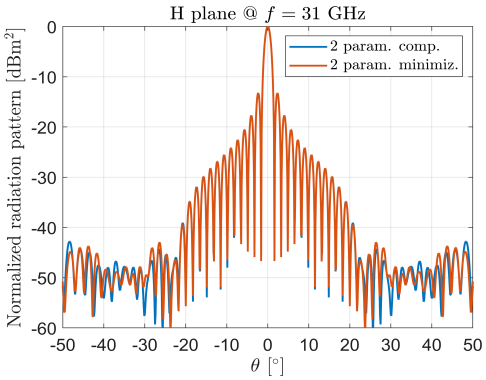

(f) H-plane of the radiation pattern, $f = 31$ GHz.

Figure 4.76: Comparison of the radiation pattern cuts at 29, 30 and 31 GHz for the innovative unit cell *Minimization* and *Compensation* method SESs.

As can be observed from Figures 4.75 and 4.76, the *Minimization* technique provides better results at all the frequencies in the working band. The flatness of the frequency behavior is also an important feature: hence, from now on, only this method will be considered between these two.

In Table 4.3, the performances achieved with the 4 different techniques are summarized.

Considered method	RCS @$f = 29$ GHz	RCS @$f = 30$ GHz	RCS @$f = 31$ GHz
Normal incidence	25.7	26.9	25.4
Opt. 1 AOI	25.5	27.6	25.1
2 param. *Minimiz.*	24.9	27.3	25.5
2 param. *Compens.*	23.5	27.0	25.1

Table 4.3: RCS [dBm^2] comparison of the different methods at $f = 29$, 30 and 31 GHz.

The *Compensation* technique performs better than the normal incidence one at the central frequency; however, its behavior becomes worse at the other frequencies. The comments made at the end of Section 4.3.1 regarding the other methods are also applicable here.

An RCS comparison plot with the square patch using normal incidence is shown in Figure 4.77.

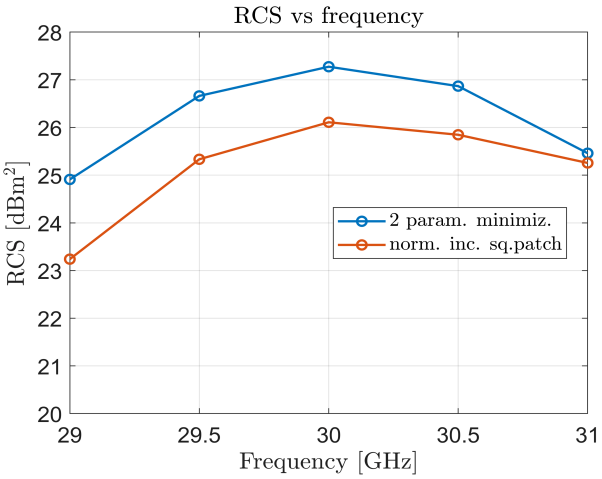

Figure 4.77: RCS versus frequency, comparison between the *Minimization* method and the square patch unit cell for the 68×60 CRA

As can be seen, there is a 1 dBm^2 increase at the central frequency when using this new technique and a gain of around 2 dBm^2 at 29 GHz. At 31 GHz, the behavior is quite similar, with no significant improvements observed.

4.3.3 Minimization and compensation techniques 29-31 GHz

At this stage, the *Minimization* and *Compensation* techniques that were previously considered are here applied using the $29-31$ GHz phase surfaces, instead of the $30-31$ GHz ones used before. This means that the first parameter is still evaluated at the central frequency (30 GHz) while selecting the second one according to the 29 and 31 GHz phase surfaces. The aim is to either minimize the variation of the required phase values between these two frequencies (*Minimization*) or compensate it (*Compensation*). The design procedure is identical to the one previously employed and is thus omitted at this point.

An RCS comparison plot is shown in Figure 4.78, where the *Minimization* technique at $30-31$ GHz is compared to the new *Minimization* at $29-31$ GHz and *Compensation* at $29-31$ GHz techniques.

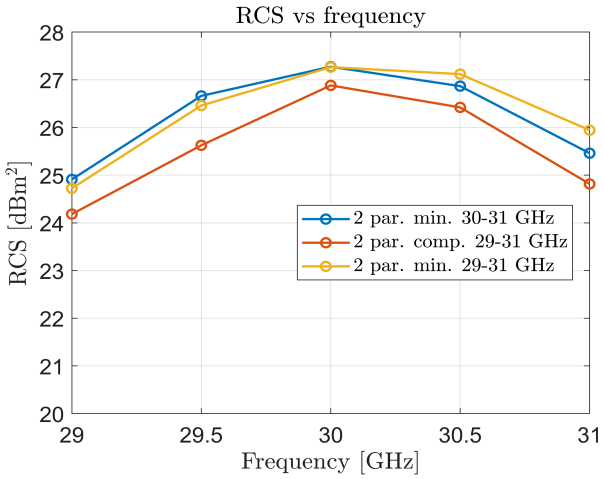

Figure 4.78: RCS versus frequency, comparison between the *Minimization* at $30-31$ method and the *Minimization* at $29-31$ GHz and *Compensation* at $29-31$ GHz methods for the 68×60 CRA

As shown by Figure 4.78, the *Compensation* technique, at $29-31$ GHz in this

case, is still the worse performance one. The *Minimization* technique at $29-31$ provides a modestly higher RCS value at the upper frequency, with a slightly lower value at the lower frequency. In conclusion, the *Minimization* technique is certainly the best solution in this case, both the $30-31$ and $29-31$ GHz types. Based on the requirements, one can choose one or the other in order to enhance the lower or the upper frequency performance, respectively.

Chapter 5

Conclusions

The thesis activity has been focused on the possibility to enhance the capabilities of 5G and beyond wireless communication networks in an urban scenario without increasing the number of base stations, but with the introduction of smart electromagnetic skins (SESs), properly integrated in the environment. SES are passive thin surface, able to produce a not specular reflection thanks to the local control of its reflecting properties. This is achieved discretizing the surface with unit cells, that could have either a resonant or sub-wavelength size. In both the cases, one or more geometrical parameters of each unit cell is varied, to locally change the reflection coefficient or the surface impedance provided by the unit cell itself. Here resonant unit cells have been selected to discretize the SES.

The first step has been the assessment of the procedure for the design of a SES. It works similarly to a reflectarray (RA), being the main difference between the two structures the distance between the reflecting surface and the source of the incident field: in the case of a RA the feed is located relatively near to the reflecting surface, and therefore the radiated filed distribution on it must be evaluated to design the unit cells. Vice versa, in the case of a SES located in outdoor environment, it is generally so far from the base station that the incident field can be modeled by a plane wave. In view of this considerations, RAs have been used as benchmark structures.

While in the first phase a simple unit cell has been adopted, consisting in a square patch printed on a backgrounded dielectric layer, the most part of the activity has been focused on the development of an innovative unit cell with enhanced properties. The resulting configuration consists in a square patch located inside a square ring with a notch on each side. It presents the advantages of providing a larger range of variation for the phase of the reflection coefficient and to present several degrees of freedom. The optimization procedure that brings to the unit cell definition is described in Chapter 3. The effectiveness of the new unit cell has been tested using it for the design of a RA and comparing its performance with those of a similar reflectarray, using square patches. The results of its numerical analysis, carried out using *CST Microwave Studio*, show that the RA designed with the introduced unit cell has a 1 dB higher gain at the central frequency. Results on the dependence of the unit cell from frequency and direction of arrival of the incident field have also been obtained and discussed.

Moreover, the possibility of using two geometrical parameters to control the unit cell performance has been investigated. Two different approaches have been introduced, named the *Minimization* and *Compensation* techniques, exploiting the new degree of freedom given by the second parameter of the unit cell. In the first technique, the second parameter is selected to minimize the required phase distribution variation at a certain frequency with respect to another one. The second one, instead, aims to use the second parameter to compensate for the required phase variation between the two frequencies.

Once that the effectiveness of the unit cell has been verified, it has been adopted for designing different smart electromagnetic skins. Two different types of structure, for different applications, have been considered. In the first case the SES is planar, for its possible integration in the wall of a building, while a considered alternative is that of mounting the smart skin on a traffic light or street light pole, in which case a curved structure is more suitable. Also in this case, the performance has been compared with that of similar configurations using square patches as re-radiating elements. First, the unit cell with a single degree of freedom has been considered. The results summarized in Chapter 4 show that to obtain the highest RCS value at

the design frequency, the most promising design method is that of using the curve representing the variation of the angle of the reflection coefficient vs. the selected geometrical parameter of the unit cell evaluated for the direction of incidence of the plane wave; in this way, the highest value of the maximum RCS at almost all the considered cases, i.e. for different angles of incidence, is obtained. An alternative consists in using for the design of the SES variation of the magnitude and phase of the reflection coefficient evaluated with normal incidence method: it provides minimal variation within the frequency band. It is therefore possible to conclude that, depending on the specific requirements of a given application, one may choose to have a higher maximum RCS or a wider bandwidth.

Finally, the Double Parameter techniques have been tested, through their application to the design of SESs. While the *Compensation* technique has enhanced the performance of the designed surface only at the design frequency, the *Minimization* approach has been proved to be the most suitable solution if the application demands both a high RCS value and a wide bandwidth. The minimization of the required phase distribution variation has been carried out between the lower and central frequency phase distributions, resulting in an improved RCS value at the higher frequencies.

Further upgrades can be investigated by modifying the innovative unit cell presented in this work, to achieve even better results. For example, a different substrate material and thickness can be selected or minor changes at the metal patch geometrical shape can be brought to get a different S-curve and re-radiated field characteristics from the SES.

Appendix A

Material characteristics

A.1 Dielectric constant and loss tangent

For dielectric materials, the dielectric constant and loss tangent are calculated as

$$\varepsilon_r = \varepsilon_0(\varepsilon_r' + j\varepsilon_r'') = \varepsilon_0(n^2 - k^2 + j2nk) \tag{A.1}$$

$$\tan\delta = \frac{\varepsilon_r''}{\varepsilon_r'} = \frac{2nk}{n^2 - k^2} \tag{A.2}$$

with $\tilde{n} = n + jk$ the complex refractive index of the material.

A.2 Metal conductivity

The metal conductivity is defined as

$$\sigma = j\omega\varepsilon_0(\tilde{n}^2) = \omega\varepsilon_0\left[2nk + j\left(n^2 + k^2\right)\right] \tag{A.3}$$

with $\tilde{n} = n + jk$ the complex refractive index of the material.

Appendix B

DXF file

B.1 DXF specifications

A DXF file[54] is organized with header, classes, tables, blocks, entities and objects sections. The file format requires the vertex positioning of the single patch, for example, a square, to follow a specific order. The vertex positions have to be specified in a manner that creates a closed loop with a counter clockwise order. Once the four vertices have been written in the file with the correct syntax, the square patch is created. This four vertices must be specified in the file for each patch element, along with its position (with respect to the antenna center).

An example of a DXF file with the patch shape is presented in Figure B.1.

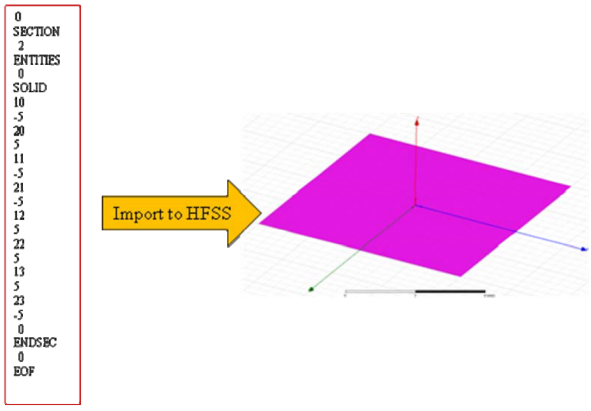

Figure B.1: DXF file and geometrical shape for a patch. [55]

B.2 DXF mask generation

Once the required phase change for all the elements on the reflectarray surface has been evaluated, the element dimensions can be determined from the S-curve diagram, as highlighted in the previous chapters.

Using *Matlab*, it is possible to obtain a M×N matrix with M and N the number of elements in the vertical and horizontal direction (the number of rows and columns, respectively) containing the *mask* of the patch elements (i.e. the patch size distribution). With this matrix it is possible to get results similar to Figure 2.19 and 2.23.

In order to speed up the process of the reflectarray simulation, it is possible to save this matrix into a file and import it into *CST Microwave Studio* to create the patch distribution of the designed antenna. This can be accomplished by using a particular file format, the DXF, which is a very common geometry format for 2-D structures.

For the conformal configuration, the same approach can be used: the dependency on the z coordinates has been considered in the phase distribution evaluation and the *mask* is still a 2-D geometry file, exploiting x and y components only.

B.3 Final UC configuration - DXF file Matlab function

In the following sections, the two *Matlab* functions used to generate the DXF file for the innovative UC are presented. Beyond these files, it is also necessary to write a proper DXF *Header* and a correct file *Close*.

B.3.1 DXF rectangle Matlab function

The `dxfRectangle` function takes as inputs the dimensions and the center of a rectangle and writes its four vertices with cartesian coordinates

$$(X_1, Y_1), (X_1, Y_2), (X_2, Y_1), (X_2, Y_2)$$

into a file, using the DXF file format. The reference system is shown in Figure B.2.

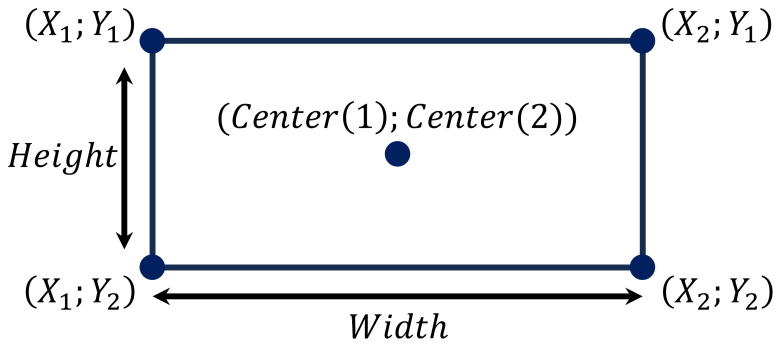

Figure B.2: Coordinate system for the rectangle in the DXF file.

```
1
2  function dxfRectangle(fid,Center,Width,Height)
3
4  X1 = Center(1) - Width/2;
5  X2 = Center(1) + Width/2;
6
7  Y1 = Center(2) + Height/2;
8  Y2 = Center(2) - Height/2;
9
10 fprintf(fid, '0\n');
11 fprintf(fid, 'SOLID\n');
12 % Write vertex (X1,Y1)
13 fprintf(fid, '10\n');
14 fprintf(fid, '%f\n',X1);
15 fprintf(fid, '20\n');
16 fprintf(fid, '%f\n',Y1);
17
18 % Write vertex (X1,Y2)
19 fprintf(fid, '11\n');
20 fprintf(fid, '%f\n',X1);
21 fprintf(fid, '21\n');
22 fprintf(fid, '%f\n',Y2);
23
24 % Write vertex (X2,Y1)
```

```
fprintf(fid, '12\n');
fprintf(fid, '%f\n',X2);
fprintf(fid, '22\n');
fprintf(fid, '%f\n',Y1);

% Write vertex (X2,Y2)
fprintf(fid, '13\n');
fprintf(fid, '%f\n',X2);
fprintf(fid, '23\n');
fprintf(fid, '%f\n',Y2);
```

B.3.2 DXF innovative UC Matlab function

The `DXFnewUC` function takes as inputs the value of the W_{side} parameter and the center of the $i-$th considered unit cell on the surface, and writes the required DXF code to create this unit cell shape into the DXF file.

It has been divided into 13 rectangular patches, that are written separately into the file, according to Figure B.3, using the above mentioned `dxfRectangle` function.

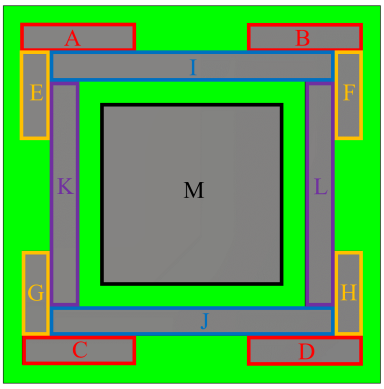

Figure B.3: Innovative unit cell partition into 13 rectangles.

```
1
2  function DXFnewUC(fid,Center,W_side)
3
4  % defined parameters
5  W_in=2.5*W_side;
6  SL=W_side;
7  InW=0.25*W_side;
8  Inspace=0.2*W_side;
9
10 % creating A element
11 c_A_x=Center(1)-SL;
12 c_A_y=Center(2)+SL+InW+0.5*InW;
13 dxfRectangle(fid, [c_A_x, c_A_y], W_side, InW);
14
15 % creating B element
16 c_B_x=Center(1)+SL;
17 c_B_y=Center(2)+SL+InW+0.5*InW;
18 dxfRectangle(fid, [c_B_x, c_B_y], W_side, InW);
19
20 % creating C element
21 c_C_x=Center(1)-SL;
22 c_C_y=Center(2)-SL-InW-0.5*InW;
23 dxfRectangle(fid, [c_C_x, c_C_y], W_side, InW);
24
25 % creating D element
26 c_D_x=Center(1)+SL;
27 c_D_y=Center(2)-SL-InW-0.5*InW;
28 dxfRectangle(fid, [c_D_x, c_D_y], W_side, InW);
29
30 % creating E element
31 c_E_x=Center(1)-SL-3/2*InW;
32 c_E_y=Center(2)+SL+W_side/2-InW-(W_side-InW)/2;
33 dxfRectangle(fid, [c_E_x, c_E_y], InW, W_side-InW);
34
35 % creating F element
```

```
c_F_x=Center(1)+SL+3/2*InW;
c_F_y=Center(2)+SL+W_side/2-InW-(W_side-InW)/2;
dxfRectangle(fid, [c_F_x, c_F_y], InW, W_side-InW);

% creating G element
c_G_x=Center(1)-SL-3/2*InW;
c_G_y=Center(2)-(SL+W_side/2-InW-(W_side-InW)/2);
dxfRectangle(fid, [c_G_x, c_G_y], InW, W_side-InW);

% creating H element
c_H_x=Center(1)+SL+3/2*InW;
c_H_y=Center(2)-(SL+W_side/2-InW-(W_side-InW)/2);
dxfRectangle(fid, [c_H_x, c_H_y], InW, W_side-InW);

% creating I element
c_I_x=Center(1);
c_I_y=Center(2)+SL+InW/2;
dxfRectangle(fid, [c_I_x, c_I_y], W_in, InW);

% creating J element
c_J_x=Center(1);
c_J_y=Center(2)-(SL+InW/2);
dxfRectangle(fid, [c_J_x, c_J_y], W_in, InW);

% creating K element
c_K_x=Center(1)-W_in/2+InW/2;
c_K_y=Center(2);
dxfRectangle(fid, [c_K_x, c_K_y], InW, W_in-2*InW);

% creating L element
c_L_x=Center(1)-(-W_in/2+InW/2);
c_L_y=Center(2);
dxfRectangle(fid, [c_L_x, c_L_y], InW, W_in-2*InW);

% creating M element
```

```
71 central_square_dim=W_in-2*InW-2*Inspace;
72 c_M_x=Center(1);
73 c_M_y=Center(2);
74 dxfRectangle(fid, [c_M_x, c_M_y], central_square_dim,
   ↪  central_square_dim);
75
76 end
```

Bibliography

[1] Y.J. Guo and R.W. Ziolkowski. *Advanced Antenna Array Engineering for 6G and Beyond Wireless Communications*. Wiley, 2021. ISBN: 9781119712923 (cit. on p. 2).

[2] Harsh Tataria, Mansoor Shafi, Andreas F. Molisch, Mischa Dohler, Henrik Sjöland, and Fredrik Tufvesson. «6G Wireless Systems: Vision, Requirements, Challenges, Insights, and Opportunities». In: *Proceedings of the IEEE* 109.7 (2021), pp. 1166–1199. DOI: 10.1109/JPROC.2021.3061701 (cit. on p. 2).

[3] Shahid Mumtaz, Josep Jornet, Jocelyn Aulin, Wolfgang Gerstacker, Xiaodai Dong, and bo ai bo. «Terahertz Communication for Vehicular Networks». In: *IEEE Transactions on Vehicular Technology* 66 (July 2017), pp. 5617–5625. DOI: 10.1109/TVT.2017.2712878 (cit. on p. 2).

[4] Barry Evans. «6G Satellite Communications». In: *2022 27th Asia Pacific Conference on Communications (APCC)*. 2022, pp. 175–177. DOI: 10.1109/APCC55198.2022.9943787 (cit. on p. 2).

[5] Ting Ma, Bo Qian, Xiaohan Qin, Xiaoyu Liu, Haibo Zhou, and Lian Zhao. «Satellite-Terrestrial Integrated 6G: An Ultra-Dense LEO Networking Management Architecture». In: *IEEE Wireless Communications* (2022), pp. 1–8. DOI: 10.1109/MWC.011.2200198 (cit. on p. 2).

[6] Mostafa Zaman Chowdhury, Md. Shahjalal, Shakil Ahmed, and Yeong Min Jang. *6G Wireless Communication Systems: Applications, Requirements, Technologies, Challenges, and Research Directions*. 2019. arXiv: 1909.11315 [cs.NI] (cit. on p. 3).

[7] Michail Matthaiou, Okan Yurduseven, Hien Quoc Ngo, David Morales-Jimenez, Simon L. Cotton, and Vincent F. Fusco. «The Road to 6G: Ten Physical Layer Challenges for Communications Engineers». In: *IEEE Communications Magazine* 59.1 (2021), pp. 64–69. DOI: 10.1109/MCOM.001.2000208 (cit. on p. 3).

[8] Danilo Erricolo, Anastasiia Rozhkova, and Alex C. Stutts. «Towards Smart Electromagnetic Environments». In: *2021 Computing, Communications and IoT Applications (ComComAp)*. 2021, pp. 361–366. DOI: 10.1109/ComComAp53641.2021.9653070 (cit. on pp. 3, 8, 10, 11).

[9] Yuanwei Liu, Xiao Liu, Xidong Mu, Tianwei Hou, Jiaqi Xu, Marco Di Renzo, and Naofal Al-Dhahir. «Reconfigurable Intelligent Surfaces: Principles and Opportunities». In: *IEEE Communications Surveys & Tutorials* 23.3 (2021), pp. 1546–1577. DOI: 10.1109/COMST.2021.3077737 (cit. on pp. 3, 9).

[10] D. Smith, Okan Yurduseven, Laura Pulido-Mancera, Patrick Bowen, and Nathan Kundtz. «Analysis of a Waveguide-Fed Metasurface Antenna». In: *Physical Review Applied* 8 (Nov. 2017), p. 054048. DOI: 10.1103/PhysRevApplied.8.054048 (cit. on p. 4).

[11] Min Wang, Shenheng Xu, Fan Yang, and Maokun Li. «A 1-Bit Bidirectional Reconfigurable Transmit-Reflect-Array Using a Single-Layer Slot Element With PIN Diodes». In: *IEEE Transactions on Antennas and Propagation* 67.9 (2019), pp. 6205–6210. DOI: 10.1109/TAP.2019.2925925 (cit. on p. 4).

[12] Shuhao Zeng, Hongliang Zhang, Boya Di, Yunhua Tan, Zhu Han, H. Vincent Poor, and Lingyang Song. «Reconfigurable Intelligent Surfaces in 6G: Reflective, Transmissive, or Both?» In: *IEEE Communications Letters* 25 (2021), pp. 2063–2067 (cit. on p. 4).

[13] Ana Dìaz-Rubio, Viktar Asadchy, Amr Elsakka and, and Sergei Tretyakov. *From the generalized reflection law to the realization of perfect anomalous reflectors*. 2016. DOI: 10.48550/ARXIV.1609.08041 (cit. on p. 4).

[14] Zijian Zhang, Linglong Dai, Xibi Chen, Changhao Liu, Fan Yang, Robert Schober, and H. Vincent Poor. «Active RIS vs. Passive RIS: Which Will Prevail in 6G?» In: *IEEE Transactions on Communications* (2022). DOI: 10.1109/tcomm.2022.3231893 (cit. on p. 5).

[15] *Surface Electromagnetics: With Applications in Antenna, Microwave, and Optical Engineering*. Cambridge University Press, 2019. DOI: 10.1017/9781108470261 (cit. on p. 6).

[16] Christos Liaskos, Ageliki Tsioliaridou, Andreas Pitsillides, Sotiris Ioannidis, and Ian Akyildiz. «Using any Surface to Realize a New Paradigm for Wireless Communications». In: (June 2018) (cit. on p. 8).

[17] Roberto Flamini, Danilo De Donno, Jonathan Gambini, Francesco Giuppi, Christian Mazzucco, Angelo Milani, and Laura Resteghini. «Toward a Heterogeneous Smart Electromagnetic Environment for Millimeter-Wave Communications: An Industrial Viewpoint». In: *IEEE Transactions on Antennas and Propagation* 70.10 (2022), pp. 8898–8910. DOI: 10.1109/TAP.2022.3151978 (cit. on pp. 9, 10).

[18] Marco Di Renzo, Alessio Zappone, Merouane Debbah, Mohamed-Slim Alouini, Chau Yuen, Julien de Rosny, and Sergei Tretyakov. «Smart Radio Environments Empowered by Reconfigurable Intelligent Surfaces: How It Works, State of Research, and The Road Ahead». In: *IEEE Journal on Selected Areas in Communications* 38.11 (2020), pp. 2450–2525. DOI: 10.1109/JSAC.2020.3007211 (cit. on p. 9).

[19] Giacomo Oliveri, Francesco Zardi, Paolo Rocca, Marco Salucci, and Andrea Massa. «Building a Smart EM Environment - AI-Enhanced Aperiodic Micro-Scale Design of Passive EM Skins». In: *IEEE Transactions on Antennas and Propagation* 70.10 (2022), pp. 8757–8770. DOI: 10.1109/TAP.2022.3151354 (cit. on p. 9).

[20] Linglong Dai et al. «Reconfigurable Intelligent Surface-Based Wireless Communications: Antenna Design, Prototyping, and Experimental Results». In: *IEEE Access* 8 (2020), pp. 45913–45923. DOI: 10.1109/ACCESS.2020.2977772 (cit. on p. 9).

[21] Steven Kisseleff, Wallace A. Martins, Hayder Al-Hraishawi, Symeon Chatzinotas, and Björn Ottersten. «Reconfigurable Intelligent Surfaces for Smart Cities: Research Challenges and Opportunities». In: *IEEE Open Journal of the Communications Society* 1 (2020), pp. 1781–1797. DOI: 10.1109/OJCOMS.2020.3036839 (cit. on p. 9).

[22] Giacomo Oliveri, Francesco Zardi, Paolo Rocca, Marco Salucci, and Andrea Massa. «Constrained Design of Passive Static EM Skins». In: *IEEE Transactions on Antennas and Propagation* 71.2 (2023), pp. 1528–1538. DOI: 10.1109/TAP.2022.3225593 (cit. on p. 9).

[23] Qingqing Wu, Shuowen Zhang, Beixiong Zheng, Changsheng You, and Rui Zhang. «Intelligent Reflecting Surface-Aided Wireless Communications: A Tutorial». In: *IEEE Transactions on Communications* 69.5 (2021), pp. 3313–3351. DOI: 10.1109/TCOMM.2021.3051897 (cit. on p. 10).

[24] Ertugrul Basar, Marco Di Renzo, Julien De Rosny, Merouane Debbah, Mohamed-Slim Alouini, and Rui Zhang. «Wireless Communications Through Reconfigurable Intelligent Surfaces». In: *IEEE Access* 7 (2019), pp. 116753–116773. DOI: 10.1109/ACCESS.2019.2935192 (cit. on p. 10).

[25] Jun Zhao. *A Survey of Intelligent Reflecting Surfaces (IRSs): Towards 6G Wireless Communication Networks*. 2019. arXiv: 1907.04789 [eess.SP] (cit. on p. 10).

[26] Álvaro F. Vaquero, Eduardo Martinez-De-Rioja, Manuel Arrebola, and José A. Encinar. «Study on the Effect of the Wall in the Performance of an Intelligent Reflective Surface for Providing Coverage in mm-Wave Frequencies». In: *2023 17th European Conference on Antennas and Propagation (EuCAP)*. 2023, pp. 1–5. DOI: 10.23919/EuCAP57121.2023.10133685 (cit. on p. 10).

[27] Özgecan Özdogan, Emil Björnson, and Erik G. Larsson. *Intelligent Reflecting Surfaces: Physics, Propagation, and Pathloss Modeling*. 2019. DOI: 10.48550/ARXIV.1911.03359 (cit. on p. 11).

[28] Emil Björnson. *Reconfigurable intelligent surfaces: Myths and realities*. https://github.com/emilbjornson/presentation_slides/raw/master/IRS_myths_and_realities.pdf. (visited on 08/12/2023). 2020 (cit. on p. 12).

[29] Emil Björnson, Özgecan Özdogan, and Erik G. Larsson. «Intelligent Reflecting Surface Versus Decode-and-Forward: How Large Surfaces are Needed to Beat Relaying?» In: *IEEE Wireless Communications Letters* 9.2 (2020), pp. 244–248. DOI: 10.1109/LWC.2019.2950624 (cit. on pp. 14, 15).

[30] Ludek Subrt, David Grace, and Pavel Pechac. «Controlling the Short-Range Propagation Environment Using Active Frequency Selective Surfaces». In: *Radioengineering* 19 (Dec. 2010) (cit. on p. 15).

[31] Paolo Rocca, Pietro Da Rù, Nicola Anselmi, Marco Salucci, Giacomo Oliveri, Danilo Erricolo, and Andrea Massa. «On the Design of Modular Reflecting EM Skins for Enhanced Urban Wireless Coverage». In: *IEEE Transactions on Antennas and Propagation* 70.10 (2022), pp. 8771–8784. DOI: 10.1109/TAP.2022.3146870 (cit. on pp. 16–19).

[32] Eduardo Martinez-de-Rioja, Álvaro F. Vaquero, Manuel Arrebola, Eduardo Carrasco, Jose A. Encinar, and Maha Achour. «Passive intelligent reflecting surfaces based on reflectarray panels to enhance 5G millimeter-wave coverage». In: *International Journal of Microwave and Wireless Technologies* (2022), pp. 1–12. DOI: 10.1017/S1759078722000721 (cit. on pp. 19–21).

[33] Venkat Arun and Hari Balakrishnan. «RFocus: Beamforming Using Thousands of Passive Antennas». In: *17th USENIX Symposium on Networked Systems Design and Implementation (NSDI 20)*. Santa Clara, CA: USENIX Association, Feb. 2020, pp. 1047–1061. ISBN: 978-1-939133-13-7. URL: https://www.usenix.org/conference/nsdi20/presentation/arun (cit. on pp. 21, 22).

[34] Daisuke Kitayama, Yuto Hama, Kenta Goto, Kensuke Miyachi, Takeshi Motegi, and Osamu Kagaya. «Transparent dynamic metasurface for a visually unaffected reconfigurable intelligent surface: controlling transmission/reflection and making a window into an RF lens». In: *Opt. Express* 29.18 (Aug. 2021), pp. 29292–29307. DOI: 10.1364/OE.435648 (cit. on pp. 23, 24).

[35] J. Huang and J.A. Encinar. *Reflectarray Antennas*. Hoboken: IEEE Press, John Wiley and Sons, 2007. ISBN: 9780470178768 (cit. on pp. 26, 28, 31, 38, 50, 51).

[36] Michele Beccaria, Alessandro Niccolai, Riccardo E. Zich, and Paola Pirinoli. «Shaped-Beam Reflectarray Design by Means of Social Network Optimization (SNO)». In: *Electronics* 10.6 (2021). ISSN: 2079-9292. DOI: 10.3390/electronics10060744. URL: https://www.mdpi.com/2079-9292/10/6/744 (cit. on p. 27).

[37] P. Nayeri, F. Yang, and A.Z. Elsherbeni. *Reflectarray Antennas: Theory, Designs, and Applications*. IEEE Press. Wiley, 2018. ISBN: 9781118846766 (cit. on pp. 28, 30, 45, 48, 56, 57).

[38] Philippe Dreyer, Juan Diaz, and Julien Perruisseau-Carrier. «Design of a reflectarray element integrated in a Solar Cell panel». In: July 2013, pp. 1558–1559. ISBN: 978-1-4673-5317-5. DOI: 10.1109/APS.2013.6711438 (cit. on p. 30).

[39] Min Zhou, Stig B. Sørensen, Peter Meincke, and Erik Jørgensen. «Design and optimization of multi-faceted reflectarrays for satellite applications». In: *The 8th European Conference on Antennas and Propagation (EuCAP 2014)*. 2014, pp. 1423–1427. DOI: 10.1109/EuCAP.2014.6902047 (cit. on p. 32).

[40] Min Zhou and Stig B. Sørensen. «Multi-spot beam reflectarrays for satellite telecommunication applications in Ka-band». In: *2016 10th European Conference on Antennas and Propagation (EuCAP)*. 2016, pp. 1–5. DOI: 10.1109/EuCAP.2016.7481438 (cit. on p. 32).

[41] Jinsu Park, Hong Jun Lim, Son Trinh-Van, Daesung Park, Youn Kwon Jung, Dongju Lim, and Keum Cheol Hwang. «Derivation of a Universally Valid Array Factor of a Conformal Arrays Based on Phase Compensation and Genetic Learning Particle Swarm Optimization». In: *Applied Sciences* 12.13 (2022). ISSN: 2076-3417. DOI: 10.3390/app12136501. URL: https://www.mdpi.com/2076-3417/12/13/6501 (cit. on p. 33).

[42] Payam Nayeri and Atef Elsherbeni. «Radiation Analysis and Characteristics of Conformal Reflectarray Antennas». In: *International Journal of Antennas and Propagation* 2012 (July 2012). DOI: 10.1155/2012/784045 (cit. on pp. 33, 41).

[43] M. Beccaria, P. Pirinoli, G. Dassano, and M. Orefice. «Design and experimental validation of convex conformal reflectarray antennas». In: *Electronics Letters* 52.18 (2016), pp. 1511–1512. DOI: https://doi.org/10.1049/el.2016.2128 (cit. on p. 34).

[44] Shenheng Xu and Fan Yang. «Reflectarray Antennas». In: *Handbook of Antenna Technologies*. Ed. by Zhi Ning Chen, Duixian Liu, Hisamatsu Nakano, Xianming Qing, and Thomas Zwick. Singapore: Springer Singapore, 2016, pp. 1279–1320. ISBN: 978-981-4560-44-3. DOI: 10.1007/978-981-4560-44-3_45. URL: https://doi.org/10.1007/978-981-4560-44-3_45 (cit. on p. 34).

[45] Dassault Systèmes. *CST Microwave Studio*. 2015. URL: http://www.cst.com/ (visited on 09/13/2023) (cit. on p. 35).

[46] J. Shaker, M.R. Chaharmir, and J. Ethier. *Reflectarray Antennas: Analysis, Design, Fabrication, and Measurement*. Antennas and Propagation. Artech House, 2013. ISBN: 9781608074990 (cit. on pp. 52, 53).

[47] Sandra Costanzo, Francesca Venneri, and Giuseppe Di Massa. «Modified Minkowski Fractal Unit Cell for Reflectarrays with Low Sensitivity to Mutual Coupling Effects». In: *International Journal of Antennas and Propagation* 2019 (Feb. 2019), pp. 1–11. DOI: 10.1155/2019/4890710 (cit. on p. 59).

[48] Huaiqing Zhang, Jiapeng Wang, Hui Xiao, and Xin Wang. «A Broadband Reflectarray Antenna for Microwave Power Transmission». In: *Advances in Astronautics Science and Technology* 5.1 (Mar. 2022), pp. 65–71. ISSN: 2524-5260. DOI: 10.1007/s42423-022-00103-x. URL: https://doi.org/10.1007/s42423-022-00103-x (cit. on p. 60).

[49] Gyoungdeuk Kim, Myeongha Hwang, Hyunmin Jeong, Chul-Min Lim, Kyoung Youl Park, and Sangkil Kim. «Design of a Flat-Panel Metasurface Reflectarray C-Band Antenna». In: *Electronics* 11.17 (2022). ISSN: 2079-9292. DOI: 10.3390/electronics11172729. URL: https://www.mdpi.com/2079-9292/11/17/2729 (cit. on p. 60).

[50] S. Costanzo and F. Venneri. «Miniaturized Fractal Reflectarray Element Using Fixed-Size Patch». In: *IEEE Antennas and Wireless Propagation Letters* 13 (2014), pp. 1437–1440. DOI: 10.1109/LAWP.2014.2341032 (cit. on pp. 61, 62).

[51] Sandra Costanzo, Francesca Venneri, Giuseppe Di Massa, Antonio Borgia, Antonio Costanzo, and Antonio Raffo. «Fractal Reflectarray Antennas: State of Art and New Opportunities». In: *International Journal of Antennas and Propagation* 2016 (2016), pp. 1–17 (cit. on p. 61).

[52] Michele Beccaria, Giuseppe Addamo, Mario Orefice, Oscar Peverini, Diego Manfredi, Flaviana Calignano, Giuseppe Virone, and Paola Pirinoli. «Enhanced Efficiency and Reduced Side Lobe Level Convex Conformal Reflectarray». In: *Applied Sciences* 11.21 (2021). ISSN: 2076-3417. DOI: 10.3390/app11219893. URL: https://www.mdpi.com/2076-3417/11/21/9893 (cit. on p. 90).

[53] Tse-Tong Chia. «Prediction of electromagnetic scattering from metasurfaces». In: *2016 10th European Conference on Antennas and Propagation (EuCAP)*. 2016, pp. 1–5. DOI: 10.1109/EuCAP.2016.7481429 (cit. on p. 121).

[54] Autodesk Inc. *DXF Reference*. 2011. URL: https://help.autodesk.com/view/OARX/2023/ENU/?guid=GUID-235B22E0-A567-4CF6-92D3-38A2306D73F3 (visited on 02/22/2023) (cit. on p. 175).

[55] P. Nayeri and University of Mississippi. School of Engineering. *Advanced Design Methodologies and Novel Applications of Reflectarray Antennas*. University of Mississippi, 2012 (cit. on p. 175).